Technical University of Denmark

DTU

# Slow light and pulse propagation in semiconductor waveguides

**Hansen, Per Lunnemann; Mørk, Jesper; Poel, Mike van der; Yvind, Kresten**

*Publication date:*
2010

*Document Version*
Publisher's PDF, also known as Version of record

Link back to DTU Orbit

**DTU Library**
Technical Information Center of Denmark

DTU

# Slow Light and Pulse Propagation in Semiconductor Waveguides

*Author:*
Per Lunnemann

*Supervisor:*
Prof. Jesper Mørk
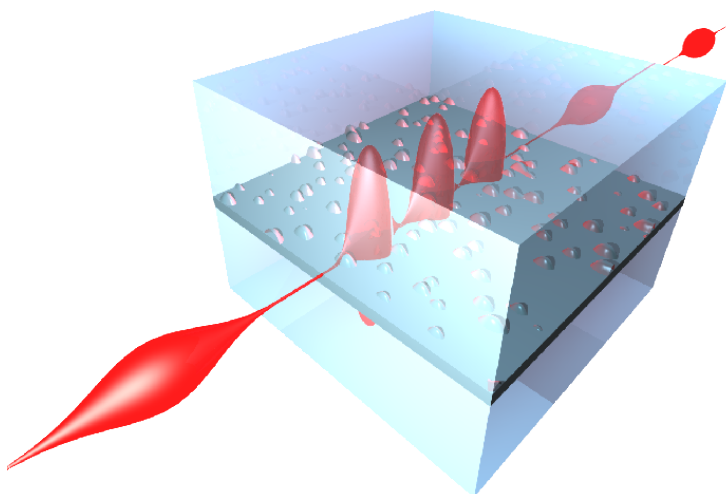
# Abstract

This thesis concerns the propagation of optical pulses in semiconductor waveguide structures with particular focus on methods for achieving slow light or signal delays.

Experimental pulse propagation measurements of pulses with a duration of 180 fs, transmitted through quantum well based waveguide structures, are presented. Simultaneous measurements of the pulse transmission and delay are measured as a function of input pulse energy for various applied electrical potentials. Electrically controlled pulse delay and advancement are demonstrated and compared with a theoretical model. The limits of the model as well as the underlying physical mechanisms are analysed and discussed.

A method to achieve slow light by electromagnetically induced transparency (EIT) in an inhomogeneously broadened quantum dot medium is proposed. The basic principles of EIT are assessed and the main dissimilarities between an atomic and a quantum dot medium are discussed. Three generic schemes are compared, showing that only one of the schemes are viable for slow light in an inhomogeneously broadened medium. The principal differences between the schemes are analysed and discussed. Propagation calculations of the three schemes are presented and compared together with estimates of the achievable delay and transmission.

Finally, measurements of the ultra fast gain dynamics of a quantum dot semiconductor optical amplifier are presented. The experiment is based on degenerate pump-probe transmission spectroscopy using 180 fs pulses. Both the wavelength dependence as well as the applied current density dependence are investigated. Two characteristic relaxation rates of $\sim 0.2$ ps and $\sim 1$ ps are extracted based on a theoretical model. The choice of model and the underlying physical processes of the measurements are discussed.

# Resumé

Denne afhandling omhandler udbredelsen af optiske pulser i halvleder bølge-lederstrukturer med særlig fokus på metoder hvorpå langsomt lys eller signal forsinkelser kan opnås.

Eksperimentelle pulsudbredelses-målinger af lyspulser af $\sim 180$ fs varighed, sendt igennem kvantebrøndsbaserede bølgeledere, præsenteres. Målinger af pulstransmission samt pulsforsinkelse er målt som funktion af input puls energi for forskelligt pålagte elektriske spændinger. Elektrisk kontrollerede pulsforsinkelser samt fremskyndelser demonstreres og sammenlignes med en teoretisk model. Grænserne for denne model, samt de underliggende fysiske processer analyseres og diskuteres.

Ydermere foreslås en metode til at opnå langsomt lys vha. elektromagnetisk induceret transparens (EIT) i et inhomogent forbredt kvantepunktsmedium. De grundlæggende principper for EIT gennemgås, og de vigtigste forskelle mellem et atomart og et kvantepunkts medium drøftes. Tre generiske systemer sammenlignes, hvor det vises, at i et inhomogent forbredt medium er det kun det ene af systemerne hvor langsomt lys kan realiseres. De primære forskelle mellem de tre systemer analyseres og diskuteres. Lysudbredelses beregninger af de tre systemer præsenteres og sammenlignes sammen med en vurdering af den opnåelige forsinkelse samt transmission.

Endeligt præsenteres målinger af den ultrahurtige dynamik af forstærkningen i en kvantepunktsforstærker. Eksperimentet tager sit udgangspunkt i degenereret pumpe-probe transmissions spektroskopi benyttende lyspulser med en varighed på 180 fs. Både afhængigheden af bølgelængde samt strømtæthed undersøges. To karakteristiske relaksations-tider, $\sim 0.2$ ps og $\sim 1$ ps, ekstraheres baseret på en teoretisk model. Valget af model og de underliggende fysiske processer for målingerne diskuteres.

# Preface

The research of this work was carried out at DTU Fotonik department of photonics technology in the Nano photonics cluster headed by Jesper Mørk, from June 2006 to August 2009 while I was enrolled as a Ph.D. student.

The work was supervised by Prof. Jesper Mørk, Associate Prof. Mike van der Poel and Associate Prof. Kresten Yvind and financed by the Danish Research Councils in the framework of QUEST.

During my work I have benefited from the knowledge and guidance of several people. Firstly, I would like to thank Jesper Mørk for his supervision during my Ph.D. While working with the, often troublesome, laser setup he always took active part in advising as well as supporting me. During my theoretical work Jesper always took the time to discuss my results and answer my sometimes "stupid" questions regarding carrier dynamics.

I would also like to thank Mike van der Poel for introducing me to the setup, for his experimental guidance and especially for his kind support during hard times in the laboratory. On the technical side I am grateful for Kresten Yvind's guidance and general expertise within semiconductor devices.

Also Sarah Ek is acknowledged for helping me with the pump-probe measurements and being pleasant company in the lab during these frustrating measurements.

A special thanks goes to Toke L. Hansen, Mads L. Andersen and Søren Stobbe for keeping a cheerful environment in the office and truly making the bicycle trip to the campus worth the ride.

Finally, I would like to express my gratitude to my family and friends for their ongoing support, and especially to Laila and Margot Rose for keeping me sane during my time of writing.

# Publications

The following publications have been authored or co-authored during the course of the Ph.D. project.

## Journal publications

- P. Lunnemann and J. Mørk (2009), *Reducing the impact of inhomogeneous broadening on quantum dot based electromagnetically induced transparency*, Applied Physics Letters **94** (7), 071108 (2009).

- J. Mørk, F. Öhman, M. van der Poel, Y. Chen, P. Lunnemann and K. Yvind (2008), *Slow and fast light: Controlling the speed of light using semiconductor waveguides*, Laser and Photonics Review **3**, 30-44 (2008).

## Journal publications in preparation

- P. Lunnemann, M. v. d. Poel, K. Yvind and J. Mørk. *Pulse Delay Measurements in Cascaded Quantum Well Gain and Absorber Media.*, submitted to Photonics Technology Letters, Aug. 2009.

## Book chapters

- P. L. Hansen, M. L. Andersen, M. v. d. Poel and J. Mørk (2008), *Nanofotonik: Nanofotonik kaster lys over fremtiden* in *Nanoteknologiske Horisonter*, DTU, pp. 145-160.

- K. Yvind, D. Larsson and P. L. Hansen (2007), *Nanoteknologi i masse-produktionOptiske Horisonter : en rejse på kommunikationsteknologiens vinger*, DTU, pp. 51-62.

## Proceedings

- P. Lunnemann and J. Mørk. *A method to achieve large tunable delays based on EIT in an inhomogeneously broadened quantum dot medium*, Slow and Fast Light, Honolulu, HI, USA, 2009.

- J. Mørk, T. R. Nielsen, W. Xue, Y. Chen and P. Lunnemann (2009), *Slow light in semiconductor structures: Physics and applications*, International Nano-Optoelectronics Workshop (iNOW), Berlin, 2009.

- M. van der Poel, P. L. Hansen and J. M. Mørk (2009), *Control of ultrafast pulse propagation in semiconductor components*, SPIE, San Jose, CA, USA, 2009.

- P. L. Hansen, M. v. d. Poel, K. Yvind and J. Mørk (2008), *Experimental observation of pulse delay and speed-up in cascaded quantum well gain and absorber media*, Slow and Fast Light, Boston, MA, USA, 2008.

- P. L. Hansen, M. v. d. Poel, K. Yvind and J. Mørk (2008), *Pulse Delay and Speed-up of Ultra Fast Pulses in an Absorbing Quantum Well Medium*, CLEO/QELS, San Jose, CA, USA,2008.

- P. L. Hansen, M. v. d. Poel, K. Yvind and J. Mørk (2008), *Pulse delay and advancement of ultrafast pulses in semiconductor waveguides*, Annual meeting Danish Physical Society, Nyborg, Denmark, 2008.

- J. Mørk, Öhman, F., M. v. d. Poel, P. L. Hansen, Nielsen, T. R., Kær Nielsen, P., Thyrrestrup Nielsen, H. and K. Yvind, *Slow light in semiconductor waveguides: Theory and experiment*, CLEO/Europe-IQEC 2007, Munich, Germany, 2007.

- P. L. Hansen, M. v. d. Poel, K. Yvind and J. Mørk (), *Slow light in semiconductor quantum dots*, Annual meeting Danish Physical Society, Nyborg, Denmark, 2007.

# Contents

# CHAPTER 1

# Introduction

Techniques for tailoring the velocity of light have over the past 10 years received an ever increasing interest by physicists and engineers. The reason for this is two-fold: The study of slow and fast light is intrinsically coupled to the study of light-matter interaction, and as such is of fundamental interest. The use of slow light may also serve as a tool to study nonlinear effects that otherwise require extremely high laser power. Secondly, slow light may lead to several promising applications for use in quantum computing, all-optical signal processing and micro wave photonics. In this chapter different quantities describing the velocity of light is introduced and is followed by a discussion of several techniques that are currently exploited for slow and fast light. Finally, the main emphasis of this thesis is outlined.

## 1.1 A historical background

The first evidence that the velocity of light was finite was shown by the Danish astronomer O. C. Rømer (1644-1710) in 1676. By measuring the orbital period of the innermost moon of Jupiter, he found that the period depended on whether we (on the planet Earth) were moving away or towards Jupiter, during our revolution about the sun. By adding up all the measured differences from the position being the closest to Jupiter in the orbit of Earth to the diametrically opposite point, he concluded that it takes the light 22 min to travel the distance corresponding to the diameter of the Earths orbit around the Sun[1] [1, 2]. The first terrestrial measurement of the velocity of light was carried out nearly two centuries after by A. H. L. Fizeau (1819-1896) using a rotating toothed wheel and a retro-reflecting mirror set up 9 km away from the wheel in the suburbs of Paris[1, 2]. By ejecting a pulse of light through a hole in the disc, he could determine the travel time of the reflected pulse by adjusting the rotation velocity such that the reflection was transmitted though the

---

[1]The correct number is found to be 16 min 40 s.

hole of the disc. This lead to a predicted velocity of $315\,300$ km/s [2]. Shortly after, using a similar technique with rotating mirrors, L. Foucault (1819-1868) reported that the velocity of light was slower in water compared to air. Later, in a series of experiments A. Michelson (1852-1931) reported a light velocity being $2.998 \cdot 10^8$ m/s. Some years later A. Einstein (1879-1955) developed the special relativity theory that states that the velocity of light is a constant independent of the state of motion of the emitting object. Finally, in 1983, the meter was defined by the International System of Units (SI), as the the distance light travels in $1/299\,792\,458$ s [1].

## 1.2 The velocity of light

Most of the above mentioned measurements, were all measurements in vacuum or close to vacuum (e.g. air). For light propagating in a medium, however, several definitions characterising the velocity of light becomes convenient. In the following we shall discuss the *phase velocity* and *group velocity*. As with all work treating the subject of electromagnetic waves, this starts with Maxwell's equations.

It was not until J. C. Maxwell (1831-1879) derived his set of equations that it was realised that electricity, magnetism and light are manifestations of the same phenomenon -electromagnetism. According to Maxwell, the evolution of electromagnetic waves in matter are governed by the Maxwell equations [3]:

$$\nabla \cdot \mathbf{D} = \rho_{free} \tag{1.1}$$
$$\nabla \cdot \mathbf{B} = 0 \tag{1.2}$$
$$\nabla \times \mathbf{E} = -\partial_t \mathbf{B} \tag{1.3}$$
$$\nabla \times \mathbf{H} = \mathbf{J} + \partial_t \mathbf{D}, \tag{1.4}$$

Where $\mathbf{D}$, $\mathbf{B}$, $\mathbf{E}$ and $\mathbf{H}$ are the electric displacement, magnetic, electric and auxiliary field respectively and $\mathbf{J}$ and $\rho_{free}$ are the free current and charge densities, respectively. Here, the partial derivative with respect to time is represented by $\partial_t$. Applying the curl of (1.3) and using $\mathbf{B} = \mu_{\mathrm{o}}(\mathbf{H} + \mathbf{M})$ we have:

$$\nabla \times \nabla \times \mathbf{E} = -\partial_t \left(\nabla \times \mu_{\mathrm{o}}(\mathbf{H} + \mathbf{M})\right) \tag{1.5}$$

where $\mu_{\mathrm{o}}$ is the vacuum permeability. Restricting ourself to non magnetic material, we can set $\mathbf{M} = 0$ and furthermore using (1.4), the right hand side of equation (1.5) is simplified to

$$-\left(\mu_{\mathrm{o}}\partial_t \mathbf{J} + \mu_{\mathrm{o}}\partial_t^2 \mathbf{D}\right). \tag{1.6}$$

Setting $\mathbf{J} = 0$ and using $\mathbf{D} = \varepsilon \mathbf{E} = \varepsilon_0 \mathbf{E} + \mathbf{P}$ we arrive at

$$-\varepsilon_0 \mu_0 \partial_t^2 \mathbf{E} - \mu_{\mathrm{o}}\partial_t^2 \mathbf{P}, \tag{1.7}$$

where $\varepsilon_0$ is the vacuum permittivity and $\mathbf{P}$ is the polarization of the medium. Regarding the left hand side of (1.5), we use the vector identity $\nabla \times \nabla \times = \nabla(\nabla \cdot) - \nabla^2$ [3]and get

$$\nabla(\nabla \cdot \mathbf{E}) - \nabla^2 \mathbf{E}. \tag{1.8}$$

Since $\nabla \cdot \mathbf{D} = \nabla \cdot (\varepsilon \mathbf{E}) = \varepsilon \nabla \cdot \mathbf{E} + \mathbf{E} \nabla \cdot \varepsilon$, using (1.1), we may set $\nabla \cdot \mathbf{E} = 0$ for a homogeneous material with no free charge, and we finally arrive at the equality

$$-\nabla^2 \mathbf{E} + \varepsilon_0 \mu_0 \partial_t^2 \mathbf{E} = -\mu_o \partial_t^2 \mathbf{P} \tag{1.9}$$

which is also know as the electromagnetic wave equation [4].

### 1.2.1 Phase velocity

Assuming the light to be travelling in a loss-less dielectric medium and restricting the equation to one dimension we get

$$-\partial_z^2 E + \varepsilon\mu\partial_t^2 E = 0 \tag{1.10}$$

It can easily be shown [4] that, considering harmonic waves as solutions, we get solutions fulfilling $E(r,t) = E(r + 1/\sqrt{\varepsilon\mu}\, t', t + t')$, i.e. waves where each of the cophasal surfaces advance with the speed

$$v_p = \frac{1}{\sqrt{\varepsilon\mu}} \equiv \frac{c}{n}, \tag{1.11}$$

where $n$ is the refractive index. We shall refer to this velocity as the *phase velocity*. For the light travelling i vacuum ($\varepsilon\mu = \varepsilon_0\mu_0$) we see the well known relation

$$c = \frac{1}{\sqrt{\varepsilon_0\mu_0}}, \tag{1.12}$$

### 1.2.2 Kramers-Kronig relation

Consider a medium that is *time invariant* and *linear* to an input signal $s_{in}(t)$. By linear we mean that a time dependent change in $s_{in}(t)$ results in a proportional time dependent change in output $s_{out}(t)$, while by time invariance means that a shift in time of $s_{int}(t)$ results in an equal shift in time of $S_{out}(t)$. In this case we may write [1, 5]

$$s_{out}(t) = \int_{-\infty}^{\infty} h(t - t')s_{in}(t')\, \mathrm{d}t, \tag{1.13}$$

Fourier transforming the above equation, results in

$$S_{out}(\omega) = H(\omega)S_{in}(\omega) \tag{1.14}$$

where

$$S_{in}(\omega) = \int\limits_{-\infty}^{\infty} s_{in}(t)\, e^{i\,\omega t}\, dt \tag{1.15}$$

and similarly for the $s_{out}$ and $h$. Suppose that our input signal is turned on at $t = 0$, i.e. $s_{in}(t < 0) = 0$ which means, that all Fourier components of $S_{in}$ interfere destructively for $t < 0$. In this case, the requirement of causality implies that $s_{out}(t < 0) = 0$, and similarly we get that all Fourier components of $S_{out}$ intere destructively for $t < 0$. Now, imagine, that the medium acts as a filter, that only absorbes/amplifies a single frequency. This implies that the sum of all Fourier components of $S_{out}$ no longer interfere destructively giving $s_{out}(t < 0) \neq 0$, in contradiction with the requirement of causality. Thus, *a perfect filter, absorbing only a single frequency without disturbing other frequencies, does not exist.* This, is the essence of the Kramers-Kronig relation, that is derived as follows: The requirement of causality requires $h(t < 0) = 0$, thus for the fourier transform we have

$$H(\omega) = \frac{1}{2\pi} \int\limits_{-\infty}^{\infty} e^{i\,\omega t}\, h(t)\, dt = \frac{1}{2\pi} \int\limits_{0}^{\infty} e^{i\,\omega t}\, h(t)\, dt. \tag{1.16}$$

It can be shown, that $H(\omega)$ must be holomorphic[2] in the complex upper half plane [4, 5]. This allows us to use Cauchy's formular [5]:

$$H(\omega) = \frac{1}{i\,\pi} P \oint\limits_{\mathcal{C}} \frac{H(\omega')}{\omega - \omega'}\, d\omega' \tag{1.17}$$

It is physically sensible to assume $\lim_{\omega \to \infty} H(\omega) = 0$, since no atomic particles are able to move with infinitely high frequencies. Furhermore it can be shown that, $H(\omega)$ converges faster towards 0 than $1/\omega$, i.e. $\lim_{\omega \to \infty} H(\omega)/|\omega| = 0$ [6]. Thus, the contribution from integration along the semicircle in the upper complex plane of equation (1.17) vanishes, leaving only

$$H(\omega) = \frac{1}{i\,\pi} P \int\limits_{-\infty}^{\infty} \frac{H(\omega')}{\omega - \omega'}\, d\omega', \tag{1.18}$$

or alternatively

$$\Im\left(H(\omega)\right) = -\frac{1}{\pi} P \int\limits_{-\infty}^{\infty} \frac{\Re\left(H(\omega')\right)}{\omega - \omega'}\, d\omega' \tag{1.19a}$$

$$\Re\left(H(\omega)\right) = \frac{1}{\pi} P \int\limits_{-\infty}^{\infty} \frac{\Im\left(H(\omega')\right)}{\omega - \omega'}\, d\omega', \tag{1.19b}$$

---

[2]Which means that it is complex differentiable. In some literature this is often referred to as $H$ being analytical, which for functions in the complex plane is equivalent.

where $\Im$ and $\Re$ denotes the imaginary and real part, respectively. The linear response in a isotropic dielectric medium is given by the macroscopic polarisation. Thus, by rewriting equation (1.13) we get [5]

$$P(t) = \int_{-\infty}^{\infty} \chi(t - t') E_{in}(t') \, \mathrm{d}t' \tag{1.20}$$

where the electric susceptibility serves as the response function. Equation (1.19) then reads

$$\Im\left(\chi(\omega)\right) = -\frac{1}{\pi}\mathrm{P}\int_{-\infty}^{\infty} \frac{\Re\left(\chi(\omega')\right)}{\omega - \omega'} \, \mathrm{d}\omega' \tag{1.21}$$

$$\Re\left(\chi(\omega)\right) = \frac{1}{\pi}\mathrm{P}\int_{-\infty}^{\infty} \frac{\Im\left(\chi(\omega')\right)}{\omega - \omega'} \, \mathrm{d}\omega', \tag{1.22}$$

which is known as the Kramers-Kronigs relation [1, 3, 5]. It is recalled that the imaginary and real part of $\chi$ describes absorption, $\alpha$, and the refractive index $n$ (cf. chapter 2) from the relations

$$n^2 = 1 + \chi' \tag{1.23a}$$

$$\alpha = 2\frac{\omega n}{c}\chi''. \tag{1.23b}$$

Thus, the Kramers-Kronig states that a variation of absorption in frequency, leads to a variation of the refractive index. Moreover, a rapid change of absorption, e.g. a narrow atomic resonance, leads to a rapid change of the refractive index. We shall use this fact, when considering the group velocity of light defined in the following section.

### 1.2.3 The group velocity

Consider two identical plane waves but with slightly shifted frequencies. The sum of the two fields is then:

$$E_1(t) + E_2(t) = A_1 \cos\left[(k - \delta k)z - (\omega - \delta\omega)t\right] + \ldots \tag{1.24}$$

$$+ A_2 \cos\left[(k + \delta k)z - (\omega + \delta\omega)t\right] \tag{1.25}$$

$$= 2\cos(kz - \omega t)\cos(\delta k\, z - \delta\omega\, t) \tag{1.26}$$

$$= 2\cos\left[\omega\left(\frac{k}{\omega}z - t\right)\right]\cos\left[\delta\omega\left(\frac{\delta k}{\delta\omega}z - t\right)\right] \tag{1.27}$$

I.e. a carrier wave moving at $v_p = \omega/k$ and a slowly varying modulation as a result of beating, moving at the speed $\delta\omega/\delta k$ as is seen illustrated in figure 1.1 . In the limit where $\delta k \to 0$ and $\delta\omega \to 0$ we get

$$v_g = \frac{\partial\omega}{\partial k}, \tag{1.28}$$
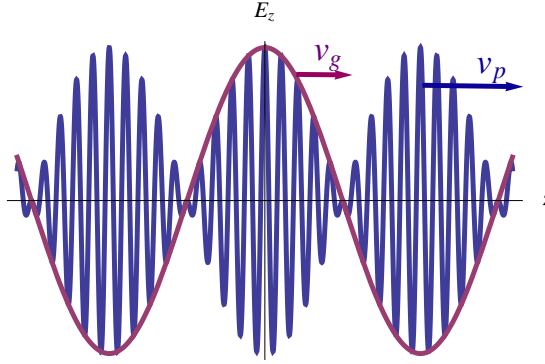
**Figure 1.1:** Illustration of the sum of two wavelets with near degenerate frequencies. The group velocity $v_g$ describes the velocity of propagation of the envelope of the the beat pattern and can be negative as well as postive. The phase velocity $v_p$ describes the velocity of a point moving with constant phase.

which is denoted the *group velocity*. A more rigorous derivation for a (single) pulse consisting of a continuum of frequencies is treated in section 2. For now, we note that the group velocity describes the velocity at which the peak of a pulse is moving in a medium. Noting that $k = \omega n/c$ where $n$ may depend on $\omega$, equation (1.28) may be rewritten to

$$v_g = \frac{c}{n + \omega \frac{\partial n}{\partial \omega}}. \tag{1.29}$$

From equation (1.29), it is clearly seen that by making $\partial_\omega n$ positive large it is possible to achieve a very small group velocity, while if $\partial_\omega n$ is large negative subliminal group velocities, i.e. $v_g > c$, and even negative group velocities are possible [7]. This has in literature been coined the terms slow and fast light, respectively, and figure of merit describing the degree of "slowness" is the *slowdown factor*:

$$S \equiv \frac{c}{v_g}. \tag{1.30}$$

As an example, consider a homogeneous gas consisting of $N$ atoms each with an optical transition between to states $|1\rangle$ and $|2\rangle$ with a dipole moment $\mu_{12}$. It is easy to show, that the complex electric susceptibility is given as [8, 9]

$$\chi(\omega) = \frac{N}{V} \frac{\mu_{12}^2}{\varepsilon_0 \hbar} \frac{\rho_{11} - \rho_{22}}{\omega - \omega_{12} + \mathrm{i}\,\gamma_{12}}, \tag{1.31}$$

where $\gamma$ is the homogeneous linewidth of the transition, and $\rho_{11}$ and $\rho_{22}$ are the occupation propabilities of $|1\rangle$ and $|2\rangle$, respectively. The imaginary ($\sim$absorption) and real ($\sim$refractive index) are plotted as a function $\omega$ in figure 1.2, for an absorbing ($\rho_{11} - \rho_{22} > 0$) and amplifying ($\rho_{11} - \rho_{22} < 0$) medium. Here it is seen, that the absorption peak of the transition leads to a rapid change of the refractive index as a result of the Kramers-Kronig theorem. From the
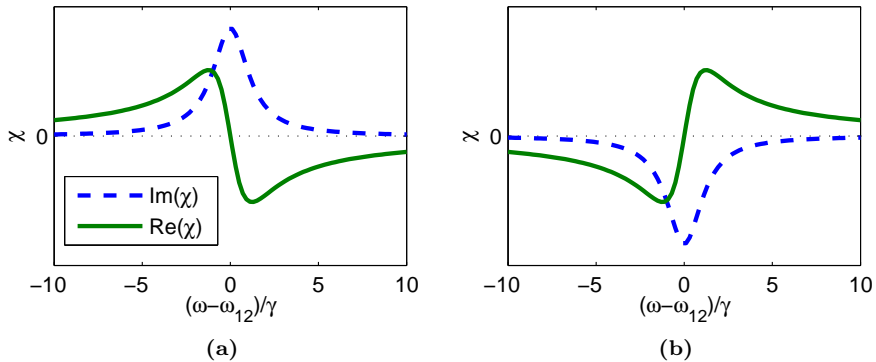
**Figure 1.2:** (a) Real (solid) and imaginary (dashed) part of $\chi$ as a function of frequency for an absorbing optical transition. As a result of Kramers-Kronig's theorem, a sharp peak in the absorption leads to a rapid change in the refractive index. A sufficiently negative slope of $\Re(\chi)$ at $\omega = \omega_{12}$ implies superluminal or even a negative group velocity. (b) Same as for figure (a) but for a medium with population inversion. The positive slope implies slow light, i.e. $v_g < c$.

negative slope at $\omega - \omega_{12} = 0$, it is seen from equation (1.29) that $v_g > c$. Similar we see that the amplifying case results in $v_g < c$ when $\omega \partial_\omega n$ is sufficiently negatively large.

A negative group velocity implies that the peak of a pulse appears at the output of the medium before entering it. This may seem like a contradiction of the special relativity theory, and has also lead to some misconception in literature (see discussions in [1]). We shall, however, not delve into the discussion, but rather note that the group velocity is not the same as the velocity of information contained in light, where the latter is always smaller than $c$. This matter was already treated by A. Sommerfeld and Brillouin during the first two decades of the 20th century and collected in an often cited English translation of the work [10].The book of P. W. Milonni [1] also gives a thorough discussion of this matter. Furthermore, negative and superluminal velocity of light has been experimentally demonstrated[11, 12, 13, 14, 15].

# 1.3 Techniques for tailoring the velocity of light

The scientific field of slow and fast light has evolved greatly over the past two decades. The fast advancement of technology has made the field evolve from being of basic scientific interest to a point where many promising application seems within reach. Today, slow and fast light has been observed in widely different optical systems, such as atomic gasses, semiconductor material, fibers and photonics bandgap material or a combination of these. In the following we shall briefly describe a few of the well known techniques. For a more rigourous introduction to the various techniques we refer to [16].

### 1.3.1 Photonic crystal structures

Photonic crystals (PCs) have recently found wide interest in the slow-light community [17, 18]. Photonic crystal waveguides (PCWs) has proven practical for slow light since the operating wavelength is easily designed, the structures are appropriate for miniaturisation and they offer wide-band applications suitable for future communication signals.

A PC membrane is a 2D periodic structure structure consisting of two materials with different refractive indices that in many cases may be considered as a grating [16]. For a certain band of wavelengths, known as the bandgap, the reflections from the boundaries between the two materials add up in phase, and as a result no waves can propagate within the bandgap [19]. Typically, the second material is air and the PC is made by periodically etching holes into a membrane of a dielectric. A PCW is introduced as a line defect, by leaving out a row of holes, where the light is confined in the transverse plane and allowed to propagate along the line defect. PCs and PCWs are conveniently described by their bandstructure diagram that shows the allowed modes of the light with frequency and wavenumber along the two axes. The line defect leads to a dispersion curve that crosses the bandgap. Close to the band edge where $k = \pi/a$, the slope of the dispersion curve converges towards 0. Thus, slow light is achieved for wavelengths close to the band edge. From equation (1.28), this implies a group velocity converging towards 0. However, there are several reasons why group velocities close to 0 are not possible. First of all, the dispersion curve near the band edge is parabolic, causing the group velocity to change rapidly with frequency. As a result, the pulse is subject to broadening and distortion [16]. Secondly, neither periodicity nor the shape of each individual hole is perfect. Since the band edge represents the cut-off where the mode turns from propagating to evanescent, imperfect crystals may in some parts lead to an evanescent mode, while in other parts lead to a propagating mode. This results in a very lossy propagation of the light. Several techniques, though, have addressed these issues. By carefull design of the holes near the waveguide, almost linear dispersion is possible over a broad range of wavelengths. This is achieved by changing the hole size [20], hole position [21] or by changing the width of the line defect [22].

Another issue of slow light using PCWs is related to the coupling losses. The modes with very low group velocity are often very different from modes of ridge waveguides. Thus, tapering of the waveguide width near the coupling wave guide is necessary [23]. Coupling losses can be further improved by design of a tapered PCW where the mode gradually enters the slow mode [24].

Achieving a low group velocity may be of use for enhancement of optical non-linearities. However, for use as a delay line, dynamic tunability of the group index is of utmost importance. Experiments using electric currents to heat of the PCW and thereby changing the refractive index, has been demonstrated for tuning the group velocity [23].

Finally, losses associated with slow light in PCW can be significant. Scattering from surface roughness and irregular periodicity lead to losses that scales with the group velocity. This can be understood from the fact that for a slow mode, the field penetrates deeper into the PC, and the mode is therefore subject to more scattering off the irregularities.

### 1.3.2 Coherent population oscillations

Coherent population oscillations (CPO) is a technique that has been demonstrated effective for control of the group velocity of light in semiconductor materials [25, 26, 27, 28, 29], doped fibers [15, 30], as well as Ruby and Alexandrite crystals [31, 32] at room temperature. Especially semiconductors have recently shown huge progress using semiconductor optical amplifiers (SOAs) and electro absorbers (EAs). Phase shifts of amplitude modulated signals at GHz were demonstrated in [26, 28]. Based on the same principles, electrical control of the phase shift was shortly after demonstrated [27].

CPO is based on a strong pump resonant with a two-level transition at frequency $\omega_0$ and a weak copropagating probe with a frequency $\omega_0 + \Omega$. Typically, this is achieved by amplitude modulation of the pump beam at a frequency $\Omega$ where one of the sidebands plays the role of a probe beam. The beating between pump and probe causes oscillations of the carrier population that lead to a temporal modulation of both gain and refractive index. Hence, both phase and amplitude of the pump beam is modulated. In frequency space, this results in a scattering into the two sidebands with frequency $\omega_0 + \Omega$ and $\omega_0 - \Omega$. Thus, for an absorbing medium, the probe experience a spectral hole in the absorption spectrum that, due to Kramers-Kronigs relation, leads to a reduction of the group velocity. Similarly, for an amplifying medium the probe experience a spectral hole in the gain spectrum that results in an increase of the group velocity. The intensity of the probe determines the depth of the spectral hole, and therefore the degree of slowdown. The width of the spectral hole sets the upper bandwidth limit, and is governed by the population lifetime since this sets the shortest time scale in which the population (incoherently) follows the beating. In SOAs the lifetime is typically the radiative liftime being in the order of 1 ns while for EAs, the lifetime is also governed by the carrier sweep out time caused by the applied electric potential, that leads to somewhat shorter carrier lifetimes . CPO in semiconductors is therefore a technique that is well

suited for optical communication based signals operating in the GHz regime [27, 33].

It is interesting to note, that the word *coherent* in this context refers to the coherence between two optical fields rather than between the quantum states of the carriers. Thus, CPO is not affected by dephasing of the quantum states that generally is a detrimental effect for techniques such as EIT (see chapter 5), and as such, CPO can be exploited at room temperature.

Although the probe experiences a spectral hole in the absorption spectrum, finite absorption is still present that for fairly short propagation lengths leads to significant signal attenuation. A way of avoiding this drawback is to cascade amplifying and absorbing sections [34]. Here, the amplifying section serves to amplify a possibly weak pulse transmitted through an absorbing section. Due to discrepancy between the saturation power of the absorbing and amplifying sections, a finite delay is possible even with a net positive gain. Pulse delay and advancement of ultrafast pulses, using similar type of structures, are demonstrated and discussed in chapter 4.

Lately, the phase shift of the modulated signal has been greatly enhanced by the use of chirping in combination with filters [35, 36]. Here the input signal is chirped, while the output signal is filtered by a notch-filter centered at the red shifted side bands. By tuning the degree of chirp, it is possible to achieve an RF phase shift of more than $2\pi$ [37].

### 1.3.3 Electromagnetically induced transparency

Electromagnetically induced transparency (EIT) [38, 39] is probably the technique that has attracted the most public attention since the impressive results of Hau et al. in 1999, demonstrating a group velocity of 17 m/s [40]. Since then, astounding physical phenomena based on EIT have been demonstrated, such as stored light [41, 42, 43], stationary light [44], single-photon slowdown and storage[45] and optical information processing with matter wave dynamics [46]. The principles of EIT are described in chapter 5.

Although EIT has shown great potential in atomic gasses, only few demonstrations have been reported in semiconductor material [47, 48, 49, 50], due to the requirement of isolated quantised states with fairly low dephasing. In chapter 5 we shall analyse the impact of dephasing and inhomogeneous broadening on EIT using self assembled quantum dots.

### 1.3.4 Gain saturation

A type of scheme that is analysed in chapter 4, is based on saturation of an amplifying or absorbing medium. In this type of scheme, a temporal shift of a short pulse is induced while propagating through a saturable absorber or amplifier, respectively [51]. Here, the front of the pulse experience a stronger absorption/amplification compared to the tail of the pulse, and as a result the pulse appears delayed/advanced. As such, the main mechanism causing the delay is not related to a steep slope in the frequency dependence of the refractive index, but is rather a pulse shaping mechanism. We shall therefore avoid using the terms slow light or slowdown in this case [52, 53]. The scheme has proven effective as a simple mean for delaying or advancing ultra fast pulses in short and compact semiconductor wave guides [54, 55]. Recently, the same effect was exploited in [56], where it was shown that by pre-chirping the pulse, the achievable pulse advancement could be drastically increased. However, because it requires pulse compressors/stretchers, this technique is not yet feasible for achieving monolithically integrated devices that allow for controllable pulse delays.

In general, the major drawback of this type of scheme is that the achievable delay cannot exceed the pulse width [57], while the largest delays are associated with a large pulse absorption. In chapter 4, it is shown that this issue can be avoided by cascading amplifying and absorbing sections, while still achieving a net delay.

## 1.4 Thesis outline

In this thesis both experimental as well as theoretical work on pulse propagation in semiconductor waveguides are reported with emphasis on methods for achieving signal delays.

Semiconductor wave guides are in many aspects advantageous for use in slow light applications. First of all, they offer a significant enhancement of the interaction length that, to first order, scales with the possible delay. Secondly, most slow light schemes are based on a nonlinear optical response such as CPO, gain saturation and EIT, that requires high intensities. With a tight confinement of the optical mode, the required optical power is drastically reduced while the mode overlap with the active material is strongly enhanced.

The use of semiconductor material is of particular interest since it offers compactness and enables for monolithic integration into opto-electronic devices using well established processing techniques. Furthermore, while the currently reported slowdown is less than what has been observed in other materials [16, 33, 58], semiconductors are attractive since the operating wavelength, to a large extend, can be designed while performing with bandwidths in the GHz regime that is well suited for communication signals.

In chapter 2, the basic equations for describing the interaction between a

semiconductor and a pulse on the order 100 fs are derived. The chapter will serve as a basic toolbox for the following chapters that use special cases of the derived equations. We start out by deriving the wave equation describing the propagation of a slowly varying envelope in an isotropic medium. The material gain dynamics are evaluated using the semi-classical density matrix approach and some numerical propagation examples are discussed. Finally, some simplifications are considered that are well suited for comparison with measurements in chapter 4.

In chapter 4, experimental pulse delay measurements of $\sim$ 200 fs pulses transmitted through saturated quantum well based waveguides are analysed and discussed. Simultaneous measurements of the transmission and pulse delay are compared with theory using a standard optical amplifier structure as well as for a cascaded absorbing and amplifying wave guide. Observed effects that can not be described by a simple propagation model are analysed and discussed.

Slow light using EIT in a quantum dot (QD) medium has recently been proposed [59, 60], but has so far mainly been observed on a single or few QDs due to the large inhomogeneous broadening (IHB). In chapter 5, a theoretical proposal of how to achieve slow light using EIT in an inhomogeneously broadened QD medium is presented. The main principles of EIT are discussed and differences between quantum dots and atoms are investigated. Three generic schemes are compared and the differences are analysed. Finally, propagation calculations are presented with estimations of the achievable delay.

In chapter 4 the ultra fast saturation behaviour of the gain dynamics are exploited to achieve a pulse delay and advancement. In chapter 6, the ultra fast gain dynamics of a quantum dot SOA is measured using a standard degenerate transmission pump-probe technique. Both the dependence on wavelength as well as applied current is investigated, and two characteristic relaxation times are extracted. Furthermore, the characterised QD SOA's strong resemblance to a quantum well (QW) and bulk medium is discussed.

A summary of the conclusions together with an outlook is given in chapter 7.

# CHAPTER 2

# Light Matter Interaction

In this section, some of the basic equations that describe the interaction between light and matter are derived. Restricting the attention to a homogeneous isotropic material imbedded in a loss-less background material, we derive the wave equation governing the field propagation in an amplifying or absorbing medium using the slowly varying amplitude approximation. This is proceeded by deriving the rate equation of the carrier dynamics in a semiconductor material, which allows for fully solving the propagation of ultra short pulses.

## 2.1 The slowly varying envelope approximation

In chapter 1, the wave equation (1.9) was derived in a form that is generally valid for most purposes in a dielectric. The only assumption that was made was assuming an isotropic and homogeneous material. The latter is primarily violated in material with a refractive index changing over length scales comparable to the optical wavelength, e.g in a photonic crystal [19]. However, (1.9) is cumbersome to solve for realistic problems and we shall therefore proceed by simplifying (1.9) further to a form commonly used for semiconductor optical devices.

Considering the **x** component of the electric field traveling along the **z** axis, equation (1.9) is written as:

$$\partial_z^2 E(z,t) - \frac{1}{c^2}\partial_t^2 E(z,t) = \mu_0 \partial_t^2 P(z,t). \qquad (2.1)$$

It is convenient to separate the induced polarisation into two parts: One arising from the background material $P_{bg}$ and one arising from the active material, i.e. the gain material $P_a$. Fourier transforming (2.1) with respect to time results

in:

$$\partial_z^2 E(z,\omega) + \frac{\omega^2}{c^2} E(z,\omega) \quad = \quad -\mu_0 \omega^2 \left( P_a(z,\omega) + P_{bg}(z,\omega) \right) \qquad (2.2)$$

$$= \quad -\mu_0 \omega^2 \left( P_a(z,\omega) + \varepsilon_0 \chi_{bg}(z,\omega) E(z,\omega) \right), (2.3)$$

where for the last equality, the polarisation of the background material was assumed to respond linearly with the electric field. Collecting terms with $E$ on one side and using $(1 + \chi_{bg})\omega^2/c^2 = n_{bg}^2(\omega)\omega^2/c^2 = k(\omega)^2$ we get

$$\partial_z^2 E(z,\omega) + k(\omega)^2 E(z,\omega) = -\mu_0 \omega^2 P_a(z,\omega) \qquad (2.4)$$

It is convenient to decompose the electric field and polarisation into its slowly varying envelopes:

$$E(z,t) \quad = \quad \mathcal{E}(z,t)\, \mathrm{e}^{\mathrm{i}(k_0 z - \omega_0 t)} + c.c. \qquad (2.5)$$

$$P(z,t) \quad = \quad \mathcal{P}(z,t)\, \mathrm{e}^{\mathrm{i}(k_0 z - \omega_0 t)} + c.c.\,, \qquad (2.6)$$

where $\omega_0$ is the carrier frequency and $k_0$ is the corresponding wave vector in the absence of an active material. Inserting (2.5) and (2.6) into equation (2.3) and ignoring terms with $\partial_z^2 \mathcal{E}$ and $\partial_z^2 \mathcal{P}$ [1] we get

$$\left( k(\omega)^2 - k_0^2 \right) \mathcal{E}(z,\Omega) + 2\,\mathrm{i}\, k_0 \partial_z \mathcal{E}(z,\Omega) = -\mu_\mathrm{o} \omega^2 \mathcal{P}_a(z,\Omega)\,, \qquad (2.7)$$

where $\Omega = \omega - \omega_0$. The term $k(\omega)$ depends on the frequency and the relation between $\omega$ and $k$ depends on the chosen material. Proceeding by Taylor expanding $k$ around the central laser frequency $\omega_0$ we get $k(\omega) = k_0 + \partial_\omega k(\omega)|_{\omega_0}\Omega + 2^{-1}\partial_\omega^2 k(\omega)|_{\omega_0}\Omega^2 + \ldots$. The necessary number of terms to include of course depends on the bandwidth of the laser pulse. Remembering from chapter 1 that $\partial_\omega k(\omega)|_{\omega_0}$ is the reciprocal of the group velocity, hence $\partial_\omega^2 k(\omega)|_{\omega_0}$ describes the group velocity dispersion (GVD). Therefore, neglecting GVD and higher order terms, it is sufficient using a first order expansion, i.e. $k(\omega) \approx k_0 + v_g^{-1}\Omega$. Dividing by $2\,\mathrm{i}\, k_0$ and using the approximations $k(\omega)^2 - k_0^2 = (k(\omega) - k_0)(k(\omega) + k_0) \approx 2k_0(k(\omega) - k_0)$ and $\frac{\omega^2}{c^2 k_0} = \frac{1}{cn_0}\frac{\omega^2}{\omega_0} \approx \frac{\omega}{cn_0}$ results in:

$$-\frac{\mathrm{i}}{v_g}\Omega \mathcal{E}(z,\Omega) + \partial_z \mathcal{E}(z,\Omega) = \mathrm{i}\,\frac{\omega}{2\varepsilon_0 cn_0}\mathcal{P}_a(z,\Omega) \qquad (2.8)$$

Applying the inverse Fourier transform for the low frequencies $\Omega$ gives us

$$\frac{1}{v_g}\partial_t \mathcal{E}(z,t) + \partial_z \mathcal{E}(z,t) = -\frac{1}{2\varepsilon_0 cn_0}\partial_t \mathcal{P}_a(z,t) + \mathrm{i}\,\frac{\omega_0}{2\varepsilon_0 cn_0}\mathcal{P}_a(z,t)\,. \qquad (2.9)$$

For lightwaves whose amplitude, $\mathcal{E}(z,t)$, changes little in an optical cycle we have $|\partial_t \mathcal{P}| \ll \omega_0 |\mathcal{P}|$. Thus, neglecting the first term on the right hand side of (2.9) we arrive at a simplified waveequation:

$$\frac{1}{v_g}\partial_t \mathcal{E}(z,t) + \partial_z \mathcal{E}(z,t) = \mathrm{i}\,\frac{\omega_0}{2\varepsilon_0 cn_0}\mathcal{P}_a(z,t)\,. \qquad (2.10)$$

---

[1]This is justified by realizing that $|\partial_z^2 \mathcal{E}(z,t)| \ll |\,\mathrm{i}\, k\partial_z \mathcal{E}|$.

The slowly varying polarisation may be written as:

$$\mathcal{P}_a(z,t) = \varepsilon_0 \chi(z,t)\mathcal{E}(z,t), \tag{2.11}$$

where a time dependence of $\chi$ is explicitly written, that could arise from non-linearities. For a continuous wave, (2.10) takes the simple form

$$\partial_z \mathcal{E}(z,t) = \mathrm{i}\,\frac{\omega_0}{2cn_0}\chi(z,t)\mathcal{E}(z,t) \equiv \mathrm{i}\,\frac{\omega_0}{2cn_0}\left(\chi'(z,t) + \mathrm{i}\,\chi''(z,t)\right)\mathcal{E}(z,t), \tag{2.12}$$

where $\chi'$ and $\chi''$ denote the real and imaginary part of the susceptibility, respectively. From this, it is clearly seen that the imaginary part of $\chi$ is related to absorption/gain whereas the real part influence the wave vector, i.e. the refractive index.

Equation (2.10) is easily rewritten to describe the photon flux using the relation [61]

$$\mathcal{S}(z,t) = \frac{\varepsilon_0 n_0 n_g}{2\hbar\omega_0}|\mathcal{E}|^2 \equiv C|\mathcal{E}|^2. \tag{2.13}$$

Separating the amplitude and phase of the electric field, $\mathcal{E} = |\mathcal{E}|\,\mathrm{e}^{\mathrm{i}\,\phi}$ we get:

$$\frac{1}{v_g}\left(\partial_t|\mathcal{E}| + \mathrm{i}\,|\mathcal{E}|\,\partial_t\phi\right) + \partial_z|\mathcal{E}| + \mathrm{i}\,|\mathcal{E}|\,\partial_z\phi = \mathrm{i}\,\frac{\omega_0}{2cn_0}\left(\chi'(z) + \mathrm{i}\,\chi''(z)\right)|\mathcal{E}(z)| \tag{2.14}$$

Multiplying with $2C|\mathcal{E}|$ on both sides of (2.14) and noting that $\partial_t\mathcal{S} = 2C|\mathcal{E}|\,\partial_t|\mathcal{E}|$ and $\partial_z\mathcal{S} = 2C|\mathcal{E}|\,\partial_z|\mathcal{E}|$ gives:

$$\frac{1}{v_g}\left(\partial_t\mathcal{S} + \mathrm{i}\,2\mathcal{S}\,\partial_t\phi\right) + \partial_z\mathcal{S} + \mathrm{i}\,2\mathcal{S}\,\partial_z\phi = \mathrm{i}\,\frac{\omega_0}{cn_0}\left(\chi'(z) + \mathrm{i}\,\chi''(z)\right)\mathcal{S}. \tag{2.15}$$

Separating imaginary and real components results in two equation governing the phase and field intensity:

$$\frac{1}{v_g}\partial_t\mathcal{S}(z,t) + \partial_z\mathcal{S}(z,t) = -\Gamma\frac{\omega_0}{cn_0}\chi''(z,t)\mathcal{S}(z,t) \tag{2.16}$$

$$\frac{1}{v_g}\partial_t\phi(z,t) + \partial_z\phi(z,t) = \Gamma\frac{\omega_0}{2cn_0}\chi'(z,t)\phi(z,t), \tag{2.17}$$

where the field overlap with the active medium is explicitly included by the confinement factor, $\Gamma$ [62].

From equations (2.16) and (2.17) it is seen that since $\chi'$ and $\chi''$ are coupled through the Kramers-Kroniger relation, the intensity and phase are also coupled. In section 2.3, the induced polarisation is derived in order to solve the propagation of a pulsed optical field. For these calculations we neglect the dynamics of the phase, governed by (2.17). In the limit of intense pulses and long propagation times, the phase evolution is well known to influence the propagation of the envelope [63, 64, 65, 66, 67]. This is realised since, as we shall see in section 2.3, a strong pulse leads to drastic changes of $\chi''$, (i.e. gain/absorption) within the duration of the pulse. Through Kramers-Kronig relation [3, 5], this leads to changes of $\chi'$ (i.e. the refractive index), giving a shift of the instantaneous frequency, $\partial_t\phi$, as seen from (2.17). For a medium where the

gain/absorption shows a strong dependence of the frequency (gain/absorption dispersion), the shift of frequency goes back as a change of the gain/absorption. Other simplifying assumptions used in deriving (2.16) and (2.16) may not be appropriate for short and intense pulses. E.g., for sufficiently short pulses, the spectral width of the pulse requires more terms in the Taylor expansion of the background material wave vector $k$ when deriving (2.8). Including GVD (2. order expansion), leads to a modification of the left handside of (2.10) with an additional term $i\tilde{\beta}\partial_t\mathcal{E}/2$, where $\tilde{\beta} = \partial_\omega^2 k(\omega)|_{\omega_0}\Omega^2$[66]. This causes an increasing pulse chirp and broadening , as the pulse propagates through the medium [68], that goes back as a change of the gain/absorption through gain/absorption dispersion and/or through gain non-linearities. Finally, including non-linearities in the background material, leads to a refractive index, $n_0$, that depends on the instantaneous intensity. With gain/absorption dispersion this leads to a time dependent change of gain/absorption. We shall discuss this issue in more detail in chapter 4.

## 2.2 Evaluating the polarisation

In order to solve (2.10), it is necessary to evaluate the polarisation that acts as a source term in the equation. To do this, the density matrix formalism is used [9]. The density matrix formalism allows for evaluation of the expectation value of quantum mechanical operators even though the precise wavefunction is unknown. Specifically we are interested in evaluating the average dipolemoment $\langle\mathbf{d}\rangle$ of an electron-hole pair. We shall start out by considering a two level system as is often encountered in atomic physics.

The density operator is a hermitian operator defined as

$$\hat{\rho} = |\psi\rangle\langle\psi|, \tag{2.18}$$

where $|\psi\rangle$ is a general state in the Hilbert space spanned by the orthonormal states $\{\phi_1, \phi_2, \ldots\}$. It is easily shown, that the expectation value of any observable $\hat{A}$ is given by [69]

$$\langle\hat{A}\rangle = \text{tr}(\hat{\rho}\hat{A}) \tag{2.19}$$

Expanding $|\psi\rangle$ on the basis states we get:

$$\hat{\rho} = \sum_{i,j} c_i c_j^* |\phi_i\rangle\langle\phi_j|. \tag{2.20}$$

From this it is seen that the diagonal elements, $\rho_{ii} \equiv \langle\phi_i|\hat{\rho}|\phi_i\rangle = |c_i|^2$, describe the population density of the corresponding state $|\phi_i\rangle$. Considering the mean dipole moment $\langle\mu\rangle = \text{tr}(\hat{\rho}\hat{\mu})$ which in our specific example evaluates to

$$\langle\mu\rangle = \sum_{i,j} (\rho_{ij}\mu_{ji} + \rho_{ji}\mu_{ij}) \quad (i \neq j), \tag{2.21}$$

since $\langle i|\hat{\mu}|i\rangle = 0$ due to the odd parity of $\hat{\mu} = e\hat{z}$ and assuming symmetric or antisymmetric wavefunctions. Thus, the off-diagonal elements of $\rho$ describe the mean dipole moment. The time evolution of the density matrix is governed by Liouville's theorem,

$$\partial_t \hat{\rho} = -\frac{i}{\hbar}[\hat{H}, \hat{\rho}]. \tag{2.22}$$

From equation (2.22) the evolution of the dipole momentum as well as the population density is calculated.

Before proceeding further, we shall elaborate on the Hamiltonian by considering a simple two level system, with the states $|1\rangle$ and $|2\rangle$ and associated eigen energies $\hbar\omega_1$ and $\hbar\omega_2$. The states are often termed "bare states" since they describe eigen states of the system without the presence of an external pertubation, i.e. an electrical (optical) field. For an applied optical field, the Hamiltonian of the system is changed through the interaction between light and matter. For all work in this thesis, we consider sufficiently intense optical fields to treat the electric field classically, while being sufficiently weak to treat the interaction Hamiltonian as a small perturbation. Using the dipole approximation [9], the interaction Hamiltonian takes the form:

$$\hat{H}_1 \approx -\hat{\mu} \cdot \mathbf{E}, \tag{2.23}$$

where $\hat{\mu}$ is the dipole moment operator. Writing the electric field in terms of its slowly varying envelope $E(z,t) = \mathcal{E}(z,t)\, e^{-i\omega_0 t} + c.c.$, we find for the considered two level system:

$$\hat{H}_1 = -\hbar \left( e^{-i\omega t} \Omega(z,t) + c.c \right) \left( |1\rangle\langle 2| + |2\rangle\langle 1| \right), \tag{2.24}$$

where we have introduced the Rabi frequency $\Omega(z,t) \equiv (\mu_{12}\mathcal{E}(z,t))/\hbar$ and assumed $\boldsymbol{\mu}_{12} = \mu_{12}\hat{\mathbf{z}}$. As the interaction Hamiltonian is considered to be a small perturbation, it is convenient to express the operators in the interaction picture. The Hamiltonian then takes the form:

$$\hat{H}_1^{int} = e^{i\hat{H}_0 t/\hbar} \hat{H}_1 \, e^{-i\hat{H}_0 t/\hbar} \tag{2.25}$$

$$= -\hbar \left( e^{-i\omega t} \Omega(z,t) + c.c \right) \left( e^{-i\omega_{21} t} |1\rangle\langle 2| + e^{i\omega_{21} t} |2\rangle\langle 1| \right), \tag{2.26}$$

$$\approx -\hbar \left( e^{-i\Delta t} \Omega(z,t)|2\rangle\langle 1| + e^{i\Delta t} \Omega^*(z,t)|1\rangle\langle 2| \right), \tag{2.27}$$

where $H_0 = \hbar\omega_1|1\rangle\langle 1| + \hbar\omega_2|2\rangle\langle 2|$, $\Delta \equiv \omega_0 - \omega_{21}$ and $\omega_{ij} = \omega_i - \omega_j$. In equation (2.27) we used the rotating wave approximation [9] neglecting all fast oscillating terms. Inserting (2.27) into (2.22) we find the time evolution of the density matrix in the interaction picture as

$$\partial_t \tilde{\rho}_{21} = -i\,\Omega(z,t)\,(\rho_{22} - \rho_{11}) - (\gamma - i\,\Delta)\rho_{21} \tag{2.28a}$$

$$\partial_t \tilde{\rho}_{12} = \partial_t \tilde{\rho}_{21}^* \tag{2.28b}$$

$$\partial_t \rho_{22} = -i\,\Omega^*(z,t)\tilde{\rho}_{21} + i\,\Omega(z,t)\tilde{\rho}_{12} - \Gamma\rho_{22} \tag{2.28c}$$

$$\partial_t \rho_{11} = -\partial_t \rho_{22} \tag{2.28d}$$

where we have introduced $\tilde{\rho}_{12} \equiv e^{-i\Delta t}\rho_{12}$ and $\tilde{\rho}_{21} = \tilde{\rho}_{12}^*$. Furthermore, decay was added phenomenologically with $\gamma$ denoting the polarisation decay rate

while $\Gamma$ denotes the population decay rate from $|2\rangle$ to $|1\rangle$. Note that from equation (2.28d) we imply conservation of the population density neglecting any population losses out of the subspace spanned by $|1\rangle$ and $|2\rangle$. Solving equations (2.28a)-(2.28d) allows for evaluating the polarization as the total dipole moment divided by the volume using equation (2.21):

$$
\begin{aligned}
P(t) = V^{-1} \sum_i \langle \mu_i \rangle &= \varrho \langle \mu \rangle \\
&= \varrho \mu_{12} (\mathrm{e}^{\,\mathrm{i}\,\omega_{21} t}\, \tilde{\rho}_{12}\, \mathrm{e}^{\,\mathrm{i}\,\Delta t} + c.c.) \\
&= \varrho \mu_{12} (\tilde{\rho}_{12}\, \mathrm{e}^{\,\mathrm{i}\,\omega_0 t} + c.c)
\end{aligned}
\tag{2.29}
$$

where $\varrho$ is the density of 2-level systems and the term $\mathrm{e}^{\,\mathrm{i}\,\omega_{21} t}$ arises from transforming from the interaction picture to the Schrödinger picture.

## 2.3 Pulse propagation in a semiconductor material

Equation (2.28a)-(2.28d) are easily modified to apply for semiconductor material, describing the electron and hole dynamics. In this case, the field is considered to be interacting with a collection of inhomogeneously broadened two level systems labelled by their corresponding wave vector $k$ [62]. For semiconductor structures offering a continuum of states (i.e. bulk and QWs), the carrier density distribution is treated to approach an equilibrium distribution given by the Fermi distribution [61]. With this assumption, we avoid having to deal with the semiconductor optical bloch equations [70] where many body problems such as Coulomb interactions between carriers are included [71]. In the following we shall derive the density matrix describing SOA following the work in [64]. We get:

$$
\partial_t \tilde{\rho}_{cv,k} = -\,\mathrm{i}\,\Omega(z,t)\,(\rho_{c,k} + \rho_{v,k} - 1) - (\gamma_2 - \mathrm{i}\,\Delta_k)\tilde{\rho}_{cv,k}
\tag{2.30}
$$

$$
\begin{aligned}
\partial_t \rho_{\alpha,k} = &-\gamma_\alpha^{(sc)}(\rho_{\alpha,k} - f_{\alpha,k}) - \gamma_\alpha^{(h)}(\rho_{\alpha,k} - f_{\alpha,k}^L) - \gamma_\alpha^{(s)}(\rho_{\alpha,k} - f_{\alpha,k}^{eq}) \\
&-\mathrm{i}\,\Omega^*(z,t)\tilde{\rho}_{cv,k} + \mathrm{i}\,\Omega(z,t)\tilde{\rho}_{cv,k}^* + \Lambda_{\alpha,k}
\end{aligned}
\tag{2.31}
$$

where $\alpha \in \{v,c\}$, $\rho_c(\rho_v)$ denotes the electron (hole) population density of in the conduction (valence) band, respectively, and $\rho_{cv,k}$ is the off diagonal matrix elements describing the polarisation, $\Lambda$ denotes carrier injection from an external source and $f_{c,k}$ $(f_{v,k})$, $f_{c,k}^{(L)}$ $(f_{v,k}^{(L)})$ and $f_{c,k}^{(eq)}$ $(f_{v,k}^{(eq)})$ are the electron (hole) quasi Fermi distribution functions describing occupations probability for various limiting cases described in the following. Four different relaxation rates, $\gamma_2$, $\gamma_\alpha^{(sc)}$, $\gamma_\alpha^{(h)}$ and $\gamma^{(s)}$ are included, that are associated with distinct relaxation processes. In the following these relaxation processes are described in the order of the typical timescale at which they decay. The processes are also illustrated in figure 2.1
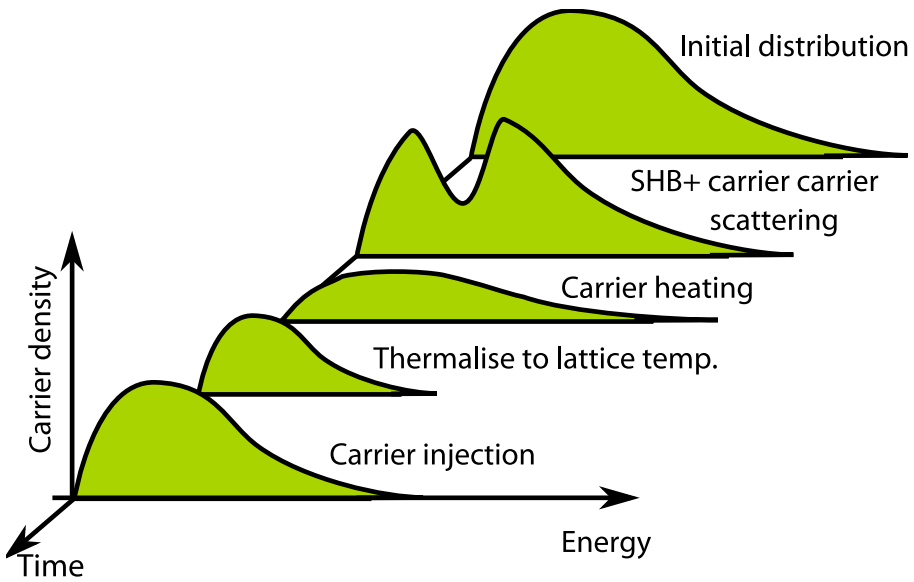
**Figure 2.1:** Illustration of the carrier relaxation processes in a bulk semiconductor. The pulse burns a spectral hole. Carriers are redistributed by carrier-carrier scattering, leading to a heated distribution. The distribution thermalise to the lattice temperature by carrier-phonon scattering and finally the carrier distribution is replenished by external carrier injection.

**Polarization relaxation, $\gamma_2$**

$\gamma_2$ accounts for the relaxation of the polarisation (compare equation 2.21 and (2.28)) and is often denoted dephasing or the homogeneous linewidth. The former notation arise from the modelling of the electron wavefunction, where a random noise term is added to the phase that leads to an exponential decay of the polarisation [9]. The latter notation arise from the measured spectral width of the absorption profile of an ideal 2-level system. In this case, the absorption spectrum is a Lorentzian with a FWHM of $2\gamma_2$. Time resolved measurements often refer to $\tau_2$ that is related to the homogeneous linewidth as $\gamma_2 = \tau_2^{-1}$.

$\gamma_2$ can be separated into the sum of two contributions $\gamma = \gamma^{(\mathrm{pd})} + \Gamma/2$ where $\Gamma$ accounts for all population losses out of $|1\rangle$ and $|2\rangle$ while $\gamma^{(\mathrm{pd})}$ accounts for energy conserving processes, i.e. elastic scattering, and is often denoted "pure dephasing". In cold atomic gasses, $\gamma^{(\mathrm{pd})}$ is often neglected as population decay by far is the dominating decay process. In this case, the dephasing is said to be lifetime limited [72]. For electrons in matter, however, this is generally not the case. Here, phonon interactions are the main contributions to the dephasing [73]. Thus, decreasing the temperature effectively decreases the pure dephasing rate [74, 75, 76, 77], but also reducing the dimensions of freedom of the electrons, effectively diminish the possible phonon interactions due the quantized energy levels. Thus, near population decay limited dephasing has been observed in quantum dot structures at cryogenic temperatures [72, 75, 77, 78, 79]. Semiconductor lasers and amplifiers, on the other hand, typically show a large dephasing rate since they are operated at room temperature and driven at large carrier densities.

**Relaxation of Spectral Hole Burning, $\gamma_\alpha^{(sc)}$ ($\sim 100$ fs)**

As the pulse enters the medium, carriers recombine through stimulated emission near the carrier wavelength, gradually creating a hole in the gain spectrum, a process denoted spectral hole burning (SHB) [80]. Meanwhile, nearby carriers are continually redistributed through intraband carrier-carrier scattering causing a gradual refilling of the spectral hole. The rate at which this occurs is denoted $\gamma_\alpha^{(sc)}$, and differs between electrons and holes, hence the index $\alpha$. In the special case where the stimulated emission rate is much smaller than $\gamma^{(sc)}$, no spectral hole is created and the carrier distribution adiabatically follows a quasi Fermi distribution given by the instantaneous temperature and Fermi energy. The SHB relaxation time in bulk and QW structures is typically on the order of 200 fs [81, 82, 83, 84, 85].

**Relaxation of carrier heating, $\gamma_\alpha^{(h)}$ $\left(0.5 \text{ ps}\right)$**

For the application of lasers or amplifiers, the photon energy is often chosen below the mean energy of the carrier ensemble (where there is a maximum gain). Thus, "cold" carriers are removed through stimulated emission, resulting in a heated remainder of the carrier ensemble. This process is therefore often denoted carrier heating (CH) in literature. In the case of an absorbing medium, there are two regimes of the laser frequency that give rise to carrier cooling and CH, respectively. Choosing the laser frequency smaller than the average carrier energy (but large enough to give absorption), leads to exitation of "cool" (i.e. less energetic) carriers through absorption of the laser field. A laser frequency higher than the mean energy, leads to exitations of "hot" carriers. The inclusion of free carrier absorption (intraband exitations) and two-photon absorption leads to exitation of very energetic carriers for high carrier density and/or high pulse intensities, respectively. This leads to CH for intense fields, regardless of the laser frequency. The heated carriers will slowly equilibrate with the surrounding lattice via carrier-phonon interactions with a distribution function converging towards a Fermi distribution given by the lattice temperature and the corresponding Fermi energy. The characteristic relaxation time of this process is typically on the order 0.5 ps [83, 84, 85, 86].

**Spontaneous decay, $\gamma^{(s)}$**

($\sim$ns) With the carriers having equilibrated with the lattice temperature, the dominating decay process is that through spontaneous emission. Without a pump source injecting new carriers, the carriers would gradually recombine, leaving a small portion in the valence and conduction band due to the finite temperature. The final distribution is described by the Fermi function evaluated at the lattice temperature and the Fermi energy corresponding to the chemical potential. The characteristic time of spontaneous decay rate in bulk is typically on the order of 1 ns. In quantum well and quantum dot media, however, this time may vary significantly depending on the chosen transition due to selection rules [62, 70]. The spontaneous decay rate may even be drastically changed by use of periodic dielectric structure [87] surrounding the active material, as has been shown for quantum well and quantum dot structures [88, 89, 90, 91].

Returning to equations (2.30) and (2.31), it is necessary to evaluate the temperature, $T_\alpha$, and Fermi energy, $\varepsilon_{f,\alpha}$, for the three Fermi distributions, $f_{\alpha,k}$, $f_{\alpha,k}^L$ and $f_{\alpha,k}^{eq}$. These, are found from the equations describing the total energy and carrier density:

$$U_\alpha(t) = \int_0^\infty E \varrho_\alpha(E) f_\alpha(E; \varepsilon_{f,\alpha}(t), T(t)) \, \mathrm{d}E = \frac{1}{V} \sum_k E_{\alpha,k} \rho_{\alpha,k}(t) \qquad (2.32)$$

$$N(t) = \int_0^\infty \varrho_\alpha(E) f_\alpha(E; \varepsilon_{f,\alpha}(t), T(t)) \, \mathrm{d}E = \frac{1}{V} \sum_k \rho_{\alpha,k}(t) \,, \qquad (2.33)$$

where $\varrho$ denotes the density of states function. Notice that the subscript $\alpha$ was dropped for $N$ assuming charge neutrality, i.e. $N_c = N_v$. In principle, one is capable to fully calculate the propagtion of a laser pulse travelling in a semiconductor gain material by solving self-consistently the material and wave equation using (2.29),(2.30),(2.31),(2.32),(2.33) and (2.10), respectively. However, the problem is computationally cumbersome. We shall therefore proceed, making some simplifying assumptions.

### 2.3.1 Adiabatic elimination of the polarisation

For structures operated at room temperature and with an applied current source, the dephasing rate, $\gamma_2$, is typically much larger than any of the other relaxation processes [75, 92]. In this case, $\tilde{\rho}_{cv}$ can be assumed to remain in a steady state, only changing adiabatically by the driving field $\Omega(t)$. Thus we set $\partial_t \tilde{\rho}_{cv} \simeq 0$ and solving for $\tilde{\rho}_{cv}$ we find:

$$\tilde{\rho}_{cv,k}(t) \approx i \, \frac{\Omega_k(z,t) \, (\rho_{c,k}(t) + \rho_{v,k}(t) - 1)}{i \, \Delta_k - \gamma_2}. \tag{2.34}$$

For the population density term, we find by inserting (2.34) into (2.31)

$$\partial_t \rho_{\alpha,k} = -\gamma^{(sc)} (\rho_{\alpha,k} - f_{\alpha,k}) - \gamma^{(h)} (\rho_{\alpha,k} - f_{\alpha,k}^{(L)}) - \gamma^{(s)} (\rho_{\alpha,k} - f_{\alpha,k}^{(eq)}) +$$
$$- \frac{2}{\gamma_2} \frac{\gamma_2^2}{\Delta_k^2 + \gamma_2^2} \, (\rho_{c,k}(t) + \rho_{v,k}(t) - 1) \, |\Omega_k|^2 + \Lambda_{\alpha,k} \tag{2.35}$$

In this case there is no coherent coupling between light and matter, thus, the notation of a material gain coefficient is meaningfull[2] and defined as

$$g(t)|_{\omega_0} = -\frac{\omega_0}{c n_0} \chi''(t) \tag{2.36}$$

as can be seen from equation (2.16). Using (2.6), (2.11), (2.12) and (2.34) we get:

$$g(z,t)|_{\omega_0} = -\frac{\omega_0}{\varepsilon_0 n_0} \frac{1}{V \mathcal{E}(z,t)} \, \text{Im} \left( \sum_k \mu_k \tilde{\rho}_{cv,k} \right) \tag{2.37}$$

$$= \frac{\omega_0}{\varepsilon_0 n_0} \frac{1}{V \mathcal{E}(z,t)} \, \text{Im} \left( \sum_k \mu_k \, i \, \frac{\Omega_k^*(z,t) \, (\rho_c + \rho_v - 1)}{i \, \Delta_k - \gamma_2} \right) \tag{2.38}$$

$$= i \frac{\omega_0}{\varepsilon_0 n_0 \hbar} \frac{1}{V} \, \text{Im} \left( \sum_k \mu_k^2 \, \frac{(\rho_{c,k} + \rho_{v,k} - 1)}{i \, \Delta_k - \gamma_2} \right) \tag{2.39}$$

$$= \frac{\omega_0}{\varepsilon_0 n_0 \hbar \gamma_2} \frac{1}{V} \sum_k \mu_k^2 \, \frac{\gamma_2^2}{\Delta_k^2 - \gamma_2^2} \, (\rho_{c,k} + \rho_{v,k} - 1) \,. \tag{2.40}$$

---

[2]Consider the other case, where there is no dephasing. In this case there is a coherent coupling between the light field and the charge carriers giving Rabi oscillations of the population inversion $\rho_{c,k} + \rho_{c,k} - 1$. Thus, the amplification in a thin slice $\delta z$ of material can lead to either complete absorption ($\pi$-pulse), or full transparency ($2\pi$-pulse) [9] depending on the field strength and duration. In this case the gain is not well defined.

Approximating the Lorentzian $\gamma_2^2/(\Delta_k^2 - \gamma_2^2)$ by a unity square function with the same area[3], we only consider stimulated emission from those carriers with a transition energy on resonance with the laser frequency. The rest of the carriers only contribute to the gain through population relaxation into the optically coupled region. Furthermore, assuming $\mu_k$ constant for the optically coupled transitions we get:

$$g(z,t)|_{\omega_0} \approx \frac{\omega_0}{\gamma_2 \varepsilon_0 n_0 \hbar} \mu^2 (n_c + n_v - N_0) \tag{2.41}$$

$$\equiv \frac{a_N}{v_g}(n_c + n_v - N_0) \tag{2.42}$$

where $N_0$ is the (spatial) density of optically coupled states, $n_c = V^{-1}\sum_k \rho_{c,k}$ and $n_v = V^{-1}\sum_k \rho_{c,k}$ are the density of optically coupled carriers in the conduction and valence band, repectively. We shall refer to these as the local carrier density. The rate equations of $n_c$ and $n_v$ are evaluated from (2.35) by summing over the optically coupled states and divide by the volume $V$. Replacing the Lorentzian by a unity square function we get:

$$\partial_t n_\alpha = -\gamma_\alpha^{(sc)}(n_\alpha - \langle n_\alpha \rangle) - \frac{2|\Omega(z,t)|^2}{\gamma_2}(n_c + n_v - N_0) \tag{2.43}$$

where $f_{\alpha,k}$ was assumed constant within the optically coupled region, the injection $\Lambda_{\alpha,k}$ was neglected and

$$\langle n_\alpha \rangle = N_0 f_\alpha(\hbar\omega_0; \varepsilon_f, T_\alpha). \tag{2.44}$$

Furthermore, terms describing the slow relaxation towards $f_\alpha^{(L)}$ and $f_\alpha^{(eq)}$, where neglected. These relaxation terms, still indirectly affect the carrier dynamics, as they are used when calculating the instantaneous Fermi energy $\varepsilon_f$ and temperature $T$ of the Fermi function $f_\alpha$ used in (2.44). The Fermi energy and temperature are found from the instantaneous total carrier density, $N$, and energy, $U_\alpha$. The rate equation of $U_\alpha$ and $N$ are found by differentiatin (2.32) and (2.33) and using (2.35) giving:

$$\partial_t N = -\gamma^{(s)} N - \frac{2|\Omega(z,t)|^2}{\gamma_2}(n_c + n_v - N_0) + \frac{I}{eV} \tag{2.45}$$

$$\partial_t U_\alpha = -\gamma^{(h)}(U_\alpha - U^{(L)}) - \gamma^{(s)} U_\alpha - E_{\alpha,k_0}\frac{2|\Omega(z,t)|^2}{\gamma_2}(n_c + n_v - N_0) \tag{2.46}$$

where $I$ is the applied current. Here, we assumed $\sum_k f_k^{(eq)} \approx 0$ and the term $\sum_k E_{\alpha,k}\Lambda_{\alpha,k}$ was neglected. The former assumption implies that thermal effects at equilibrium does not lead to a significant filling of electrons or holes in the conduction and valence band, respectively, while the latter states that the carrier injection rate into each $k$ state is assumed lower than all other decay processes. Noting that $\gamma^{(h)} \gg \gamma^{(s)}$ we can neglect the term $U_\alpha\gamma^{(s)}$. Finally,

---

[3]I.e. a function $f$, where $f(\Delta) = 1$ for $2|\Delta_k| < \int_{-\infty}^{\infty} \gamma_2^2/(\Delta_k^2 - \gamma_2^2)\,\mathrm{d}\Delta_k$ and $f(\Delta) = 0$ otherwise.

identifying $\frac{2|\Omega(z,t)|^2}{\gamma_2}(n_c + n_v - N_0) = v_g g(t)\mathcal{S}(z,t)$ we summarise the complete set of equations describing the carrier dynamics:

$$\partial_t n_\alpha = -\gamma_\alpha^{(sc)}(n_\alpha - \langle n_\alpha \rangle) - v_g g(t)\mathcal{S}(z,t) \tag{2.47}$$

$$\partial_t N = -\gamma^{(s)}N - v_g g(t)\mathcal{S}(z,t) + \frac{I}{eV} + \frac{\Gamma_2}{\Gamma}v_g\beta_2\mathcal{S}(z,t)^2 \tag{2.48}$$

$$\partial_t U_\alpha = -\gamma^{(h)}(U_\alpha - U^{(L)}) - E_{\alpha,\hbar\omega_0}v_g g(t)\mathcal{S}(z,t) + $$
$$+ \frac{\Gamma_2}{\Gamma}v_g\beta_2 E_{\alpha,2\omega_0}\mathcal{S}(z,t)^2 + \sigma_\alpha\hbar\omega N \tag{2.49}$$

where two photon loss (TPA) was included phenomenologically in the equation for $U_\alpha$ and $N$, through the TPA coefficient $\beta_2$. Furthermore, intra band carrier excitations where added phenomenologically through the free carrier scattering cross section $\sigma_\alpha$ in the expression for $U_\alpha$. With the inclusion of TPA and waveguide loss (WGL) the wave equation takes form:

$$\frac{1}{v_g}\partial_t\mathcal{S}(z,t) + \partial_z\mathcal{S}(z,t) = (\Gamma g(t) - \alpha_{int})\mathcal{S}(z,t) - \beta_2\mathcal{S}(z,t)^2, \tag{2.50}$$

where $\Gamma$ is the confinement factor.

Equation(2.50) together with (2.47),(2.48) and (2.49) form a complete set of equations to describe the propagation of an optical electric field traveling in an semiconductor medium.

### 2.3.2 Gain dynamics and pulse propagation examples

In the following, some examples of the gain dynamics and pulse propagation in an absorbing and amplifying medium are presented based on numerical solutions to (2.47),(2.48), (2.49) and (2.50). The used parameters are based on estimated values from measurements on an SOA presented in chapter 4, with $\alpha_{int} = 4.8$ cm$^{-1}$ and $\beta_2 = 45$ cm/GW with a small-signal gain of either 32.2 cm$^{-1}$ or $-116$ cm$^{-1}$. The pulse intensity FWHM is 150 fs. Other parameters are presented in table 4.3. For the following discussion we denote the relaxation time constants $\tau_\alpha^{(i)} = 1/\gamma_\alpha^{(i)}$, e.g. $\tau_v^{(sc)} = 1/\gamma_v^{(sc)}$,

In figure 2.2, the calculated temporal dynamics of the local carrier density, gain and temperature is seen plotted for an amplifying medium for various input energies For the lowest energies 0.1 pJ and 1 pJ, the temporal carrier dynamics are seen to be close to the linear regime. I.e. the change of the local carrier density scales almost linearly with the pulse energy. Here the gain initially drops due to SHB, leading to CH. After this, the local density rapidly increase with two time constants: The fast carrier-carrier scattering $\tau_\alpha^{(sc)}$ and "slow" temperature equilibration $\tau_\alpha^{(h)}$. Where the latter process is clearly revealed in the decreasing temperature. As the pulse energy is further increased, both CH, TPA and free carrier absorption starts to appear that are particular clearly seen for the hole dynamics at 10 pJ. At $t = 0$, it is mainly TPA that causes the narrow dip in the local carrier density. Within the scattering time, $\tau^{(sc)}$, the carrier ensemble equilibrate to a quasi Fermi distribution with a strongly
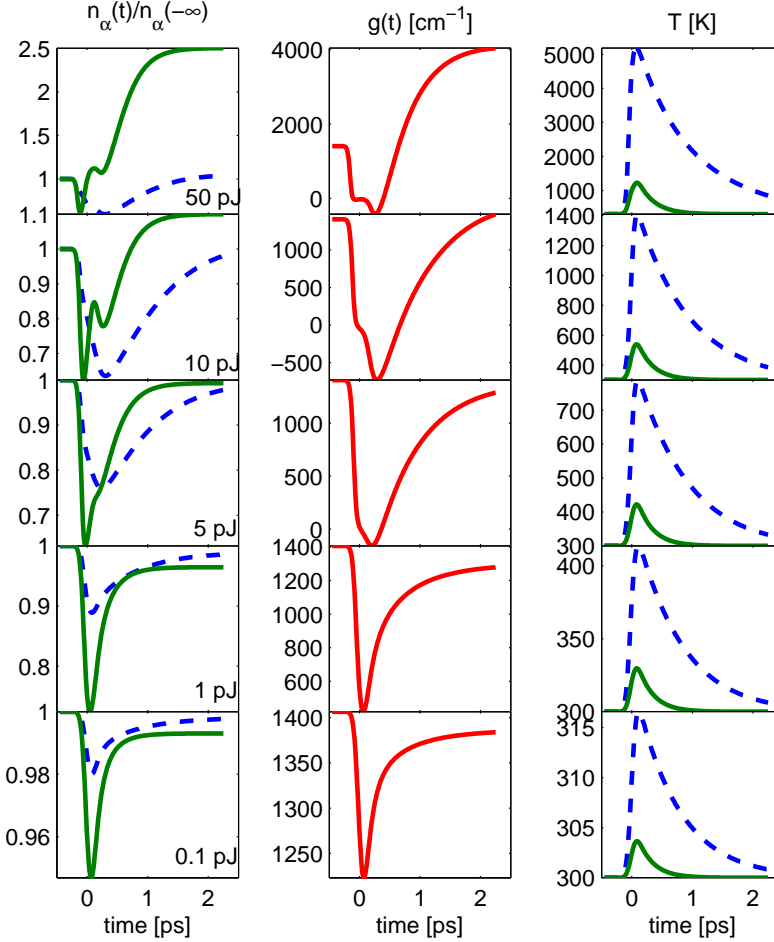
**Figure 2.2:** Example of calculations from solving (2.47), (2.48) and (2.49) for the pulse energies $E_{in} = \{50\text{ pJ}, 10\text{ pJ}, 5\text{ pJ}, 1\text{ pJ}, 0.1\text{ pJ}\}$ (rows from top to bottom) and a small signal modal gain of $32.2$ cm$^{-1}$. Pulse envelope is centered around 0 ps with a FWHM 150 fs. (Left column): Carrier density of electrons (dashed) and holes (solid) normalized by the initial carrier density. (Middle): Calculated gain using 2.42 in units of cm$^{-1}$. (Right): Temperature calculated from numerically solving (2.32) (2.33). Chosen parameters are $\alpha = 4.8$ cm$^{-1}$ and $\beta_2 = 45$ cm/GW. Other parameters are shown in table 4.3.

heated ensemble owing to the energetic carriers from TPA and free carrier absorption, which is seen as the second dip in the local hole density. A second dip is not clearly seen for the electrons, since the decrease due to heating is much stronger owing to the smaller effective mass. The dip from TPA is thus not clearly resolved. The ensemble gradually cools, leading to an increasing local carrier density that eventually goes above the initial carrier density due to the initial carrier pumping by TPA and free carrier absorption processes.

The same type of calulations are illustrated in figure 2.3 only for an absorbing medium. Inspecting the temperature at low input energies, it is seen that
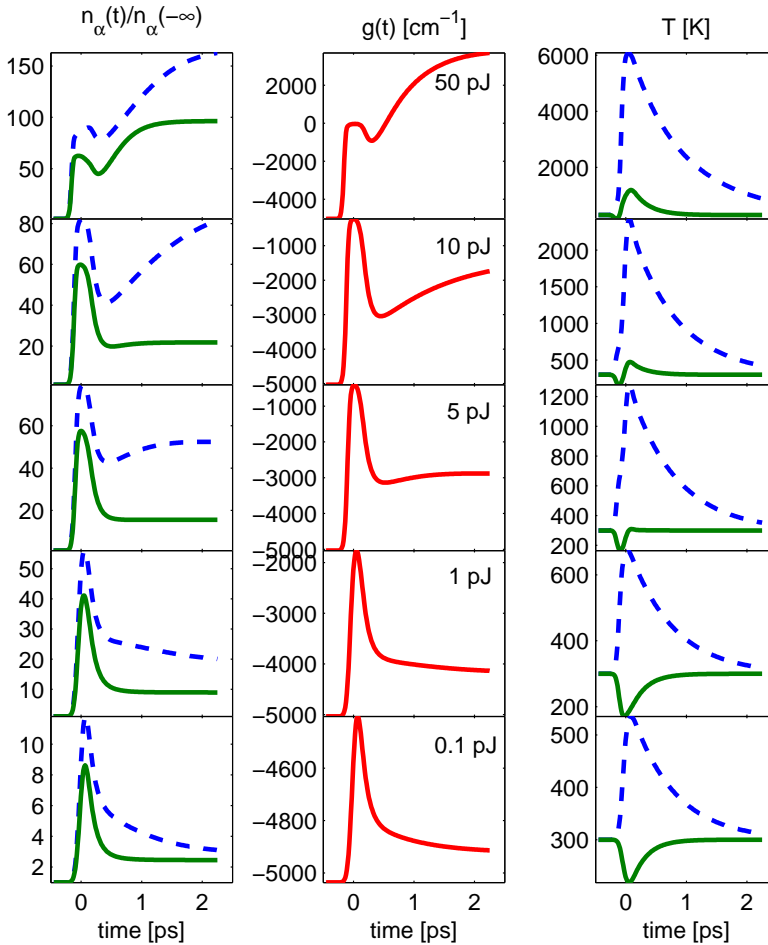


**Figure 2.3:** Similar calculation as presented in figure 2.2, only for an absorbing medium with small signal modal gain of -116 cm$^{-1}$.

the hole ensemble is cooled, while the electrons are heated. This corresponds to a laser frequency that is resonant with electron(hole) states with a larger(lower) energy than the mean electron(hole) energy[4]. As the pulse energy is increased, both electrons and holes are heated due to the excitation of highly energetic carriers from TPA and free carrier absorption. The increasing TPA and free carier absorption are also seen to affect the gain, where the slope changes sign from negative to positive between 1 pJ and 5 pJ for times $t > 0.6$ ps.

In figure 2.4, the temporal dynamics of the absorbing medium as a function of propagation length is seen plotted for a 2 pJ pulse entering an absorbing medium. The same parameters are used as for the results in figure 2.3. As the pulse enters the medium ($z = 0$ $\mu$m), the absorption is strongly saturated, but as the pulse is gradually absorbed through the material, the degree of saturation is seen to drop. The absorption of carriers leads to a strong heating as seen from the plotted temperature (bottom, left). At the first part of the propagation, the heating is due to absorption of "hot" carriers, but also TPA and free carrier absorption. As discussed above, the highly energetic carriers from TPA and free carrier absorption processes slowly decay back into the optically coupled region, as is seen from the slightly increasing modal gain and local carrier density for $\tilde{t} > 0.5$ at $z \sim 0$ $\mu$m. As the probe is gradually absorbed through the material, eventually only resonant carrier excitations occur. This is also clearly seen from the temperature along $t = 0$. For the first propagation length $T$ drops with a steep slope due to decreasing TPA and free carrier absorption. As the pulse is signficantly attenuated, TPA and free carrier absorption cease and as a result the slope near the middle section is seen to flatten.

The intensity envelope associated with figure 2.4 is seen plotted in figure 2.5 as a function of propagation length. For clarity, the envelope at each point $z$, have been normalised by the peak intensity. Here, it is clear seen that the pulse is shaped as it propagates through the material, leading to a shift towards positive times. Furthermore the pulse is seen be compressed slightly. As we shall see in chapter 4 this can be exploited for achieving a pulse delay or advancement.

### 2.3.3 Comments on the rate equations

The main simplifications made to describe the carrier dynamics in (2.47),(2.48) and (2.49) was the adiabatic elimination of the polarization and the substitution of a Lorentzian function of width $\gamma_2$ with a unity square function. This reduced the complexity of the initial task considerably, however, the numerical calculations of the gain dynamics are still somewhat ponderous. Especially the evaluation of the instantaneous Fermi energy and effective temperature needed for $\langle n_\alpha \rangle$, which are calculated self consistently from equations (2.33) and (2.32), increase the computation time considerably. Since $U_\alpha$ is a function of $N$ and

---

[4]As pointed out in [61], the condition for cooling is $\partial_N U_\alpha|_{T_\alpha} < E_{\alpha,\hbar\omega_0}$. Thus, for these calculations, $\partial_N U_v|_{T_v} < E_{v,\hbar\omega_0}$ while $\partial_N U_c|_{T_c} < E_{c,\hbar\omega_0}$.
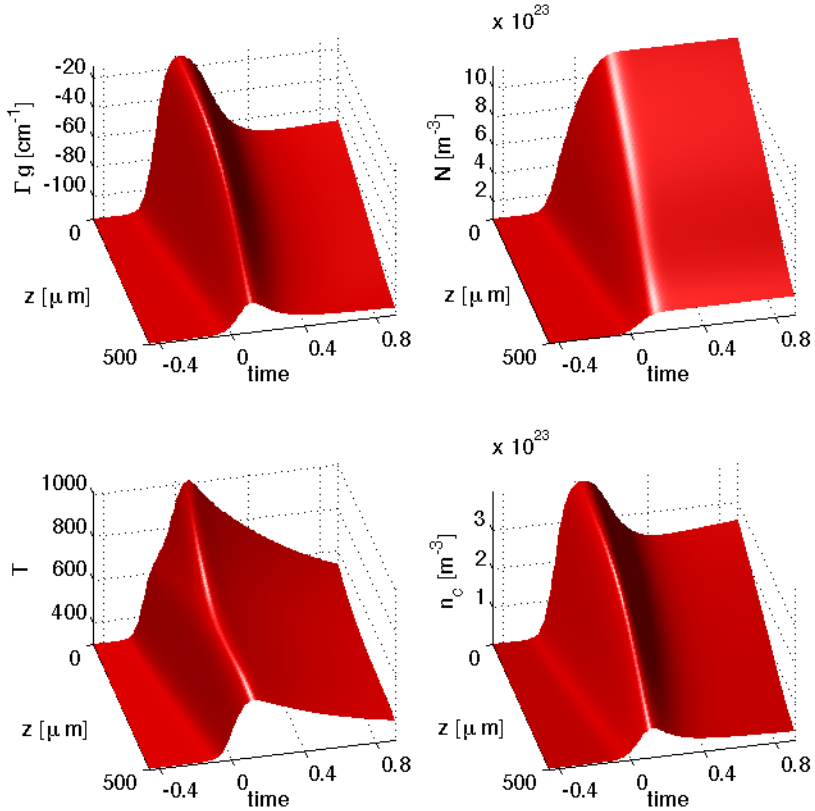
**Figure 2.4:** Calculated carrier dynamics as a function of time and propagation length for an absorbing medium. The time used is given in the frame moving at the group velocity of the pulse, i.e. $\tilde{t} = t - z/v_g$. Plots showed are (top,left) modal gain $[\text{cm}^{-1}]$, (top,right) carrier density, (bottom,left) conduction band temperature [K], (bottom,right) local electron density. Chosen parameters are presented in table 4.3.
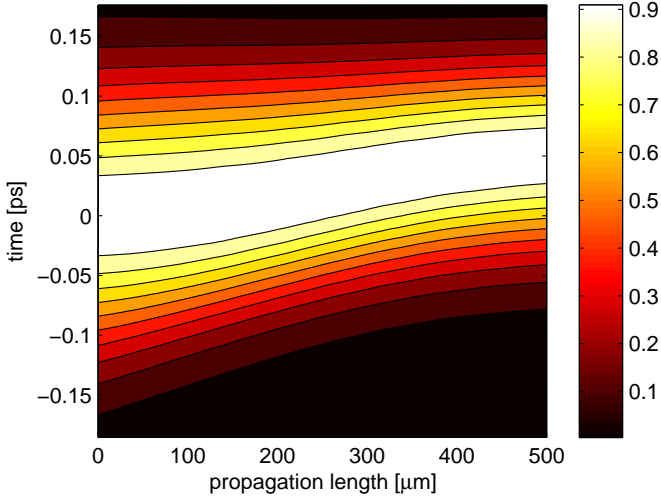
**Figure 2.5:** Normalized pulse envelope as a function of propagation length and time. The time is given in the frame moving at the group velocity of the pulse, i.e. $\tilde{t} = t - z/v_g$. Parameters are presented in table 4.3.

$T_\alpha$, we may write [61]

$$\frac{\partial U_\alpha}{\partial t} = \frac{\partial U_\alpha}{\partial N} \frac{\partial N}{\partial t} + \frac{\partial U_\alpha}{\partial T_\alpha} \frac{\partial T_\alpha}{\partial t} \tag{2.51}$$

Solving for $\partial_t T_\alpha$, leads to a rate equation for the temperature. Thus, the task is reduced to determining the Fermi energy from the $N(t)$, where approximations with analytical expressions exist [62]. For the work presented in chapter 4, gain saturation effects are investigated at high input pulse energies. In this case, a linear expansion of $U_\alpha$ breaks down, and this technique was therefore not used for this work.

The rate equation model, has proven effective for describing the ultra fast gain dynamics of bulk and QW SOAs [64, 81, 82, 86]. For quantum dots on the other hand, quantized carrier states prohibit the redistribution of carriers into continuous quasi Fermi distribution functions, thus, the concept of CH is no longer meaningful. Nevertheless, the CH terminology is sometimes used in literature on characterization of large QD SOAs [93, 94], because the measured gain dynamics show features similar to the footprint of CH and SHB. For small QDs, however, it is in principle necessary to solve the full density matrix of all energy levels in the quantum dots which requires full knowledge of all inter-level relaxation rates and dipole moments. With small QDs, allowing only a few electron and hole states, these parameters can be deduced from experiments [72, 75, 77, 78, 95, 96, 97, 98, 99, 100] as well as from simulations [101]. However, for quantum dot SOAs and lasers operating near 1.55 $\mu$m, the average quantum dot size leads to a rich spectrum of states [93, 94, 102, 103], that

makes deduction of the dipole moment and decay rate of all possible channels a truly daunting task. Complicating matters further, the large inhomogeneous broadening, that is mainly caused by fluctuating quantum dot sizes, needs to be taken into account when calculating the gain dynamics. A simplifying technique is to approximate the hole density of states as being continuous [104]. The heavier mass of the heavy holes compared to the electrons, leads to more eigenstates with smaller level-spacing that can be approximated by a continuous density of states. The gain dynamics are then calculated from the coupling of a single electron state to the continuum of hole states.

## 2.4 Simple gain saturation model

For the experimental pulse delay measurements in chapter 4, a qualitative comparison between measurements and simulations, based on the rate equation model as described in section 2.3, is useful for identifying contributions to the gain dynamics. However, for extraction of physical parameters, e.g. by fitting, the numerical calculations become too extensive. In the following we shall derive a simplified equation describing the pulse propagation, based on approximations of the rate equation model from section 2.3.

In equation (2.47), the term $\langle n_\alpha \rangle = N_0 f_\alpha(\hbar\omega_0; \varepsilon_{f,\alpha}(t), T_\alpha)$ was determined from the instantaneous Fermi destribution, that gradually changes due to resonant carriers that recombine and off resonant carriers that are redistributed. Instead, considering a medium where the differential gain $\partial_N g$ is very low. This implies that the gain is hardly changed after transmission of the pulse. Thus, the *instantaneous* Fermi function can be exchanged with the *constant* Fermi function describing the carrier distribution before the pulse have entered the medium, $f(\hbar\omega_0; \bar{\varepsilon}_{f,\alpha}, T_L)$, where $\bar{\varepsilon}_\alpha = \varepsilon_{f,\alpha}(t \to -\infty)$. With this assumption, equations (2.47),(2.48) and (2.49) are substituted by a single equation given as:

$$\partial_t n_\alpha = -\gamma_\alpha^{(sc)}(n_\alpha - \bar{n}_\alpha) - v_g(n_c + n_v - N_0)\mathcal{S} \qquad (2.52)$$

where $\bar{n}_\alpha = N_0 f_\alpha(\hbar\omega_0; \bar{\varepsilon}_\alpha, T_L)$. The physical picture of this, is that as the pulse enters the medium, it will gradually burn a spectral hole in the carrier distribution. Meanwhile, the off resonant carriers will start redistributing and refill the spectral hole. Since the gain change was assumed small, the local carrier density is almost completely recovered. This assumption is valid in a bulk and QW medium for laser frequencies close to the band edge. In this case, the change of optically coupled carrier density $\delta n_\alpha$, is much smaller compared to the total carrier density $N$. This is illustrated in figure 2.6, where the gain spectrum is plotted at times $t \gg 1/\gamma^{(sc)}$ but much shorter than the time it takes the gain to fully recover due to the carrier injection[5]. At higher frequencies, the change of gain becomes significant and the model is no longer a good

---

[5]The total carrier density is eventually fully restored due the external current source. This occurs on a much longer time scale ($\sim 100$ ps)
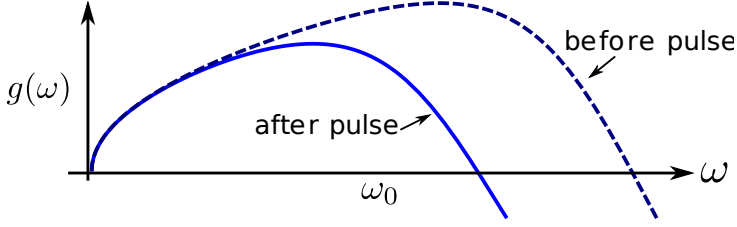
**Figure 2.6:** Illustration of the initial gain the gain spectrum (dashed), and the gain spectrum at times $1/\gamma^{(sc)} \ll t$ after the pulse having passed through the medium. At frequencies close to the bandgap, the gain is almost fully recovered, whereas for large frequencies, the gain is significantly suppressed.

approximation. The model may also be well suited for simulating the gain dynamics in a QD medium. QD SOAs have been demonstrated having a very fast initial gain recovery time [57, 105]. This comes from the fact that the resonant energy levels are being refilled by higher quantised states that acts as a carrier reservoir. In this case, the material gain is fully recovered within $\sim 2 \, \text{ps}^6$ pulse. Writing equation (2.52) in terms of the gain coefficient $g = \frac{a_N}{v_g}(n_c + n_v - N_0)$ and the pulse intensity $\mathcal{I}(z,t) = \hbar\omega v_g S(z,t)$ gives:

$$\partial_t g = -\left(\gamma^{(sc)} + 2\frac{a_N}{v_g \hbar \omega_0}\mathcal{I}\right)g + \gamma^{(sc)}g_0 \tag{2.53}$$

where $g_0 \equiv \bar{n}_c + \bar{n}_v - N_0$ is the initial material gain, also known as the small signal gain and it was assumed $\gamma_v^{(sc)} = \gamma_c^{(sc)}$. Equation (2.53) is an inhomogeneous linear differential equation with the solution[106]:

$$g(t) = e^{-\int_{-\infty}^{t} p(z,t')\,dt'}\left[\int_{-\infty}^{t}\gamma^{(sc)}g_0\, e^{\int_{-\infty}^{t'} p(z,t'')\,dt''}\,dt' + g_0\right] \tag{2.54}$$

where $p(z,t) \equiv \gamma^{(sc)} + 2\frac{a_N}{v_g \hbar \omega_0}\mathcal{I}(z,t)$ and $g_0$ denotes the small signal material gain. In the limit where the scattering relaxation time is much greater than the pulse width, $1/\gamma^{(sc)} \gg \tau_p$, equation (2.54) reduces to [107, 108]

$$g(t) = g_0\, e^{-E_{\text{sat}}^{-1}\int_{-\infty}^{t}\mathcal{I}(z,t')\,dt'} \tag{2.55}$$

where the parameter $E_{\text{sat}} \equiv v_g \hbar \omega_0/(2a_N)$ is denoted the saturation energy and identified as the required pulse energy per unit area for which the material gain is decreased by $1/\text{e}$ assuming $1/\gamma^{(sc)} \gg \tau_p$. Calculations of $g(t)$, based on equation (2.54), is seen in figure 2.7 for various values of $\gamma^{(sc)}$. The pulse energy, $E_p$, was set equal to the saturation energy, except for the calculations seen as a dotted line, where $E_p = 0.7E_{\text{sat}}$ and $\gamma^{(sc)} = 0$. For $\gamma^{(sc)} = 0$ the

---

[6]Here communication based signals are not considered, where pulses are coming one after another. In this case, the higher lying quantised states are eventually emptied leading to gain supression of the signal.
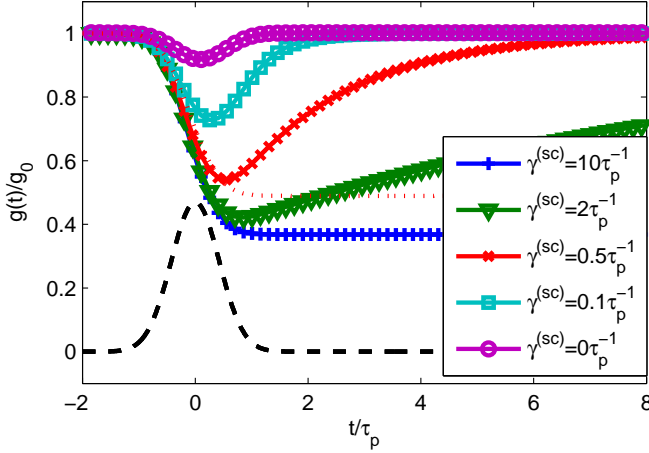
**Figure 2.7:** Example of gain dynamics based on equation (2.54) for various values of $\gamma^{(sc)}$. The pulse envelope is seen plotted with dashed lines. The pulse energy was set equal to the saturation energy $E_{\text{sat}}$, except for the dotted line, where $E_{\text{p}} = 0.7 E_{\text{sat}}$ and $\gamma^{(sc)} = 0$.

gain is seen to decline to $g_0/e$. For increasing $\gamma^{(sc)}$, the gain is more and more rapidly recovered, while the extend of saturation decreases.

From comparison with the calculated gain dynamics using the full rate equations, equation (2.54) was seen fairly accurate for times in the vicinity of the pulse, using moderate scattering rates, $\tau^{(sc)} \gtrsim \tau_p$. Even so, for the measurements in chapter 4, the further simplifying assumption $\tau^{(sc)} \gg \tau_p$ that leads to equation (2.55) is used to fit the experimentally measured transmission, in order to keep the number of fit parameters to a minimum. This is justified by comparing the calculated gain in figure 2.7 for $E_{\text{p}} = E_{\text{sat}}$ and $\gamma^{(sc)} = 0.5\tau_p^{-1}$ (red line) and for $E_{\text{p}} = 0.7 E_{\text{sat}}$ and $\gamma^{(sc)} = 0\tau_p^{-1}$ (red dotted). In the vicinity of the pulse, the two lines are seen to closely follow each other, hence, the induced pulse shaping are similar for the two cases. This is easily understood from the fact that when $\gamma^{(sc)} > 0$ s, it requires additional energy to deplete the number of resonant carriers due the simultaneous refilling from scattered carriers.

### 2.4.1 Pulse propagation

The simple expression for the gain in equation (2.55), allows for swift propagation calculations of an optical pulse using equation (2.50). Transforming the space and time variables in (2.50), to the reference frame moving with the group velocity of the pulse with center at the peak of the envelope, i.e. $(t, z) \mapsto (\tilde{t}, \tilde{z}) = (t - z/v_g, z)$ allows us to simplify (2.50) to:

$$\partial_z \mathcal{I}(\tilde{t}) = \Gamma g_0 \, e^{-E_{sat}^{-1} \int_{-\infty}^{t} \mathcal{I}(t') \, dt'} - \alpha_{\text{int}} \mathcal{I} - \beta_2 \mathcal{I}^2 \qquad (2.56)$$

where an unsaturable loss term, $\alpha_{\text{int}}$, was added, corresponding to waveguide losses.

An example of a pulse propagated 500 $\mu$m in an amplifying and in an absorbing material is seen plotted in figure 2.8. The propagated pulse envelope,
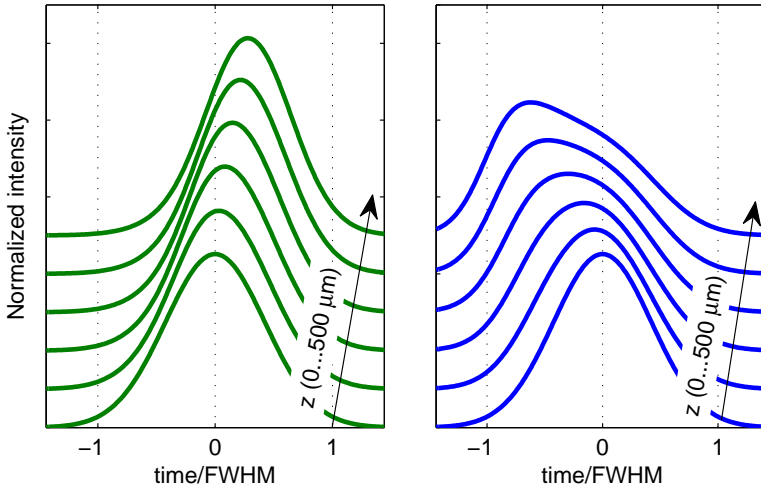


**Figure 2.8:** Calculated pulse envelopes at various propagation lengths in steps of 100 $\mu$m for an absorbing (left) and an amplifying (right) medium. The calculations are based on equation (2.55) with $\Gamma = 1$, $g_0 = \pm 60$ cm$^{-1}$ $\alpha = 10$ cm$^{-1}$, $E_p = 7 E_{\text{sat}}$ (left), $E_p = 3.5 E_{\text{sat}}$ and $\beta/A = 43$ m$^{-1}$W$^{-1}$ where $A$ is the transverse mode area.

normalised by its pulse energy, is plotted at increasing propagation lengths, in steps of 100 $\mu$m, shifted vertically for clarity. For the case of an absorbing medium, the peak amplitude is gradually shifted towards positive times, implying an effective delay of the pulse. This is also observed in figure 2.5 using the full rate equation model. Similarly, a positive gain implies an effective advancement, however, in this case, two photon absorption becomes increasingly dominating as the pulse is amplified through the medium. As a result, the pulse is subject to significant broadening at $z = 500$ $\mu$m.

The calculated transmission and pulse delay are shown plotted in figure 2.9 as a function of the input pulse energy for an absorbing and amplifying device. Starting out by considering the simulations neglecting WGL and TPA (dashed
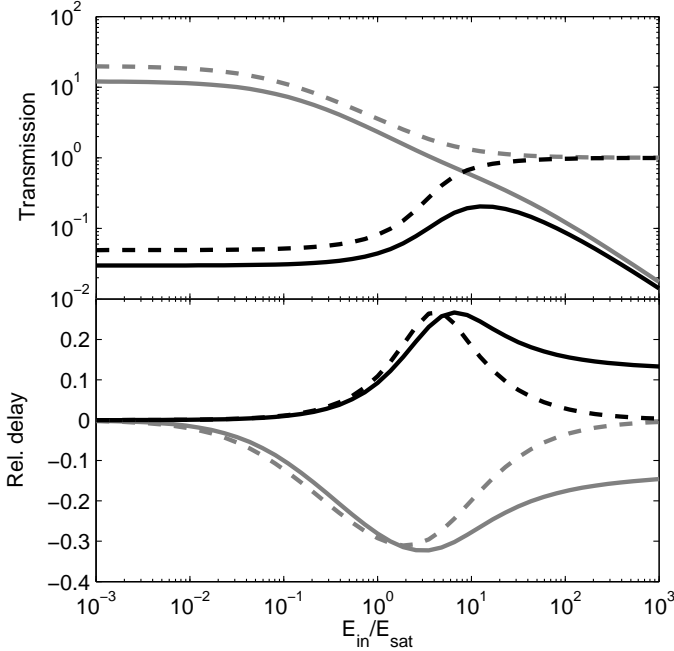


**Figure 2.9:** Transmission (top) and pulse delay (bottom) relative to the pulse FWHM as a function of input pulse energy, for an amplifying (grey) and an absorbing medium (black) with $g_0 = \pm 60$ cm$^{-1}$. Other parameters as in figure 2.8. Solid and dashed lines represent calculations, based on equation (2.55), with and without waveguide losses and two photon absorption, respectively

line) it is seen that as the input pulse energy is increased, the transmission starts to saturate. This leads to the expected delay for the absorbing medium and advancement for the amplifying medium. Here, the delay, $\delta t$ is calculated from the statistical mean, i.e. $\delta t = \int \mathcal{I}_{\text{out}}(t)t\,\mathrm{d}t / \int \mathcal{I}_{\text{out}}(t)\,\mathrm{d}t$, where $\mathcal{I}_{\text{out}}(t)$ is the output envelope. When increasing the input pulse beyond $E_{sat}$, the transmission is seen to converge towards unity. Furthermore, the transmission of the amplifying device is seen to saturate at lower input pulse energies compared to the absorbing one. E.g. a pulse slightly below the saturation energy is gradually amplified above the saturation energy causing the material gain to saturate at the end of the device. For the absorbing device, the pulse energy decreases while propagating down the device. Hence, saturating the transmission requires a pulse energy stronger than the saturation energy. For the same reason, in literature, one distinguish between the input and output saturation energy, e.g the energy at which the transmission through the first fraction of

the waveguide or the full length of the waveguide has dropped by $1/\mathrm{e}$, respectively. Accordingly, the output saturation energy is lower (higher) than the input saturation energy for an amplifying (absorbing) medium. Concerning the pulse shift, increasing the pulse energy initially leads to an increasing delay/advancement. However, at the highest pulse energies, the medium is instantly saturated causing the front and tail of the pulse to experience the same amplification/absorption. As a result, no net delay is achieved.

When including TPA, the transmission decreases for increasing input pulse energy at the highest input energies with asymptote $1 - \beta L/E_{in}$, where $L$ is the device length. This, most notably, results in pulse broadening, but also the delay no longer converges towards zero. This can be understood in the limit of very strong pulse where TPA dominates. In this case, the peak intensity of the pulse is, within the very first part of the medium, decreased to a level where TPA is no longer dominating. If the resulting pulse energy is close to the saturation energy, the remaining part of the waveguide induces an overall delay as described above. Increasing the pulse energy does not significantly change the delay, as TPA causes the pulse to become flat with a peak intensity and pulse energy almost independent of the initial pulse energy.

# CHAPTER 3

# Experimental setup

In this chapter we describe the laser setup and the measurements techniques used for the experiments in chapter 4 and 6.

## 3.1 Laser setup

The laser setup, used for the experiments in chapter 4 and 6, generates Fourier limited pulses with a minimum duration of 150 fs at a repetition rate of 250 kHz, and is capable of being tuned from 930 nm - 2.3 $\mu$m. A fairly large tuning capability is essential for the setup, since different device material and structures call for a large span of wavelength. The tuning is achieved using optical nonlinearities, that require very strong pulses. Thus, the laser setup consist of three parts: A mode-locked laser for generating short optical pulses, a regenerative amplifier for amplifying the laser pulses, and an optical parametric amplifier for wavelength tuning.

### 3.1.1 Mode-locked laser

The mode-locked laser is a Coherent Mira 900 Ti:Sapphire laser [1] that is pumped by a 5 W Verdi laser at 532 nm. Mode locking is achieved by a Kerr lense mode locking scheme [109], generating output pulses tunable between 700 nm and 980 nm with a maximum duration of 200 fs. Both the Ti:Sapphire crystal and the diode-pack of the verdi laser are water cooled at 15°. For the work presented in this thesis, the carrier frequency is fixed at 798 nm to ensure the best performance of the regenerative amplifier. The pulse duration is approximately 150 fs with a repetition rate of 78 MHz and an average output power of 700 mW. The output power of the Mira is, for this work, of minor

---

[1] $Al_2O_3$ doped with titanium

importance, since the subsequent amplifier ensures sufficiently strong pulses. Therefore, a beamsplitter is used for reflecting 25% for use in the amplifier, thus allowing for simultaneous use of the remaining 75% elsewhere (e.g. an autocorrelator). However, for proper operation of the regenerative amplifier, a stable signal both in terms of amplitude as well as repetition rate is required. Thus, in the day to day work, much time is spent optimising the cavity in order to ensure maximum stability.

### 3.1.2 Regenerative amplifier

The pulses from the Ti:Sapphire laser is injected into a regenerative amplifier (RegA). The amplifier is a Coherent RegA, with Ti:Sapphire as gain medium that is pumped by a continous wave 10 W Verdi laser at 532 nm. Amplification is achieved by cavity Q-switching [109, 110], in which single pulses are picked out and injected into the cavity of the RegA by opening a port using an electro-optical switch. The port is opened in a time window less than the roundtrip time, ensuring that the injected pulse remains within the cavity. For each roundtrip, the pulse is amplified by the Ti:Sapphire crystal. After several roundtrips ($\approx 20$), the gain saturates and the pulse does not become any stronger. The GVD acquired through the Ti:Sapphire crystal and Q-switch leads to pulse durations of 20 ps, and is compensated by a grating based pulse compressor before the exit of the pulse. At this point, the output port is re-opened, the amplified pulse is ejected and the port is subsequently closed to recover the gain of the Ti:Sapphire crystal. The time it takes for the gain to fully recover sets the upper limit of the repetition rate. To ensure proper synchronization with the Mira, the RegA is fed with a signal from a diode detector measuring the pulse train inside the cavity of the Mira. If the diode signal suffers from noise due to poor alignment of the Mira, it is very difficult getting the RegA to operate acceptably. The output repetition rate from the RegA has a maximun of 295 kHz, but is typically run at approximately 250 kHz, with an average output power of 700 mW and an intensity FWHM of 150 fs. It is noticed that even though only approximately every 312th pulse is amplified, the average output is approximately the same as for the output of the Mira laser. This implies very strong pulses with energy of approximately 4 $\mu$J and a peak intensity of roughly 18 MW.

### 3.1.3 Optical Parametric Amplifier

The output from the Rega, is injected into an optical parametric amplifier (OPA). The OPA works by splitting the beam into two paths. One is frequency doubled to approximately 400 nm by second harmonic generation[5] in a $\beta-\text{BaB}_2\text{O}_4$ (BBO) crystal acting as a pump. The other is focused onto a sapphire crystal. The high peak intensity inside the sapphire crystal is further enhanced by kerr induced self focusing. This causes a broadening of the pulse spectrum that, for significantly high peak intensities, leads to the generation of a super continuum covering all of the visible spectrum. The pump and the super continuum beam is focused onto a second BBO crystal in a double pass configuration. Through difference frequency generation, an idler (and signal) beam is amplified through the crystal fullfilling the energy conservation condition $\hbar\omega_p - \hbar\omega_s = \hbar\omega_i$, where $\omega_p$, $\omega_i$ and $\omega_s$ are the pump, idler and signal frequency. The latter is the component in the spectrum of the supercontinuum that fullfills the phase matching condition $k_p - k_s = k_i$, where $k$ is the corresponding wavevector in the crystal. By changing the angle of the BBO crystal, the phase matching condition implies a change in the signal and idler frequencies. E.g. for a signal wavelength of 539 nm, the generated idler wavelength is 1550 nm. An idler output of approximately 300 $\mu$W corresponding to a pulse energy of $\sim$ 1.2 nJ at 1550 nm is typically generated.

## 3.2 Heterodyne measurement technique

The idler beam from the OPA, is used for characterisation of semiconductor optical devices. Unfortunately, there exist no detectors capable of resolving pulses on the order of $<$150 fs.[2] Thus, time resolved measurements of ultra short pulses, are based on detected signals integrated over multiple pulses. In order to resolve such fast changes of the electric field, a reference field is typically correlated with the pulse. This is often achieved by introducing a non-linear element exploiting second harmonic generation or by frequency shifting the two signals relative to each other. The former method is extensively used in basic tools for characterisation of ultra fast pulses, e.g. auto correlators[111] and frequency resolved optical gatings (FROGs) [112, 113]. In this work we shall use the method of frequency shifting the two signals. A detection technique denoted heterodyne detection. The word heterodyne is derived from the greek words *hetero* meaning different and *dyne* meaning power. The principles was first demonstrated for use in pump-probe measurements by E. Ippen and co-workers [85].

Most of the setup used in this thesis, was originally developed by P. Borri in the group of J. Hvam[114], and has been extensively used for gain dynamics

---

[2]Current state of the art streak cameras are quoted with a response time of $<$200 fs. Currently, the fastest semiconductor photo detectors typically have a response time of $\sim$ $30 - 40$ ps.

measurements on SOAs [72, 74, 114, 115, 116]. In the following we shall briefly describe the main principles of the heterodyne detection scheme. For a more detailed discussion of the technique we refer to [114, 117].

### 3.2.1 The heterodyne detection setup

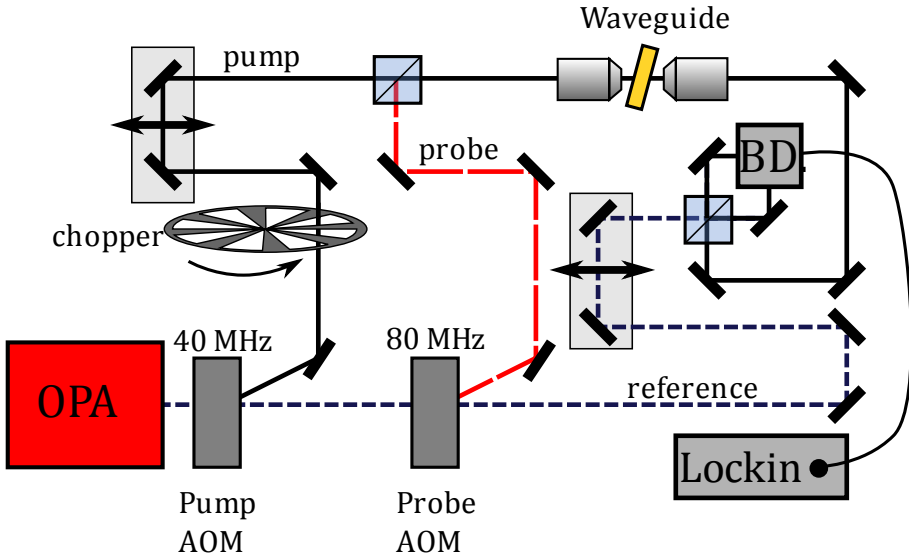The setup, following the OPA, is illustrated in figure 3.1 The idler beam



**Figure 3.1:** Experimental setup. Solid, dottet and dashed lines illustrate the pump, probe and reference beam paths, respectively. For the pump-probe measurements in chapter 6, a chopper is used for the pump beam.

from the OPA is injected into an acousto optical modulator (AOM)[3] driven at 40 MHz. The 1st order diffracted beam, is used for injecting into the waveguide device. For the pump-probe measurements, in chapter 6, this corresponds to the pump beam, and we shall in the following denote it accordingly although its role might be different. Similarly, we shall denote the AOM the pump AOM. The 0th order transmitted beam is used as the reference beam, traveling outside the device. The pump AOM is capable of diffracting 90% of the power to the pump beam, however, such high efficiency is associated with some group velocity dispersion. The resulting pulse broadening can be avoided using a compensating pulse shaper preceding the AOM [114]. For the experiments in this work, however, this method was not used and as a result, the

---

[3]Acouto Optical Modulator. A piezoelectric transducer generates at travelling wave through a crystal (typically fused silica), that produce a grating of the refractive index. The injected optical electric field, is scattered on the grating where the $n$th order diffracted beam is shifted by $n$ times the carrier frequency of the transducer.

pulse intensity FWHM is broadened to 180 fs. Flip mirrors in the reference and pump beam paths were set up that allow for alternative paths of the reference and pump beams. In this path, the pump beam goes through a spatial light modulator (SLM) using a liquid crystal array[118, 119] that enables broadening of the pump pulse as well as creating pulses in rapid succession [57]. For the work presented in this thesis however, the SLM was not used.

The pump pulse is attenuated by changing the amplitude of the RF signal for the AOM, or using a neutral density (ND) filter. Changing the fraction of power that goes into the pump beam using the AOM, implies a corresponding opposite change of power in the reference beam. Therefore, for measurements that require an absolute measurement of the transmission as a function of pump power, the ND filter was used for attenuation (see chapter 4). The pump beam goes through a delay line, that enables temporal overlap with the reference pulse at the detection site. Finally it is injected into and collected out of the waveguide, using AR coated aspheric lenses with a numerical aperture NA= 0.65 and focal length $f = 2.75$ mm.

For the pump-probe measurements, the reference is transmitted through another AOM, where the 1st order diffracted beam is shifted by 80 MHz and used as a probe. Since the probe needs to be weak, an AOM was chosen with a small diffraction efficiency ($\sim 20\%$) that on the other hand does not introduce significant pulse broadening. The reference beam goes through a delay line before recombining with the pump or probe on a non-polarizing beamsplitter. The delay line of the reference beam enables temporal overlap with the probe pulse.

### 3.2.2 Detection scheme

The pump (or probe) and reference pulse are combined on a beamsplitter as depicted in figure 3.1. The two output ports of the beamsplitter are balanced with respect to the reference beam using a variable ND filter. Writing the reference and pump (probe) field in terms of their slowly varying envelope, i.e. $E_r(t) = \mathcal{E}_r(t) \exp\left(\mathrm{i}(\omega_r t + \phi_r)\right)$ and $E_p(t) = \mathcal{E}_p(t) \exp\left(\mathrm{i}(\omega_p t + \phi_p)\right)$, the output fields $E_a$ and $E_b$ arriving at detector A and B are [110]:

$$\begin{pmatrix} E_a \\ E_b \end{pmatrix} = \frac{1}{\sqrt{2}} \begin{pmatrix} 1 & \mathrm{i} \\ \mathrm{i} & 1 \end{pmatrix} \cdot \begin{pmatrix} E_r \\ E_p \end{pmatrix} \tag{3.1}$$

$$= \frac{1}{\sqrt{2}} \begin{pmatrix} \mathcal{E}_r(t) \exp\left(\mathrm{i}(\omega_r t + \phi_r)\right) + \mathrm{i}\, \mathcal{E}_p(t) \exp\left(\mathrm{i}(\omega_p t + \phi_p)\right) \\ \mathrm{i}\, \mathcal{E}_r(t) \exp\left(\mathrm{i}(\omega_r t + \phi_r)\right) + \mathcal{E}_p(t) \exp\left(\mathrm{i}(\omega_p t + \phi_p)\right) \end{pmatrix}, \tag{3.2}$$

where we have ignored any possible acquired phases apart from the $\pi/2$ shift from the reflections. The resulting intensity measured by the detectors are

$$\begin{pmatrix} I_a \\ I_b \end{pmatrix} = \frac{c\varepsilon_0}{4} \begin{pmatrix} \mathcal{E}_p(t)^2 + \mathcal{E}_r(t)^2 - 2\mathcal{E}_p(t)\mathcal{E}_r(t)\sin\left(\phi_p - \phi_r + (\omega_p - \omega_r)t\right) \\ \mathcal{E}_p(t)^2 + \mathcal{E}_r(t)^2 + 2\mathcal{E}_p(t)\mathcal{E}_r(t)\sin\left(\phi_p - \phi_r + (\omega_p - \omega_r)t\right) \end{pmatrix} \tag{3.3}$$

where the last term in each of the components is the beat signal, between pump(probe) and reference. The common mode intensity noise fluctuation are

significantly reduced by subtracting the two signals, giving a balanced signal with only the beat signal remaining

$$I_a - I_b = -c\varepsilon_0 \mathcal{E}_p(t)\mathcal{E}_r(t)\sin\left(\phi_p - \phi_r + (\omega_p - \omega_r)t\right). \tag{3.4}$$

Since the spectrum of a laser pulse train consist of a series of sharp spectral lines separated by the repetition rate, $f_{rep}$, there exists a multitude of beat frequencies, cf. figure 3.2. Approximating the spectral lines with delta functions,
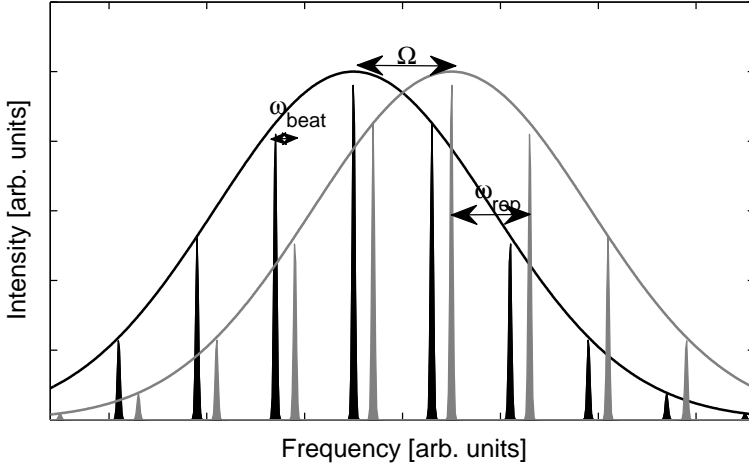


**Figure 3.2:** Illustration (not to scale) of the mixed reference and pump or probe spectrum. $\Omega$ denotes the RF frequency driving the AOM, $\omega_{rep}$ denotes the repetition rate of the RegA while $\omega_{beat}$ is the lowest beat frequency between the pump(probe) and reference spectrum, that is detected by the lock-in amplifier.

the spectrum of the two fields are given as:

$$S_r(\omega) = \sum_{-\infty}^{\infty} A_n \delta(\omega_n - \omega) = \sum_{-\infty}^{\infty} A_n \delta(\omega_0 - n\omega_{\rm rep} - \omega) \quad ; \quad n \in \mathbb{Z} \tag{3.5}$$

$$S_p(\omega) = \sum_{-\infty}^{\infty} A_m \delta(\omega_m - \omega) = \sum_{-\infty}^{\infty} A_m \delta(\omega_0 + \Omega - m\omega_{\rm rep} - \omega); \quad m \in \mathbb{Z}, \tag{3.6}$$

where $\Omega$ is the frequency driving the pump (probe) AOM, and $\omega_{\rm rep} = 2\pi f_{\rm rep}$. The beat frequencies between (3.5) and (3.6) are then

$$\Delta\omega_{nm} = (m - n)\omega_{\rm rep} - \Omega \equiv l\omega_{\rm rep} - \Omega \quad ; \quad l \in \mathbb{Z}. \tag{3.7}$$

For a repetition rate of 255 kHz and a driving frequency of the AOM of 40 MHz, the lowest beating frequency between the pump and reference field is 35 kHz for $l = 157$. The next lowest is 190 kHz. Since the beat signal is sent to a

lock-in amplifier with a detection range from 0-100 kHz, only the lowest beat frequency is detectable by the lock-in. The lock-in amplifier is referenced by down-mixing the sinusoidal RF frequency driving the AOM with a TTL[4] signal of the repetition rate fed by the RegA. Since the TTL signal contains all higher harmonics of the repetition rate, the mixed frequencies corresponds exactly to those in equation (3.7).

An important point of equation (3.4), is that the detected signal on the locking detects changes of the electrical field of the pump (probe), and *not* the intensity. Thus, doubling the input pump (probe) intensity leads to an increase in the detected signal by a factor $\sqrt{2}$, for pulse energies in the linear gain regime. This becomes important when measuring the pulse width as well as for pump-probe experiments measuring the gain dynamics.

---

[4]TTL is a square wave signal, where the lower voltage is typically 0 V and the highest voltage is between 1-10 V. The Fourier series of the square wave, is a sum of all harmonics of the carrier frequency.

# CHAPTER 4

# Pulse delay by gain saturation

In this chapter experimental pulse propagation measurements in quantum well waveguide are presented. The measurements examine the delay and advancement of ultra fast pulse with a duration of 180 fs, exploiting gain saturation effects. The type of devices are described together with the experimental procedure of the measurements. Sources of noise in the measurements are discussed and the taken precautions are presented. The experimental results are compared with a simple model and end with a discussion of possible physical effects that may lead to discrepancy between measurements and model.

## 4.1 Pulse delay of ultra fast pulses

Semiconductor optical amplifiers SOAs and EAs have been demonstrated to be efficient at delaying or advancing signal with a bandwidth of up to a few tens of GHz using CPO, cf. chapter 1. However, for signals in the THz regime ($< 1$ ps), CPO is no longer effective due to the carrier life time of $\sim$ns. Nevertheless, SOAs and EAs have been demonstrated for electrically controlled pulse delays and advancements of sub-picosecond pulses [54] using a different, although related [52], technique based on gain/absorption saturation effects. The basic origin of pulse delay and advancement in a saturated absorbing/amplifying medium are easily understood [51, 107]: The tail of the pulse experience a weaker absorption/amplification compared to the front of the pulse, due to the gradual bleaching of the medium, resulting in a pulse shaping towards negative/positive times, cf. chapter 2. Recently, the technique was improved by introducing dispersive elements on both sides of the SOA [56]. However, because it requires pulse compressors/stretchers, this technique is not yet feasible for achieving monolithically integrated devices that allow for controllable pulse delays.

In general, the major drawback of the absorption saturation technique is

that a large delay is associated with a large pulse absorption. On the other hand, pulse advancement is associated with pulse amplification, and one might naturally consider the results of combining such two materials. Balancing the absorption and gain in the two sections to achieve a net transmission of unity, one might naïvely think that the induced delay in the two section would cancel. In the following, we experimentally demonstrate the possibility for delaying ultrafast pulses in a monolithically integrated device with a transmission of unity, by cascading SOAs and EAs.

## 4.2 Device structure

The ridge waveguide devices investigated are based on a design originally developed for the National Technical Research Council project Semiconductor COmponentes for Optical signal Processing (SCOOP). A detailed analysis of the devices, with emphasis primarily on use as mode-locked lasers can be found in [120]. The material composition and processing method for the mode locked lasers, are similar for the SOA and EA devices[1]. A detailed discussion of the choice of material composition and processing techniques is beyond the scope of this work and we shall only briefly describe the basic structure of the devices used for the experiments.

The waveguide structures are based on an active material of compressively strained InGaAsP QWs, with a ground state transition near 1530 nm, embedded in a PIN structure with positively and negatively doped InP, see figure 4.1. The waveguides are single moded with a ridge width of 2 $\mu$m giving an average modal area of roughly $\sim 3$ $\mu m^2$. Furthermore, the waveguides are angled by $7°$ relative to the end facets, corresponding to a $21°$ external angle, to avoid back-reflections. To further minimise reflections, the facets are anti reflection coated using layers of TiOs and $SiO_2$ [120]. An example of the calculated field mode, on a logarithmic scale, is plotted in figure 4.2. The calculations were performed using the commercial software *Selene*. The confinement factor of a single QW is estimated to $\Gamma = 0.023$.

Two types of devices were investigated: One 500 $\mu$m long waveguide consisting of a single QW with a single contact (see figure 4.3a) that we shall refer to as the single sectioned device. The other device has 5 QWs with separately contacted sections of the waveguide allowing for individually applied voltages on separate parts of the waveguide, see fig. 4.3b. We shall denote this the cascaded device. Here, the first and last section (as experienced by the pulse) are forward biased rendering them amplifying (SOA), whereas the middle section is reverse biased to make it absorbing (EA). The samples were mounted on a copper heat sink cooled to $18°$ C by a Peltier element. Based on the measured photo current generated by the laser beam, we estimate an in coupling efficiency of 0.37.

---

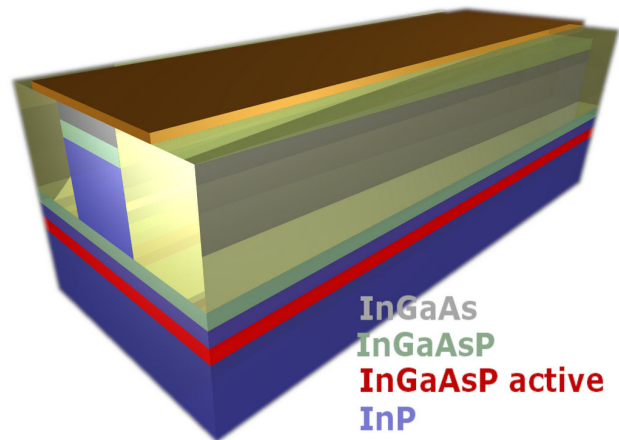[1]In fact, the same lithography mask is used for all three types of devices.

**Figure 4.1:** Illustration of the SOA/EA waveguide structure. The active material consists of compressively strained InGaAsP QWs in a PIN structure (from top to bottom). Gold contacts on top and bottom allow for applying a voltage across the active material. The width of the ridge waveguide is 2 $\mu$m. Material surrounding the ridge (colored light yellow) is a BCB polymer offering a low refractive index.
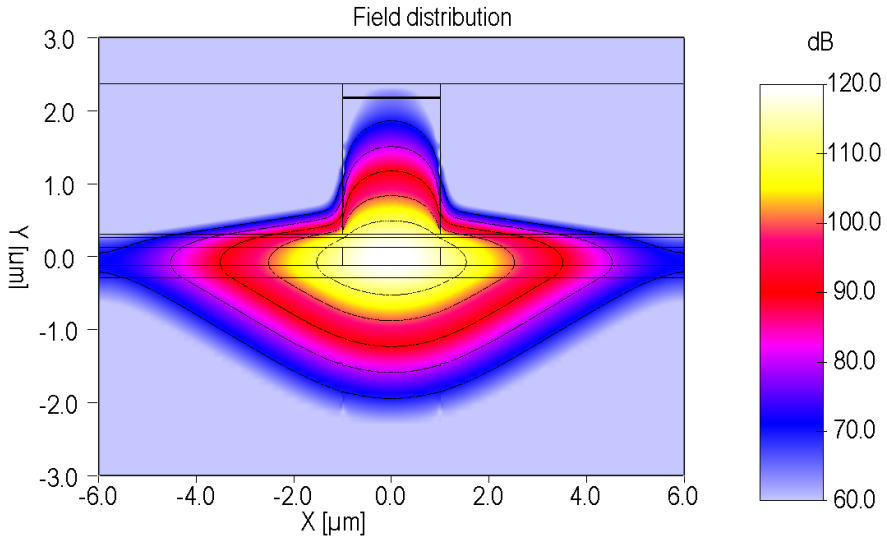
**Figure 4.2:** Transverse field distribution calculation using *Selene*. Note that the field distribution is plotted on a logarithmic scale. Dark straight lines illustrate the material compositions. The confinement factor of a single QW is found to be $\Gamma = 0.023$.
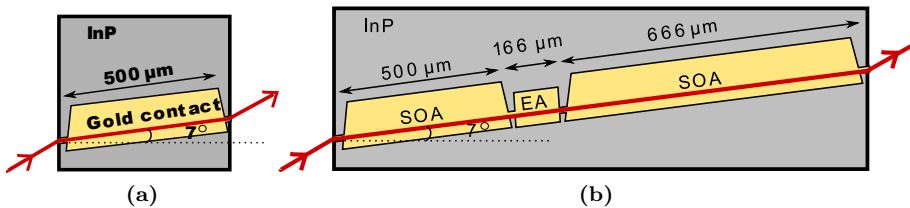


**Figure 4.3:** (a) Top view of the single contacted device. Waveguide length is 500 $\mu$m, with a active medium consisting of a single QW. (b) Top view of cascaded device consisting of a 500 $\mu$m amplifying, 166 $\mu$m absorbing and a 666 $\mu$m long amplifying section. Arrows indicate the propagation direction of the laser pulse.

## 4.3 Measurement procedure

Using the pump AOM (see section 3.2.1), the 1st order diffracted beam was injected into the waveguide, while the 0th order was used as the reference. As discussed in section 3.2.1, the injected pulse energy can be changed by either changing the power of the RF signal fed to the AOM, or alternatively simply using a variable ND filter. Since the former solution implies a corresponding but opposite change of the reference beam, the method of using an ND filter is used for attenuation. It was checked that the filter did not itself induce distortion of the pulse amplitude profile. Also the optical transit time of the filter was measured to be independent of the attenuation within an accuracy of 3 fs. The measurement setup is illustrated in figure 4.4
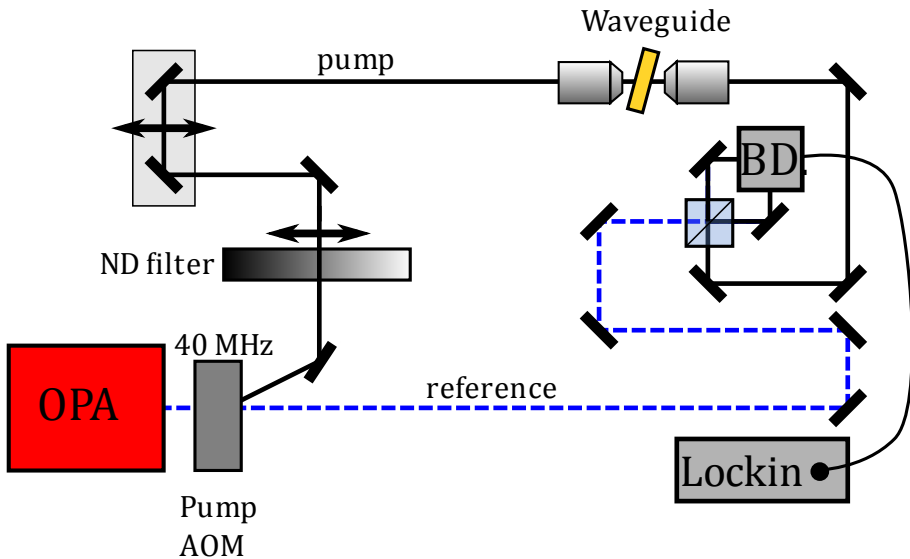


**Figure 4.4:** Experimental setup used for the delay measurements. The 1. order diffracted beam from the AOM is injected into the waveguide, using high NA aspherical lenses. The reference beam is directed outside the device. A lockin amplifier detects the signal from the balanced photodiode at a beat frequency between the two beams.

The heterodyne detection scheme, described in chaper 3.2.1, was used to perform cross-correlation measurements of the transmitted pulse with a reference pulse propagating outside the waveguide. A series of measurements, with fixed applied bias, were performed measuring the transmitted pulse envelope as a function of time by stepping the pump delay stage for various input pulse energies. In order to minimise influence of long term drifts, such as laser intensity fluctuation and temperature drift, a step size corresponding to 50 fs makes measuring each envelope fairly quick while maintaining an acceptable

resolution of the envelope. Each measurement is fitted with a Gaussian function from which both amplitude and delay are extracted. An example of this is seen in figure 4.5.
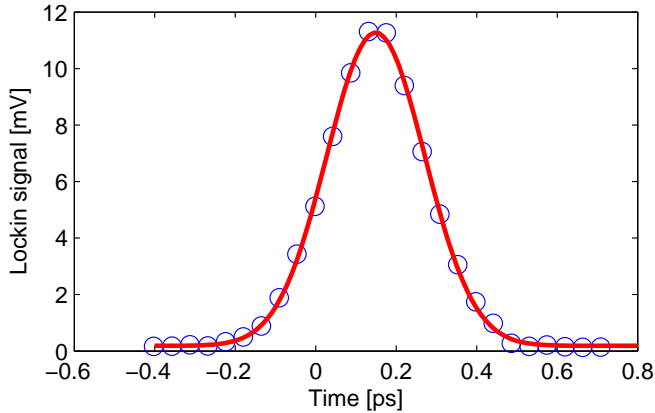


**Figure 4.5:** Example of a measure pulse envelope using the single sectioned device with a pulse energy of 2 pJ. The delay stage is translated in steps corresponding to 0.05 ps. Solid line is a Gaussian fit of the measured data.

Finally, the relative pulse delay, deduced from the Gaussian fit of each measurement series, is calibrated to zero at the lowest input pulse energy, since no shift is expected in the small signal regime where the medium does not saturate (see section 2.4).

### 4.3.1 Transmission calibration

Calibrating the pump pulse intensity relative to the lockin amplifier signal is difficult since the detected signal on the lock-in amplifier depends on the power of the reference beam, as well as the overlap of the reference and pump beam on the detectors. Also the amount of amplified spontaneous emission (ASE) from the component is seen to influence the measured signal on the lock-in amplifie. Instead, the small signal transmission is calibrated using two detectors measuring the input and output power respectively. The transmission based on the heterodyne measurements, is then deduced from the area of the squared envelopes[2] divided by the measured input pulse energy and scaled to correspond with the directly measured small signal transmission.

---

[2]recall from section 3.2.2, that the detected signal from the heterodyne setup scales as the square root of the output signal of the component. Hence, the area of squared envelope is proportional to the output pulse energy.

### 4.3.2 Influence of temperature drift

In order to make sure, that the variable ND filter did not itself introduce a delay that changes with the position of the filter, we performed a series of measurements changing the reference pulse energy using the ND filter. For each pulse energy, the pulse envelope was measured and fitted with a Gaussian function. The center of the Gaussian envelope and the "area" from integrating the envelope is seen plotted in figure 4.6a and 4.6b, respectively, as a function of the reference transmission through the ND filter. The arrow indicates the
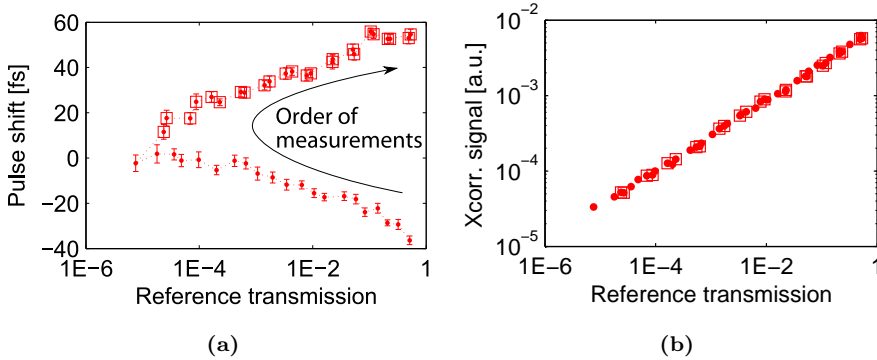


**Figure 4.6:** (a) Measured position in time of the center pulse envelope, as a function of transmission of the reference beam. The reference beam was attenuated using the same variable ND filter used for pulse delay measurements. (b) Corresponding "area" from integrating the Gaussian envelopes.

order in which the measurements were performed. Considering the delay in figure 4.6, clearly, a source of noise is seen to give rise to a significant drift of the measured delay. Had it been the ND filter causing the shift, the control measurement for increasing pulse energy (squares) would follow the measurements for decreasing pulse energy (dots). We note that the measurements were performed with roughly equidistant time intervals, where the full measurement series lasted approximate 1.5 hours. Such a long term drift is likely to arise from a drifting room temperature. The measurement were performed, with the pump beam transmitted through the waveguide device. The observed pulse shift could therefore emerge as a result of a gradual misalignment of the pump due to thermal expansion. In this case, the in-coupled pulse energy is slowly decreasing that leads to a different pulse shaping through the device. However, from figure 4.6b, it is clearly seen, that the transmitted signal remains approximately constant, since the measurements with increasing pulse energy (squares) overlap with the measurements with decreasing pulse energy (dots). From figure 4.6a, a drift of roughly 100 fs is observed corresponding to a change of propagation length of $\sim 30$ $\mu$m. To verify that temperature indeed was the key source of drift, we performed the same measurements as before, only without attenuating the reference beam an noting the time of each measured envelope.

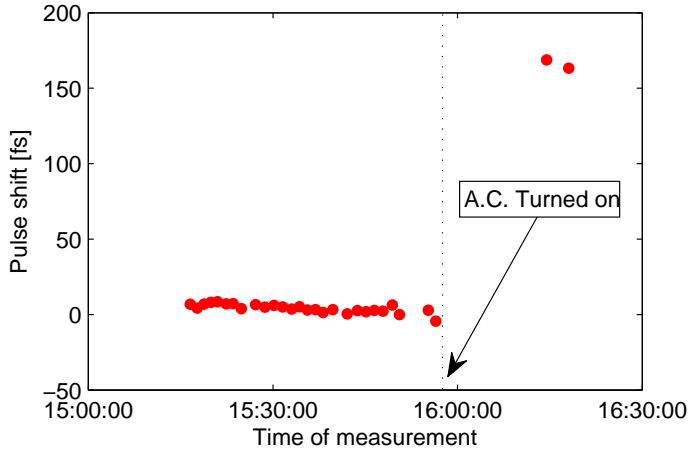The results are seen plotted in figure 4.7. Once again a slow drift is observed,



**Figure 4.7:** Repeatedly measured pulse delay as a function of the time of measurement. Dashed line indicate the time where the climate control was turned on.

until the time where the climate control was turned on indicated by a dashed line. Within few minutes, the pulse was shifted by 170 fs. Thus, for this type of measurement where delays of a few tens of fs are measured, control of the temperature is crutial. Since our climate control at the time simply was not capable of keeping a satisfactory constant temperature, we instead performed a reference measurement for every second measurement using a fixed input pulse energy. Noting down the clock of each measured envelope allows us to extract the reference delay at any given time by interpolating the measured reference delays as a function of the time of measurement. The interpolated reference delay is then subtracted from the corresponding delay measurement. In this way, any delay induced by temperature drift is separated out. An example of this is seen in figure 4.8, where the reference delay is seen to drift by about 50 fs during less than an hour. The red squares indicate the measured delay reference, and the red solid line is the interpolated curve. Blue circles indicated the inferred delay reference from all other measurements.

Due to the the temperature drift, the in-coupling factor between free space and the waveguide was also measured to degrade with time by approximately 0.17/hour. Thus, after each measurement series with a fixed bias level, the in-coupling was re-optimised.
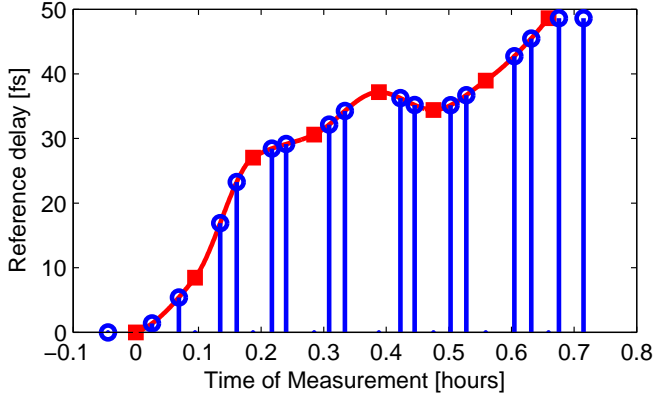
**Figure 4.8:** Example of delay reference points in a measurement series with fixed bias. Every third measurement was a reference measurement at a fixed input pulse energy, illustrated by squares. Solid line represents interpolation curve of the reference delay values. Bars represent the time of all other measurements, with circles indicating the inferred delay reference value.

## 4.4 Experimental results

### 4.4.1 Single sectioned waveguide

Figure 4.9 shows the measured pulse delay (bottom) and transmission (top) of the single sectioned device as a function of input pulse energy for four different applied bias levels. Considering the transmission (top), it is seen that the device is amplifying for bias levels corresponding to 5 mA and 20 mA and absorbing for bias level of 0 V and −1 V. This is in good agreement with a measured transparency current[3] of 3 mA. For the bias levels of −1 V and 0 V, where the device is absorbing, a clear sign of pulse delay is observed. This is in good agreement with the model derived in section 2.4 where pulses, entering a saturable absorbing medium, experience a stronger absorption of the front of the pulse compared to the tail of the pulse, thus shifting the pulse towards positive times. A maximum pulse delay of 90 fs was measured for a pulse energy near 1 pJ, however, it comes at the cost of 10 dB attenuation. As the pulse energy is further increased, bleaching of the absorption is expected during the very first part of the pulse which implies a reduction of the induced shift. For the measurements, however, we observe a pulse advancement at the highest input energies for all applied bias, in contrast to the expected. To signify this, the measured transmission is fitted using equation (2.56).

---

[3]The current at which the device has a net gain of 0 dB. The transparency current was measured from the generated photo current using a lock-in amplifier detecting at the laser repetition rate. At the transparency current, the photocurrent reach 0 mA since the absorption and stimulated emission rate are equal.
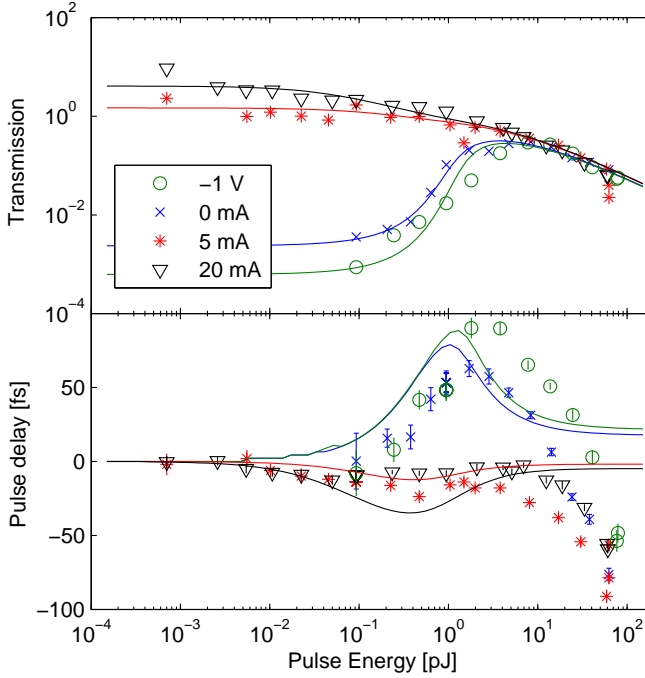
**Figure 4.9:** Measured pulse delay (top) and transmission (bottom) of the single sectioned device, for the applied bias levels corresponding to -1 V, 0 V, 5 mA and 20 mA. Solid lines represent fits of the transmission using equation (2.56).

Solid lines in figure 4.9 represents fits of the transmission. The saturation energy, $E_{sat}$, is allowed to vary between the four measurement series, as this phenomenological parameter is expected to vary with applied bias. The fitting parameters $\alpha_{int}$ and $\beta_2$, on the other hand, are fixed in all four measurement series. The values of the fitting parameters are presented in table 4.1. We note that the value of $\beta_2$ is found assuming an average mode volume of 2.8 $\mu$m$^2$ [4]. The simulated pulse shift is extracted in an analogous fashion to the experiment, i.e. by fitting the propagated pulse envelope with a Gaussian function. We emphasise that it is only the transmission that is fitted to the measurement. The delay is simply extracted from the corresponding simulated pulse envelope.

Comparing the measured transmission to theoretical values, good agreement

---

[4]The unit of $\beta_2$ as presented in equation (2.56) is the reciprocal of length times intensity [m/W]. Since we measure quantities related to the power in the experiement, the fitted TPA coefficient, $\beta_{\text{fit}}$, has the dimension of the reciprocal of length times power [m$^{-1}$W$^{-1}$]. Thus, to correspond with equation (2.56), the fitted value of $\beta_{\text{fit}}$ needs to be multiplied by the average mode area. I.e. $\beta_{\text{fit}} = A\beta_2$.

| Bias | $g_0$ [cm$^{-1}$] | $E_{\text{sat}}$ [pJ] |
|---|---|---|
| -1 V | -123 | 0.70 |
| 0 V | -116 | 0.72 |
| 5 mA | 11 | 0.77 |
| 20 mA | 34 | 0.77 |

**Table 4.1:** Used parameters for the fitted plots in figure 4.9 of the single sectioned device. WGL and TPA are fixed for all bias levels at $\alpha_{in} = 4.8$ cm$^{-1}$ and $\beta_2 = 45$ cm/GW assuming an average mode volume of 2.8 $\mu$m$^2$

is seen, while for the extracted delays clear deviations between theory and experiment are observed especially for the strongest pulse energies. We shall discuss the origin of this deviation in section 4.5.

### 4.4.2 Cascaded device

The single-sectioned device shows a maximum pulse delay of 90 fs corresponding to roughly half the pulse duration. The delay, however, comes at the cost of an attenuation of 10 dB. This drawback was successfully avoided with the cascaded device. These measurements were performed with a fixed applied bias corresponding to 17 A/mm$^2$ on the amplifying sections, being well above the transparency current.

Three series of measurements were performed for the bias levels, 0 V, $-1$ V and $-3$ V, applied to the middle section, all of which turn the section absorbing. The transmission and delay as a function of input pulse energy is plotted in figure 4.10, with solid lines representing fits of the transmission using equation (2.56). Considering the measured delay, the cascade device shows similar behavior as the single sectioned device, with a maximum delay of 70 fs. However, the maximum delay at -3 V is, as opposed to the single sectioned device, achieved with a transmission of unity.

Comparing the measured transmission with the fits, it seems that the model captures quite well the saturation properties of the pulse. However, regarding the delay (bottom), clear qualitative differences between measurements and model are observed. For the data shown in figure 4.10, $g_0^{(\text{SOA})}$, $\alpha$ and $\beta_2$ was fixed between all three data sets, whereas $g_0^{(\text{EA})}$ and the saturation energy of both SOA and EA sections where allowed to differ. Yet, fitting the three data sets can lead to somewhat dubious fit parameters, due to the few data points compared to the number of fitting parameters. Several different sets of fit parameters were experienced to give reasonable fits of the transmission, but common for them all was that the associated delay, did not correspond well with the measured values. Having said that, the fit parameters used in figure 4.10 are shown in table 4.2.

Considering the delay for large input energies, we observe, similarly to the single-sectioned device, that the pulse is advanced for all EA bias levels. This
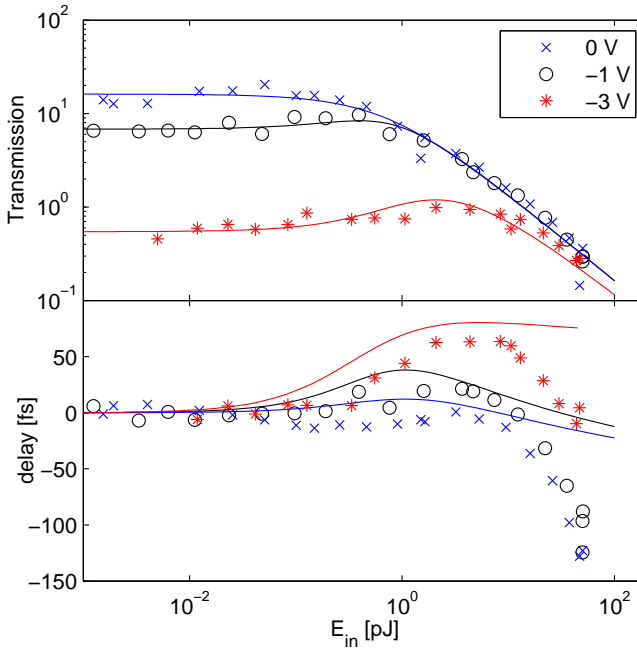
**Figure 4.10:** Measured transmission (top) and delay (bottom) of device II for various bias levels on the EA section. The bias current was 17 mA and 23 mA for the first and last SOA respectively. Solid lines represent fits of the transmission using equation (2.56), with fit parameters presented in table 4.2.

| Voltage | $g_0^{(EA)}$ [cm$^{-1}$] | $E_{sat}^{(EA)}$ [pJ] |
|---------|-------------------|-------------------|
| -3 V | $-3.3 \cdot 10^2$ | 2.3 |
| -1 V | $-2.1 \cdot 10^2$ | 1.8 |
| 0 V | $-1.5 \cdot 10^2$ | 3.4 |

**Table 4.2:** Used parameters for the fitted plots in figure 4.10. The remaining parameters were fixed at $g_0^{(SOA)} = 51$ cm$^{-1}$, $\alpha = 6.4$ cm$^{-1}$, $E_{sat}^{(SOA)} = 24$ pJ and $\beta_2 = 24$ cm/GW

effect was repeatedly observed for all measured devices, and is currently not fully understood. We shall discuss possible explanations for the observed effect in section 4.5.

Comparing the transmission of the three bias levels for the highest pulse energies, it is seen that they are of equal magnitude due to the dominating contribution of two photon absorption. The delay, on the other hand, differs by roughly 100 fs, thus, allowing for a temporal shift of more than 100 fs without significant changes in output power. However, at such high input energies, pulse distortion starts occuring. This is seen in figure 4.11 where the measured cross correlation intensity envelopes are plotted for a bias of −3 V giving the strongest pulse distortion. At the pulse energy giving the maximum



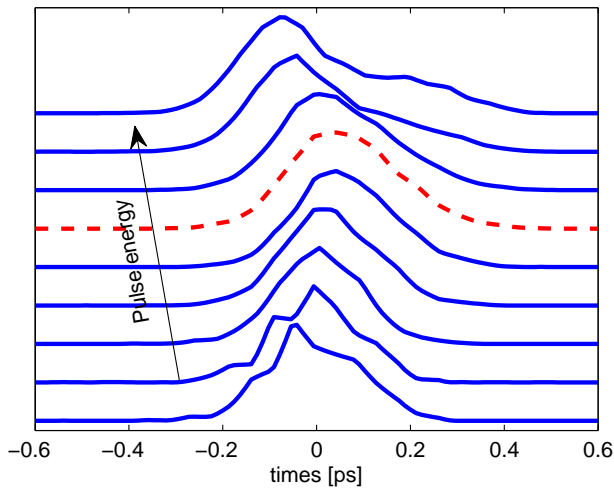**Figure 4.11:** Measured cross correlation intensity envelopes plotted in normalised units for input energies in the range 0.1- 100 pJ (distributed on a logarithmic scale) shifted vertically for clarity. The envelopes corresponds to the data plotted in figure 4.10 for a bias level of -3 V. The dashed envelope is for the pulse energy giving the largest delay.

delay (dashed envelope), however, no significant pulse distortion occurs.

# 4.5 Discussion

For the single sectioned-device, the simple gain saturation model was found to give results in qualitative agreement with the observed delay, except for high input pulse energies. Comparing the results of the cascaded device with the model was, to some extend, ambiguous due to the increased number of fit parameters. In principle, the observed pulse advancement at high energies could be explained as being due to a much larger saturation energy of the SOA section compared to the EA section. In this case, a delay is observed at low energies, and an advancement is observed at high energies, as seen for -1 V in figure 4.10. This, however, does not explain the observed pulse advancement of the single sectioned device in the absorbing regime in figure 4.9. The observed pulse advancement for all bias levels simply cannot be accounted for using (2.56), no matter the choice of fitting parameters. In the following we shall investigate and discuss possible effects that could explain the observed pulse advancement.

### 4.5.1 Polarisation rotation

It has earlier been shown [121], that intense laser fields propagating in an SOA may lead to a rotation of the polarisation. Since the group velocity of the TE and TM mode may differ appreciably, this could lead to a shift of the pulse, as the input pulse energy is increased. If the input pulse is not fully polarised in the TE plane, a residual TM component could be rotated with an output component that is detected in the heterodyne setup. To check if this was the cause of the observed pulse advancement we measured the transmission as a function of the input pulse energy and output polarisation. However, from the results, no significant rotation of the polarisation was detected at the highest input pulse energies. We therefore conclude that the observed pulse advancement at high input energies is not related to a rotation of the polarisation.

### 4.5.2 Pulse delay calculation including heating effects

It is clear from section 2.3 that the model, used for fitting, is a crude simplification, based on several questionable assumptions. E.g. CH as well as the redistribution of carriers near the resonance frequency was left out (see section 2.4). To check if a more rigourous model including the effects of carrier heating, could lead to the observed pulse advancement, we simulated the pulse propagation through a 500 $\mu$m medium similar to the single sectioned device. The calculation are based on solving (2.50) together with (2.47), (2.48) and (2.49). The used density of states, corresponds to a bulk medium, only changing the corresponding decay rates and confinement factor to correspond to QW structures. The resulting delay and transmission are plotted in figure 4.12 for three values of the small signal modal gain. The chosen values of $g_o$, $\alpha_{int}$ and $\beta_2$ are

chosen equal to those found by fitting the data of the single sectioned device in figure 4.9, for the bias levels of 0 V, 5 mA and 20 mA, respectively. Other
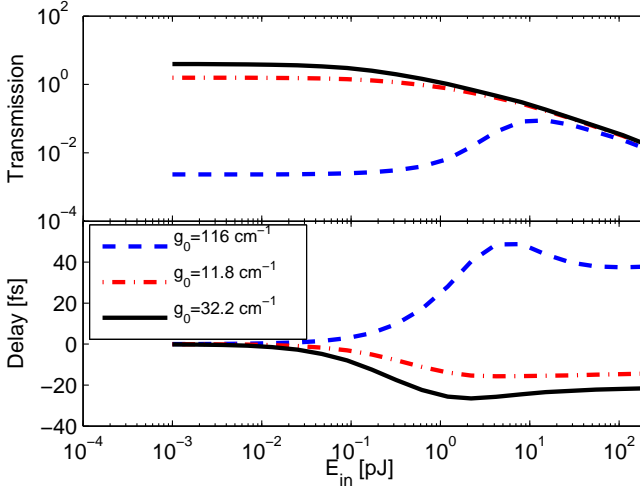


**Figure 4.12:** Simulated gain and delay as a function of injected pulse energy using a model including carrier heating effects. A 180 fs pulse was propagated through a 500 $\mu$m device by solving (2.50) together with (2.47), (2.48) and (2.49). Parameters corresponds to those extracted from fitting the data show in 4.9. Other parameters are presented in table t4.3.

parameters are presented in table 4.3.

From the figure, it is seen that the predicted maximum delay is reduced, compared to the results from the simplified model, cf. figure 4.9. This is also expected, since a finite SHB relaxation time reduces the saturating behaviour of the medium. However, besides minor corrections to the pulse delay we conclude that the inclusion of carrier heating effects does not result in any significant difference compared to the simplified model used for fitting. Notably, it does not give rise to the measured pulse speedup.

### 4.5.3 Estimation of the contribution from Kerr effects

As discussed in section 2.1, in deriving the rate equations we neglected the phase dynamics. In a medium exhibiting gain dispersion, this leads to a coupling between the instantaneous frequency and the gain experienced by the pulse. It has earlier been shown that this contribution becomes important for short pulses ($\sim$ 100 fs) and long waveguides even for weak pulses, where the carrier dynamics scales linearly with the pulse energy [63, 122]. This could lead to significantly different predictions of the pulse transmission at high input energies, compared to the simplified equation (2.56). In the following we shall discuss the possible influence from including refractive index nonlinearities in

| Parameter | Value |
|---|---|
| $\tau_2$ | 45 fs |
| $\tau_c^{(sc)}$, $t_v^{(sc)}$ | 100 fs |
| $\tau_c^{(h)}$ | 0.7 ps |
| $\tau_v^{(h)}$ | 0.25 ps |
| $\tau^{(s)}$ | 2 ns |
| $a_N$ | m$^3$/s |
| $\sigma_c$, $\sigma_c$ | $2 \cdot 10^{-21}$ m$^2$ |
| $m_c/m_e$ | 0.045 |
| $m_v/m_e$ | 0.37 |
| $E_g$ | 0.8 eV |
| $\beta_2$ | 45 cm/GW |
| $\alpha_2$ | 0.4 cm |
| $\Gamma$ | 0.023 |
| $\Gamma_2$ | 0.1 |

**Table 4.3:** Chosen parameters for the calculations presented in figure 4.12.

the background material.

For intense pulses the background material starts exhibiting refractive index nonlinearities that was neglected in equation 2.3. Higher order terms are included by expansion [5]:

$$\mathcal{P}(z,t) = \chi^{(1)}\mathcal{E}(z,t) + \chi^{(2)}\mathcal{E}(z,t)^2 + \chi^{(3)}\mathcal{E}(z,t)^3 + \dots, \tag{4.1}$$

Including a third order dependency, $\chi^{(3)}$, we get

$$\mathcal{P}(z,t) = \left(\varepsilon_0\chi_0 + \chi^{(3)}|\mathcal{E}(z,t)|^2\right)\mathcal{E}(z,t) \tag{4.2}$$

The refractive index is then found as

$$n = \sqrt{1+\chi} = \sqrt{1 + \chi_{bg} + \frac{1}{\varepsilon_0}\chi^{(3)}|\mathcal{E}(z,t)|^2} \tag{4.3}$$

$$\approx \sqrt{1+\chi_{bg}}\left(1 + \frac{\chi^{(3)}}{2\varepsilon_0(1+\chi_{bg})}|\mathcal{E}(z,t)|^2\right) \tag{4.4}$$

$$= n_{bg} + n_2\mathcal{I}(z,t) \tag{4.5}$$

where in the second equation it was assumed $\chi^{(3)}|\mathcal{E}(z,t)|^2/\varepsilon_0 \ll (1+\chi_{bg})$. Equation (4.5) describes the well known Kerr effect [5], giving an intensity dependent refractive index. Please note that the introduced Kerr nonlinearity arises from virtual transitions in the background material, and as such is considered instantaneous. This is in contrast to a intensity dependent refractive index associated with carrier absorption and recombination. I.e. a change of carriers, leads to a change of gain that, due to Kramers-Kronigs relation, leads to a change of refractive index. The intensity dependent refractive index leads

to a change of the optical phase of a pulsed laser field after a propagation length $z$ and is given by:

$$\delta\phi(z,t) \equiv \phi_2 - \phi_1 = \frac{\omega_0}{c} n_2 z\, \mathcal{I}(t), \tag{4.6}$$

where $\phi_1$ and $\phi_2$ is defined as the optical phase in a medium excluding and including Kerr nonlinearities, respectively. The change of phase leads to a change of the instantaneous frequency given by:

$$\delta\omega(z,t) = -\frac{\mathrm{d}\delta\phi(t)}{\mathrm{d}t} = -\frac{\omega_0}{c} n_2 z \frac{\mathrm{d}\mathcal{I}(t)}{\mathrm{d}t}, \tag{4.7}$$

where the sign of frequency was chosen such that $E \sim \exp\left(\mathrm{i}(kz - \omega t)\right)$. Assuming a frequency dependent gain, the change of frequency leads to a change of gain that by Taylor expansion is given as

$$\delta g(z,t) \approx \frac{\partial g}{\partial\omega}\Big|_{\omega_0} \delta\omega + \frac{1}{2}\frac{\partial^2 g}{\partial\omega^2}\Big|_{\omega_0} \delta\omega^2 + \dots \tag{4.8}$$

Exanding to first order we get

$$\delta g(z,t) = \frac{\partial g}{\partial\omega}\Big|_{\omega_0} \delta\omega \tag{4.9}$$

$$= -\frac{\partial g}{\partial\omega}\Big|_{\omega_0} \frac{\omega_0}{c} n_2 z \frac{\mathrm{d}\mathcal{I}(t)}{\mathrm{d}t}. \tag{4.10}$$

In the following, we shall consider two limiting cases:

In the limiting case where $t^{(sc)} \ll \tau_p$, the carrier distribution remains in a quasi Fermi distribution. For a Gaussian pulse, it is seen that $\mathrm{d}\mathcal{I}/\mathrm{d}t > 0$ for $t < 0$, while $\mathrm{d}\mathcal{I}/\mathrm{d}t < 0$ for $t > 0$ as is illustrated in figure 4.13. Depending on
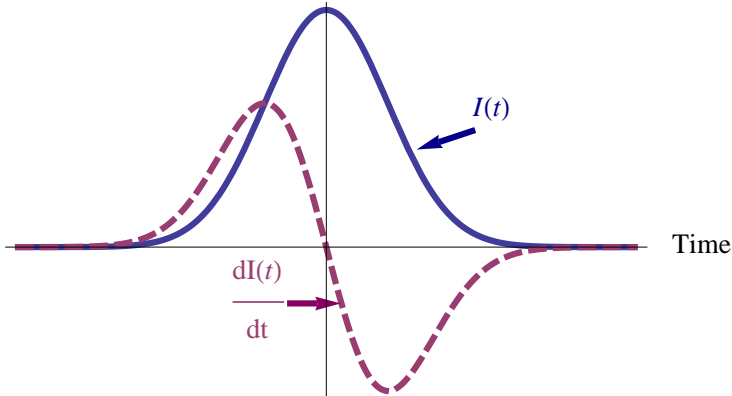


**Figure 4.13:** Illustration of a Gaussian envelope and it time derivative

the sign of $\partial_\omega g(\omega)$ and $n_2$, we find that a strong pulse leads to an increase of the gain at the front and a decrease of gain at tail of the pulse or vice versa.
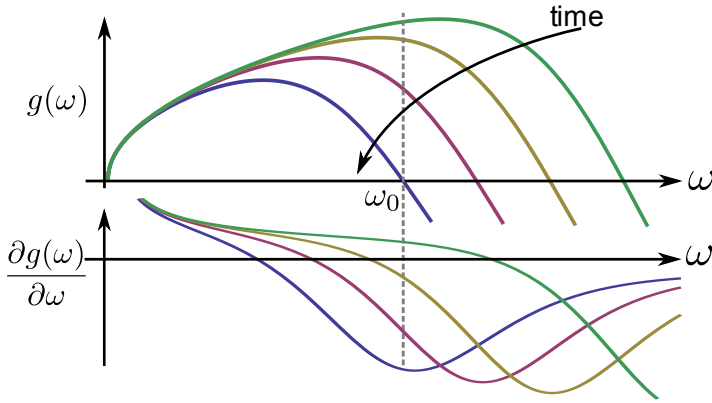
**Figure 4.14:** (top) Illustration of the gain spectra at various points in time upon excitation of a pulse for the special case $\tau^{(sc)} \ll \tau_p$. (bottom) The associate slope of the gain spectra.

E.g. if $n_2 < 0$ and $\partial_\omega n|_{\omega_0} < 0$ leads to a decrease of the gain at the front and an increase of the gain at the tail. The gain spectrum of bulk material is illustrated in figure 4.14 for a medium initially exhibiting gain. From the plotted slope (bottom), it is seen that initially $\partial_\omega g > 0$ at the laser frequency $\omega_0$, but as the gain is driven towards transparency, the slope turns negative. Thus, for a strongly saturated medium we can assume that $\partial_\omega g < 0$ and $g(\omega_0) \approx 0$, throughout the pulse duration. Thus, the propagation equation is found, using equation (4.10), as:

$$\frac{\partial \mathcal{I}(z, t')}{\partial z} = \delta g(z, t)\, \mathcal{I}(z, t') \tag{4.11}$$

$$= -\Gamma \frac{\partial g}{\partial \omega}\Big|_{\omega_0} \frac{\omega_0}{c} n_2 z \frac{\mathrm{d}\mathcal{I}(z, t')}{\mathrm{d}t'} \mathcal{I}(z, t') \tag{4.12}$$

The calculated output pulse and gain change $\delta g(t)$, after 500 $\mu$m propagation, is seen plotted in figure 4.15. Main parameters are $E_{in} = 10$ pJ, $\tau_p = 180$ fs, $\Gamma = 0.023$, $\partial_\omega g|_{\omega_0} = -1.5 \cdot 10^{-9}$ s/m and $n_2 = -3.2 \cdot 10^{-12}$ cm$^2$/W, where the latter was taken from [83]. From the gain change, it is seen that combination of a negative value of $\partial_\omega g|_{\omega_0}$ and $n_2$ leads to decreased gain at the front of the pulse and an increased gain at the tail of the pulse. This causes a self steepening towards positive times, i.e. a pulse delay.

In the limit $\tau^{(sc)} \gg \tau_p$ that was considered in section 2.4, a spectral hole is burned in the gain spectrum as is depicted in figure 4.16. Since the spectral hole has its minimum at $\omega_0$ we get $\partial_\omega g|_{\omega_0} = 0$, and the gain shift due to the Kerr effect is vanishing to first order in $\delta\omega$.

From this simple analysis, it is seen that in the limit where $t^{(sc)} \ll \tau_p$, a Kerr nonlinearity leads to a pulse delay, rather than the observed advancement, while in the limit where $t^{(sc)} \gg \tau_p$, no shift in gain is expected. We note, that the above arguments, hold for an absorbing medium as well. In this case a

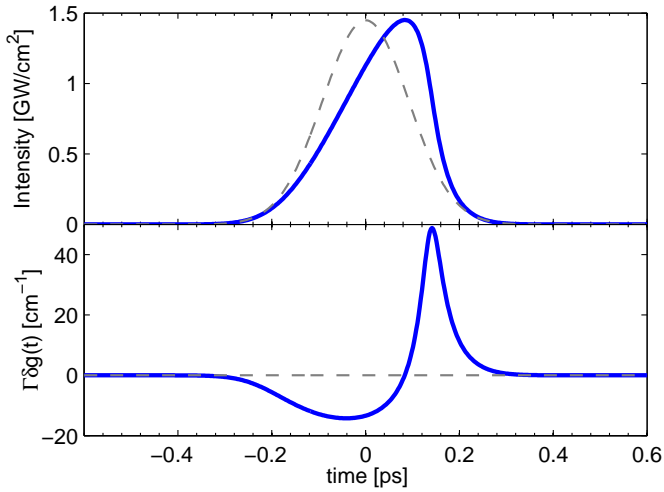**Figure 4.15:** (top) Calculated intensity envelope based on solving 4.12 propagating 500 $\mu$m. Dashed line illustrate initial pulse shape. (Bottom) Associated modal gain change $\Gamma\delta g(t)$.
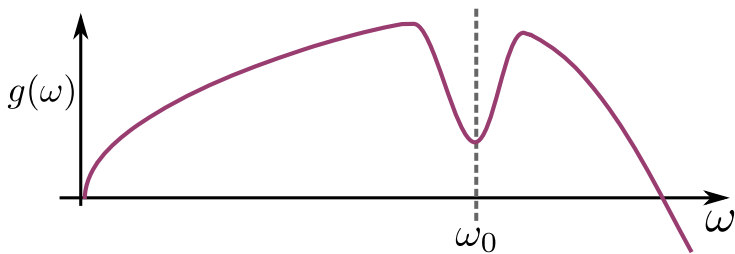


**Figure 4.16:** Illustration of the gain spectrum subject to SHB in the limiting case where $\tau^{(sc)} \gg \tau_p$. The gain dispersion is seen to be negligible near the carrier frequency $\omega_0$.

pulse delay is induced for $t^{(sc)} \ll \tau_p$. Also, in this analysis, we used a bulk medium as an example, however the arguments are applicable for a quantum well medium as well.

Unfortunately, the above analysis may be too simplified. In chapter 2, we only considered a linear expansion of $\Re(\chi_{bg}(\omega))$ around $\omega_0$ and neglected higher order terms that lead to GVD. As for the active material, only $\Im(\chi_a)$ (i.e. $g(\omega)$) was considered and was furthermore being treated independent of frequency. In this section, we expanded $g(\omega)$ to first order, while including an instantaneous Kerr nonlinearity from the interaction with the background material. Importantly, however, we did not consider refractive index non-linearities, associated with the carrier dynamics, e.g. by including linewidth enhancement factors $\alpha_N$, $\alpha_{SHB}$ and $\alpha_{CH}$ [123]. This would lead to a change of the instantaneous frequency that, in contrast to the above example, happens over time scales of the corresponding processes, e.g. stimulated emission and absorption, SHB and CH. Calculations like these were carried out in [63, 64, 122] by J. Mørk and A. Mecozzi with emphasis on pump-probe simulations. Although the calculations were based on carrier dynamics in the linear regime, the results showed clear deviation from the results using $\partial_\omega g(\omega_0) = 0$. The inclusion of nonlinear carrier dynamics were treated in [65, 66] with a 3. order expansion of $\chi(\omega)$ for both the background and active material, although using a somewhat simplified and generalised model for the carrier dynamics. In this case they show significant pulse shaping for pulse durations of 500 fs.

Based on the above mentioned work, we believe that in order to better describe the gain dynamics and pulse propagation at high input pulse energies, it is necessary to include gain dispersion in combination with refractive index nonlinearities .

## 4.6  Conclusion

In this chapter, experimental gain and delay measurements on waveguide structures using 180 fs laser pulses were presented. Two devices were used for measurements: One single sectioned device and one with cascaded amplifying and absorbing sections. For the single sectioned device, a total pulse delay of 90 fs were measured, although with a loss of 10 dB. This signal attenuation was effectively avoided in the cascaded device, showing a maximum delay of 70 fs with a transmission of unity.

The measurements were compared with a simplified propagation model derived in chapter 2. For the single sectioned device, reasonably good agreement was seen at modest input pulse energies. However, at high input energies, both devices showed a pulse advancement for all bias levels, which can not be accounted for, by the simple model. More advanced calculations based on the rate equation derived in chapter 2, including ultra fast carrier dynamics such as carrier heating, spectral hole burning and two photon absorption was compared with the measurement. Nonetheless, this did not give rise to the

observed pulse advancement. Finally, a simple inclusion of Kerr non-linearities in combination with gain dispersion was considered. This, however, was not able to account for the observed pulse advancement, but nevertheless pointed to the importance of including the phase dynamics.

# CHAPTER 5

# Slow light in quantum dots by EIT

In this chapter we propose a method of how to achieve electromagnetically induced transparency (EIT) in an inhomogeneously broadened quantum dot medium. We start by introducing some earlier work on EIT, followed by a brief introduction to the basic principles of EIT in an idealised atomic level system. The influence on dephasing, temperature and inhomogeneous broadening is assessed, where the latter leads to a comparison of three generic schemes. Finally, pulse propagation calculations for the three schemes are compared and analysed.

## 5.1 Motivation

Electromagnetically induced transparency (EIT) is a phenomenon, originally termed by Harris et al. [38], where an, otherwise opaque, medium is rendered transparent to a weak probe by applying a second strong coupling beam. The two light fields establish a coherence between the atomic states that leads to quantum interference between the excitation paths governing the optical response of the probe. The first experimental demonstration of EIT was carried out by Boller and co-workers in 1991 in Sr at room temperature [39]. Here, they showed that the transmission was changed from $\exp(-20)$ to $\exp(-1)$ when applying a strong coupling field. Later, Hau and co-workers [40] published their work, demonstrating a reduction of the speed of light to 17 m/s as a result of EIT. In this case, they used a Na Bose-Einstein condensate [124] in order to diminish pure dephasing as well as increase the atomic density. Shortly after, Kash and co-workers demonstrated light velocities of 90 m/s in a Rb gas at room temperature. Since then, EIT in atomic gasses has given rise to a major number of impressive experiments e.g. [41, 42, 43, 44, 45, 46] and [125] and references therein.

Self assembled QDs seem as an obvious choice for realising EIT in a solid material [60, 126]. I.e. they offer quantised energy levels, and as opposed to

atomic gasses, no efforts are spent on trapping the QDs. Furthermore, with the existing semiconductor processing facilities, self assembled QDs can be stacked, to increase the QD density, and imbedded in waveguide structures to increase the laser field overlap [60]. However, there are several issues that complicate the goal of QD-based EIT for achieving slow light: Firstly, dephasing rates in QDs are significantly higher than those found in atomic gasses. Depending on the temperature, the dephasing rate of the ground state transition ranges from being close to lifetime limited $\sim 1$ $\mu$eV at $\sim 5$ K to several meV at room temperature [72, 77, 78, 79, 127]. Secondly, the transitions in symmetrical quantum dots are subject to selection rules [62, 70] that only allow interband transitions between states with the same quantum number $\ell$, where $\ell$ is the angular momentum quantum number of the envelope functions. Finally, QDs suffer from inhomogeneous broadening IHB mainly caused by fluctuating QD sizes in the ensemble [128]. This leads to different transition energies of the individual QDs that for the total ensemble shows a Gaussian spectrum [78, 95, 129] which tends to destroy EIT features when probing an ensemble.

Several theoretical papers, have discussed the possible slowdown of light using EIT in QDs [59, 60, 126, 130, 131, 132, 133]. Apart from [130], only the $\Xi$-scheme (described later in this section) are considered, while only in [60, 126] is the IHB of QDs considered. In [126] a cavity design surrounding the QDs is proposed in order to enhance the slowdown effect and thereby reduce the number of necessary QDs. In [60], a scheme using a cascade of frequency components for the coupling field is suggested in order to reduce the degrading effects of IHB. However, for both proposals the experimental implementations are challenging.

So far, there have only been a few experimental demonstrations of EIT using self assembled QDs: Jundt et al. [48] and Xu et al [47] report on EIT features in the frequency domain of single QDs, whereas in the work of Marcinkevičius et al [134], EIT features are observed on an ensemble of QDs. In the experiment by Xu and co-workers, the transitions are based on a hyperfine splitting [135, 136, 137] of the ground state transition due to asymmetry of the QD potential; mainly caused by piezoelectricity [135]. Here, the degeneracy of the exciton ground states $|m_l = \pm 1\rangle$ is lifted with the new eigenstates $1/\sqrt{2}(|m_l = 1\rangle \pm |m_l = -1\rangle)$, that are coupled by linearly polarised light [135, 138]. The same scheme is used in the experiment by Marcinkevičius et al., where an ensemble of QDs were probed using a single broad band pulse that serves both as a pump and probe. Jundt et al exploits, the energy difference between exciton and biexciton states arising from Coulomb interactions. Common for all three papers [47, 48, 134] is that the scheme relies on a hyperfine splitting that requires the pump and probe to be linearly and perpendicularly polarised with both polarisation vectors in the plane of the QD plane of growth. As a result, at least one of the two fields (coupling or probe) are required to propagated perpendicular to the QD plane of growth. Letting the probe propagate perpendicular to the plane, offers the possibility of using a waveguide structure for the coupling field, thereby increasing the peak intensity. However, this limits the interaction length of the probe field to only a few layers of QDs. Instead, if the waveguide structure is used for the probe, the coupling

field must propagate perpendicular to the plane, while being expanded to cover the full length of the wave guide. The expanded mode area increases the power required for the coupling field. In all three papers, both the coupling and the probe field are travelling perpendicular to the sample. Thus, only the transmission spectrum were measured since the short interaction length only leads to very small pulse delays.

In this chapter we shall investigate the influence of IHB for EIT schemes based on schemes allowing for propagation of both pump and probe parallel to the QD plane (i.e. hyperfine splitting is not considered). In the following, the basic principles of establishing EIT is described for three commonly used generic schemes. For the purpose of illustration, we start by considering the simplest type of interaction that serves as a good approximation for atomic gases, i.e. we consider schemes in which one transition is forbidden, all dephasing rates are lifetime limited and IHB is neglected.

## 5.2 Principles of EIT in atomic systems

Consider a 3-level atomic system, interacting with a strong coupling laser field, and a weak probe laser field. Three generic schemes are considered, $\Xi$, V and $\Lambda$, depending on which state is chosen as the transit state[1], as illustrated in figure 5.1. The propagation of the probe field is found from the wave equation
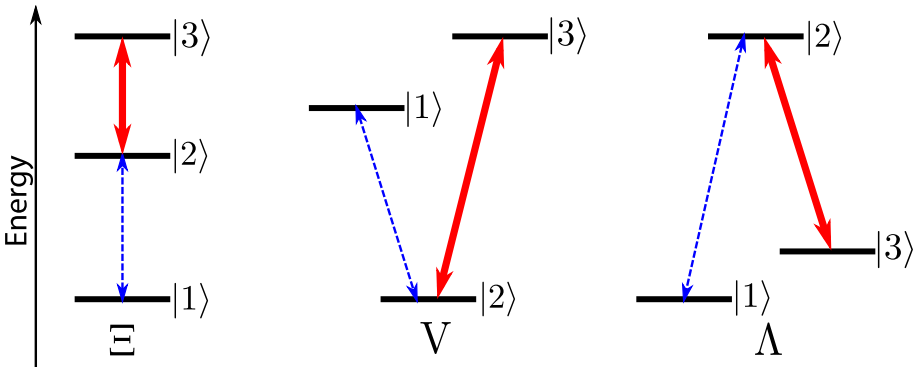


**Figure 5.1:** Three generic schemes $\Xi$, V and $\Lambda$. The states $|1\rangle$ and $|2\rangle$ are coupled by a weak probe field (dashed arrow) while $|2\rangle$ and $|3\rangle$ are coupled by a strong coupling field (solid arrow). The transition between $|1\rangle$ and $|3\rangle$ is assumed forbidden.

(2.10), by calculating the induced expectation value of the polarisation. As shown in section 2.2, this is done by calculating the density matrix of the system, analogous to the calculated density matrix of a two level in section

---

[1]the state that is a part of both the coupling and probe transition.

2.2, using the dipole approximation and the rotating wave approximation. The resulting density matrix equations of the three schemes, $\Xi$, V and $\Lambda$, are shown in appendix A. The expectation value of the polarisation is, by expansion of equation (2.29), given as:

$$P(t) = \varrho \left( \mu_{12} \tilde{\rho}_{21} \, \mathrm{e}^{-\,\mathrm{i}\,\omega_p} + \mu_{23} \tilde{\rho}_{32} \, \mathrm{e}^{-\,\mathrm{i}\,\omega_c} + \mathrm{c.c.} \right), \tag{5.1}$$

where $\omega_p$ and $\omega_c$ are the probe and coupling carrier frequency. The pump and probe field are assumed to be polarised along $z$ while $\mu_{12}$ and $\mu_{23}$ are the corresponding components along $z$. Since the probe field is weak, we can write the probe induced polarisation in terms of the linear susceptibility $\chi_p$. Assuming the medium to be isotropic implies that $\chi_p$ is a scalar. For a monochromatic probe and coupling fields, the polarisation is written as:

$$P(t) = P_p(t) + P_c(t) \equiv \mathcal{P}_p \, \mathrm{e}^{-\,\mathrm{i}\,\omega_p t} + \mathcal{P}_c \, \mathrm{e}^{-\,\mathrm{i}\,\omega_c t} + \mathrm{c.c.}$$
$$= \varepsilon_0 \chi_p(\omega_p) \mathcal{E}_p \, \mathrm{e}^{-\,\mathrm{i}\,\omega_p t} + \mathcal{P}_c \, \mathrm{e}^{-\,\mathrm{i}\,\omega_c t} + \mathrm{c.c.} \tag{5.2}$$

By inspection of equations (5.1) and (5.2), we find:

$$\chi_p(\omega_p) = \varrho \frac{\mu_{12}}{\varepsilon_0 \mathcal{E}_p} \tilde{\rho}_{21}(\omega_p) = \varrho \frac{\mu_{12}^2}{\varepsilon_0 \hbar} \frac{\tilde{\rho}_{21}(\omega_p)}{\Omega_p}. \tag{5.3}$$

Solving $\tilde{\rho}_{21}$ in the steady state allows us to write analytical expression for the electric susceptibility for continuos probe and coupling fields. Since $\Omega_p$ is assumed small, we may expand $\tilde{\rho}_{21}$ around $\Omega_p$ and neglect terms with $\Omega_p^2$ or higher orders[2] [125]. With this we get for the $\Xi$ and $\Lambda$-scheme:

$$\Xi: \quad \chi_p(\Delta_p, \Delta_c) = \varrho \frac{\mu_{12}^2}{\varepsilon_0 \hbar} \frac{2(\delta_+ - i\gamma_{13})}{4(\delta_+ - i\gamma_{13})(\Delta_p - i\gamma_{12}) - \Omega_c^2} \tag{5.4}$$

$$\Lambda: \quad \chi_p(\Delta_p, \Delta_c) = \varrho \frac{\mu_{12}^2}{\varepsilon_0 \hbar} \frac{2(\delta_- + i\gamma_{13})}{4(\delta_- + i\gamma_{13})(\Delta_p + i\gamma_{12}) - \Omega_c^2}, \tag{5.5}$$

where $\Delta_p$ and $\Delta_c$ are the probe and coupling laser detuning, e.g. $\Delta_p = \omega_p - \omega_{12}$ for the cascade scheme. Furthermore, the two photon detunings were introduced and defined as $\delta_\pm \equiv \Delta_p \pm \Delta_c$. The expression for the V-scheme is not quite as simple[3] as opposed to the other the schemes, and is given as:

$$\chi_p(\Delta_p, \Delta_c) = \varrho \frac{\mu_{12}^2}{\varepsilon_0 \hbar}$$
$$\frac{-2\zeta(\delta_- + i\gamma_{13}) - 2\delta_- \gamma_{23} \Gamma_1 + i\gamma_{23}(-2\gamma_{13}\Gamma_1 + \Gamma_3 \Gamma_{12}) + \Gamma_3 \Gamma_{12} \Delta_c}{(4(\delta_- + i\gamma_{13})(i\gamma_{12} + \Delta_p) - \Omega_c^2)(\zeta + \gamma_{23}(2\Gamma_{12} + \Gamma_{13})\Omega_c^2)} \tag{5.6}$$

where we define $\Gamma_1 = \Gamma_{12} - \Gamma_{13}$ and $\Gamma_3 = \Gamma_{23} + \Gamma_{13}$, i.e. the total population loss rate of state 1 and 3, respectively. Furthermore, we define $\zeta =$

---

[2]Since $\chi_p \propto \tilde{\rho}_{21}/\Omega_p$, a linear expansion of $\tilde{\rho}_{21}$ results in a susceptibility independent of the probe field.

[3]The origin of this complication, arrives from the fact, that $\rho_{33} - \rho_{22} \neq 0$ as opposed to the two other schemes. When solving the set of equations this causes a term of the type, $\Omega_p \Omega_c$ in the expression for $\rho_{13}$, that needs to be included in the expression of $\rho_{12}$.

$2\Gamma_{12}(\Delta_c^2 + \gamma_{13}^2)(\Gamma_{23} + \Gamma_{13})$. It is seen from equations (5.4), (5.5) and (5.6), that the susceptibility only depends on the homogeneous linewidths for the $\Xi$- and $\Lambda$-scheme, whereas for the V-scheme also the population decay rates are important. As we shall see later, this puts restrictions on the population decay rates in order to achieve EIT using the V-scheme.

As noted in section 2.1, the imaginary part of the susceptibility is related to the absorption coefficient, $\alpha$, and the real part is related to the refractive index, $n$, through the relations [9]:

$$\alpha = \frac{\omega_p}{cn_0}\chi'' \quad \text{and} \quad n = \Re(\sqrt{1+\chi}). \tag{5.7}$$

In the following, examples of the calculated $\chi''$ and $\chi'$ are presented and loosely referred to as the absorption and refractive index having the relations in equation (5.7) in mind.

Figure 5.2 shows the calculated real and imaginary part of $\tilde{\rho}_{21}$ normalized by $\Omega_p$ as a function of the probe detuning for all three schemes. The calculations were performed by solving the steady state of the density matrix rate equations derived in appendix A. Population decay parameters are $\Gamma_{23}/\Gamma_{12} = 1$,
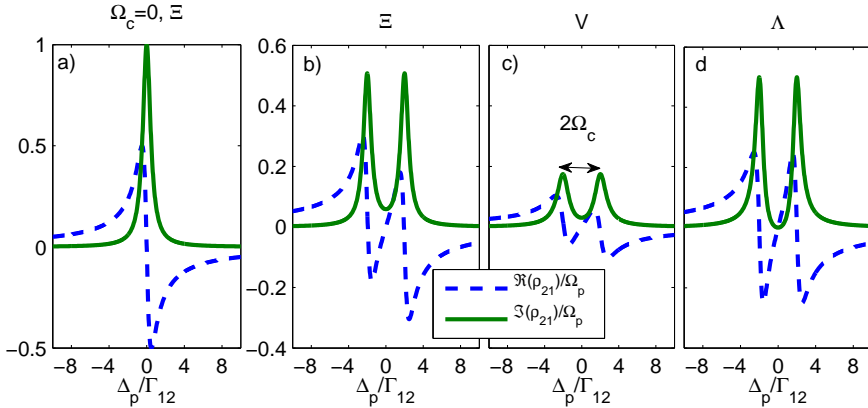


**Figure 5.2:** Plot of the real (dashed) and absolute imaginary (solid) part of $\tilde{\rho}_{21}$ as a function of the probe detuning $\Delta_p$ for the $\Xi$ (a,b), V (c), and $\Lambda$ (d) scheme. An example of $\Omega_c = 0$ is plotted in (a) for the $\Xi$ scheme. Parameters are $\Gamma_{23}/\Gamma_{12} = 1$, $\Gamma_{13}/\Gamma_{12} = 0$, $\Omega_c/\Gamma_{12} = 2$. Dephasing rates are assumed population lifetime limited.

$\Gamma_{13}/\Gamma_{12} = 0$ where $\Gamma_{ij}$ is the population relaxation rate between $|i\rangle$ and $|j\rangle$. The coupling Rabi frequency was chosen as $\Omega_c/\Gamma_{12} = 2$. The dephasing rates $\gamma_{ij}$ were assumed population lifetime limited, i.e. $\gamma_{12}^{(deph)} = \gamma_{13}^{(deph)} = \gamma_{23}^{(deph)} = 0$. For the case of a vanishing coupling field (figure 5.2(a)), the probe absorption shows the characteristic Lorentzian absorption curve together with anomalous dispersion near resonance. With the presence of a strong coupling field, the absorption is split into two resonances, with minimal absorption near $\Delta_p = 0$.

The dispersion has turned to normal dispersion, i.e. with positive slope near $\Delta_p = 0$. In this case, the group velocity of the light is reduced according to equation 1.29. The effect can be interpreted as arising from the coupling laser, that turns the eigenstates from being the bare states $|2\rangle$ and $|3\rangle$ to the dressed states [4] given by $|+\rangle = (|2\rangle + |3\rangle)/\sqrt{2}$ and $|-\rangle = (|2\rangle - |3\rangle)/\sqrt{2}$ with eigenvalues $\pm\Omega_c$, when $\Delta_c = 0$ and $\Omega_c \gg \Omega_p$. This shows as two resonances on the probe transition shifted by $\pm\hbar\Omega_p$. This is illustrated for the three schemes in figure 5.3(top). The contribution to the linear susceptibility from the two resonances
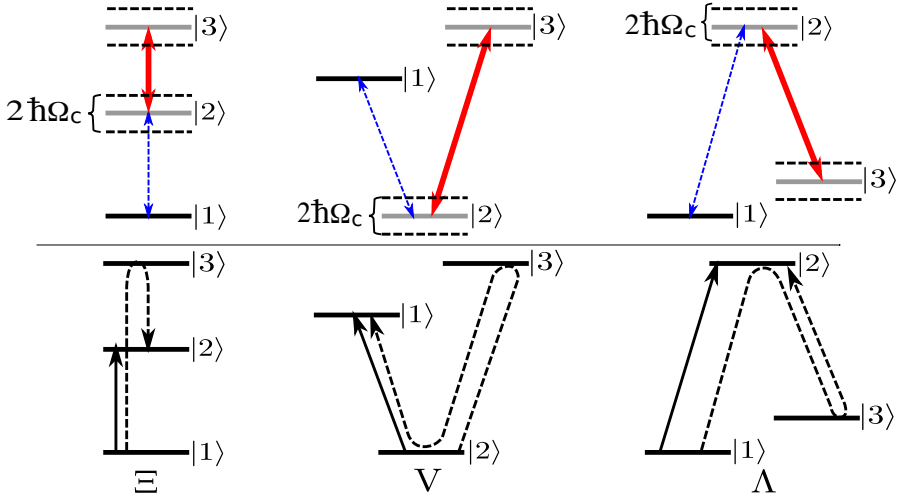


**Figure 5.3:** Illustration of the two equivalent interpretations of EIT. Upper diagrams shows the dressed states picture. Dashed lines illustrates the energy splitting relative to the bare state energy. Lower diagrams shows the interference of absorption paths interpretation. Solid and dashed arrows indicate the single and two photon absorption path, respectively. For the two photon path only the lowest order contribution is shown. I.e. contribution from $|1\rangle \rightarrow |2\rangle (\rightarrow |3\rangle \rightarrow |2\rangle)(\rightarrow |3\rangle \rightarrow |2\rangle)(\rightarrow |3\rangle \rightarrow |2\rangle) \ldots$ are left out

are equal but with opposite sign, and as a result the absorption vanishes [9, 125]. An alternative and equivalent interpretation, that we shall use, considers only the bare states where transparency arises from destructive interference between two types of absorption paths connecting $|1\rangle$ and $|2\rangle$, illustrated in figure 5.3. For the $\Lambda$ scheme, this correspond to the path $|1\rangle \rightarrow |2\rangle$ that we shall refer to as the single-photon pathway. The other type of path is the sum of all transitions of the type $|1\rangle \rightarrow |2\rangle (\rightarrow |3\rangle \rightarrow |2\rangle)(\rightarrow |3\rangle \rightarrow |2\rangle)(\rightarrow |3\rangle \rightarrow |2\rangle) \ldots$ that we shall refer to as the two-photon pathway. The two types of transitions are illustrated in figure 5.3 where only the fist term of the two-photon transition is illustrated.

---

[4]In the case of a vanishing electric field, the eigenstates of the system are those of bare atomic hamiltonian, denoted the *bare* states. In the case of a strong field, the eigenstate are found from the full hamiltonian including the contribution from the electric field. In this case, the eigenstates are denoted the *dressed* states.

Since the coupling field is strong compared to the probe field, the transition amplitudes of the single and two-photon transitions are equal in magnitude but with opposite sign, and as a result the probe absorption vanishes [125].

Comparing figure 5.2 b), c) and d), it is seen, that only for the $\Lambda$-scheme, does the absorption completely vanish. This comes from fact, that EIT arises from the coherence between the two terminal states $|1\rangle$ and $|3\rangle$. Hence, for non-vanishing $\gamma_{13}$, complete transparency is no longer possible. This is also confirmed from the analytical expression of the susceptibility in equations (5.4) and (5.5). In the case of population lifetime limited dephasing and no population decay between $|1\rangle$ and $|3\rangle$, we have $\gamma_{13} = 0$ for the $\Lambda$-scheme, while for the V- and $\Xi$-scheme we have $\gamma_{12} = \frac{1}{2}(\Gamma_{12} + \Gamma_{23})$ and $\gamma_{12} = \frac{1}{2}\Gamma_{23}$. Thus, only the $\Lambda$ scheme provide true EIT, and is in this sense also the preferred choice for achieving slow light. For the same reason, the $\Lambda$-scheme is the scheme commonly found in textbook examples. As we shall see in the following section, the dephasing rates and population decay rates between the three quantised levels can be very different in a QD due to selection rules and phonon coupling, and as such, the same conclusion does not hold. Furthermore, inhomogeneous broadening turns out to be the main problem, for achieving EIT in a QD medium.

Returning to the idealised atomic system, it is important to note that EIT is a quantum interference effect and not simply an effect of a reduced absorption due to AC Stark splitting [39]. This is illustrated in figure 5.4, where the real and imaginary part of $\tilde{\rho}_{12}$ in the $\Lambda$-scheme is plotted for $\Omega_c < \Gamma_{12}$. In this
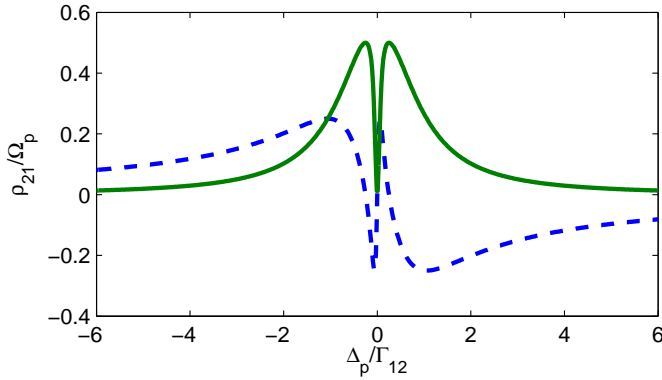


**Figure 5.4:** Calculated real (dashed) and imaginary (solid) part of $\tilde{\rho}_{21}$ normalized by $\Omega_p$ in the case of a very small coupling strength $\Omega_c = 0.5\Gamma_{12}$.

case, the absorption is still vanishing at $\Delta_p = 0$, however, the transparency windows is very narrow. This is associated with a rapid change of the real part of $\tilde{\rho}_{21}$, that leads to a very slow group velocity of the probe within a narrow bandwidth. In reality, however, $\gamma_{13} > 0$, and it therefore requires a minimum coupling strength for EIT to be observable. Nevertheless, close to negligible dephasing, $\gamma_{13}$, between state $|1\rangle$ and $|3\rangle$ can be realised in an atomic $\Lambda$-scheme,

by using a metastable state for $|3\rangle$. While for the other two schemes, dephasing between $|1\rangle$ and $|3\rangle$ is inevitable due to a finite population decay from $|1\rangle$ and $|3\rangle$. In figure 5.5, the absorption spectrum in terms of $\Im(\tilde{\rho}_{21})/\Omega_p$ is shown for the $\Lambda$-scheme for increasing $\gamma_{13}$. From the figure it is clearly seen, that EIT
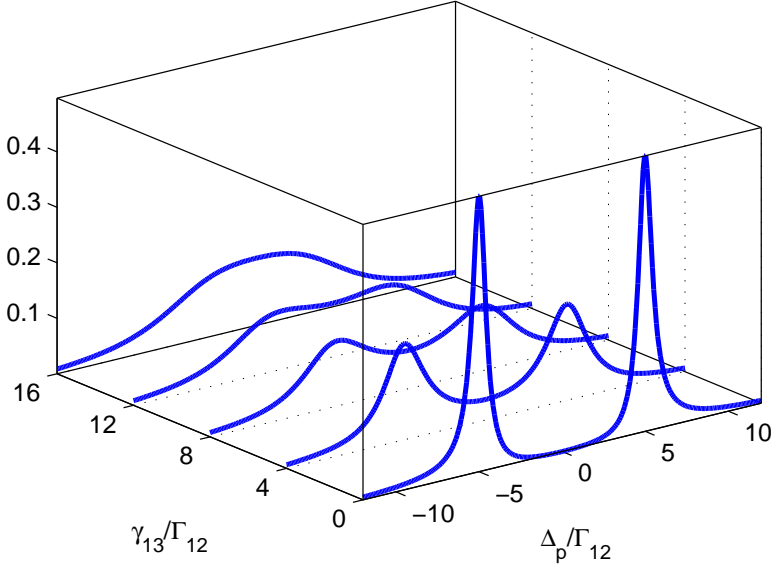


**Figure 5.5:** Calculated absorption spectrum, $\Im(\tilde{\rho}_{21})/\Omega_p$, as a function of $\gamma_{13}$ for the $\Lambda$-scheme. Other parameters equal to those in figure 5.2.

depends critically on the coherence between $|1\rangle$ and $|3\rangle$.

For a finite dephasing rate, $\gamma_{13}$, the features of EIT are re-established by increasing $\Omega_c$ to fullfill the condition $|\Omega_c|^2 \gg \gamma_{12}\gamma_{13}$ [125]. While increasing the coupling intensity leads to a decreasing absorption, it also has an impact on the slowdown factor due to the Kramers-Kronig relation. In figure 5.6, $\Re(\rho_{12})$ is seen plotted as a function of probe detuning, $\Delta_p$ for increasing values of $\Omega_c$ using the $\Lambda$-scheme. Parameters are chosen equal to those used in figure 5.2, except $\gamma_{13} = 0.4\Gamma_{12}$. The chosen coupling strengths are $\Omega_c/\Gamma_{12} = \{0, 1/2, 1, 2, 5\}$ shifted vertically for clarity. From the figure it is seen, that by increasing the coupling strength, the dispersion near $\Delta_p = 0$ goes from being anomalous to normal dispersion with a small positive slope. Increasing the coupling strength further, initially increases the slope near $\Delta_p$ but as the separation between the two resonances becomes larger, the slope starts decreasing. Recalling that the group index is related to the slope as $n_g = n_0 + \omega_p\partial(\sqrt{1 + \chi_p})/\partial\omega|_{\omega=\omega_p}$, it is seen that an optimum coupling strength exists where the group index is maximised. Thus, in a medium with significant dephasing between the terminal states, it is possible to decrease the absorption simply by increasing the coupling Rabi frequency, however, this decreases the possible slowdown effect.
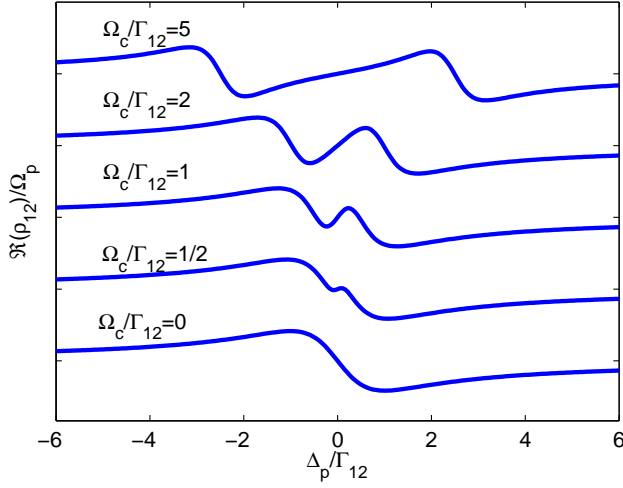
**Figure 5.6:** Dispersion relation, $\Re(\tilde{\rho}_{21})$, as a function of probe detuning, for various coupling field strengths. Other parameters are as in figure 5.2, exept $\gamma_{13} = 0.4\Gamma_{12}$.

IHB implies that different atoms (or quantum dots) experience different laser detunings. It is therefore instructive to examine the refractive index and absorption as function of both probe and coupling detuning. An example is plotted in figure 5.7. Restricting our attention to the absorption spectra (bottom), it is seen, that at $\Delta_c = 0$, the absorption is split symmetrically around $\Delta_p = 0$. However, for $|\Delta_c| > 0$, the two absorption peaks are split asymmetrically around $\Delta_p = 0$ both in terms of frequency as well as amplitude. The strongest peak is asymptotic to $\Delta_p = 0$ while the weaker peak is asymptotic to the condition

$$\Delta_p \pm \Delta_c = 0, \tag{5.8}$$

illustrated with a dashed white line, where the sum is for the $\Xi$-scheme while the difference is for the V- and $\Lambda$-scheme. We denote this the two-photon resonance. It can be shown[125] that the absorption is a local minimum close to this condition. For the $\Lambda$-schemes this implies complete transparency along the dashed white line. For large coupling detunings, $\Delta_c \gg 0$, the strong absorption is interpreted as arising from the single photon pathway, $|1\rangle \rightarrow |2\rangle$, while the weak absorption peak, asymptotic to the two-photon resonance, arise from the two-photon pathway. See figure 5.3. We denote these the primary and secondary resonance, labelled by I and II in figure 5.7. From the absorption plot of the V-scheme (middle, bottom), it is noted, that the secondary resonance quickly vanishes. This is due to the fact, that only in the V-scheme does the coupling field drive electrons on the coupling transition. Thus, for a coupling field far off resonance, electrons are never exited from $|2\rangle$ to $|3\rangle$ (see figure 5.3). Hence, only the single photon absorption path contributes to the probe
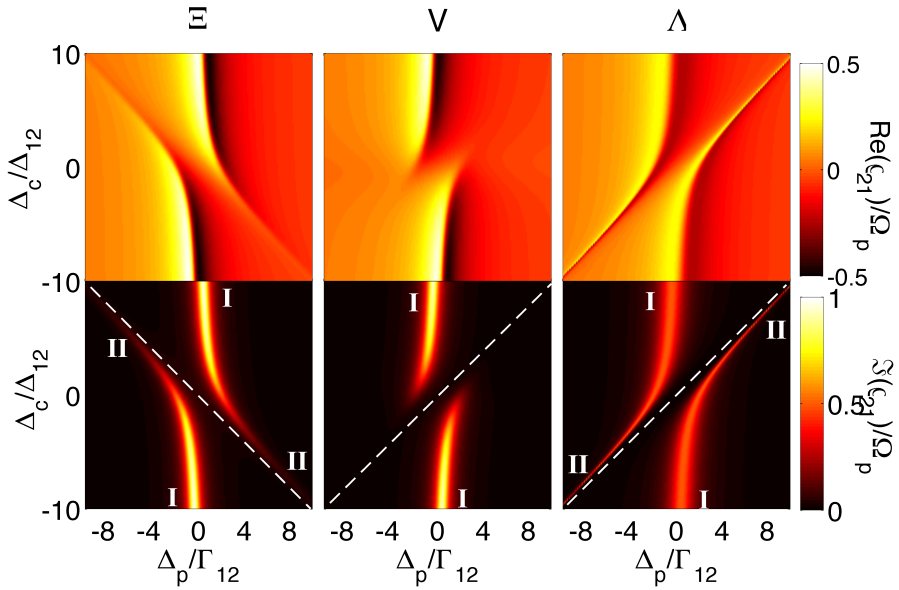
**Figure 5.7:** Real (top) and imaginary (bottom) part of $\tilde{\rho}_{21}$ normalised by $\Omega_p$ as a function of the normalised probe detuning, $\Delta_p/\Omega_p$, and coupling detuning, $\Delta_c/\Omega_c$, for the three schemes $\Xi$ (left), V (middle) and $\Lambda$ (right). Dashed white lines indicate the two-photon resonance. Primary and secondary are labelled by I and II, respectively.

absorption spectrum.

## 5.3 EIT in a quantum dot medium

Based on section section 5.2, we are now fully equipped to calculate the absorption and group index in a QD medium subject to EIT.

The three schemes $\Xi$, V and $\Lambda$ are considered in a quantum dot confinement potential as seen in figure 5.8. Please note, for ease of notation, we shall use a



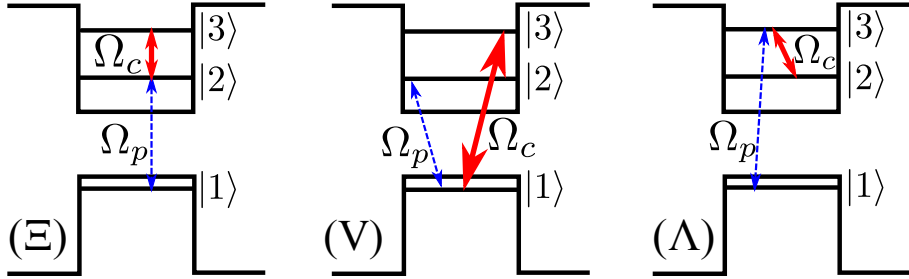**Figure 5.8:** $\Xi$- (left), V- (right) and $\Lambda$- (right) in a quantum dot confinement potential. Dashed and solid arrow indicate the probe and coupling transition, respectively. Note the different labelling compared to figure 5.1.

different labelling of the states (cf. figure 5.1). We note, that in a symmetric[5] potential, the transition $|1\rangle \leftrightarrow |3\rangle$ is forbidden due to the orthorgonality of the wavefunctions [62, 70]. Thus, in order to exploit the V- and $\Lambda$-scheme, one needs to break the symmetry of the QD potential. This can be achieved, e.g. by applying an electric DC field across the potential. In reality, however, bandmixing [62] and anisotropic strain effects, relax these selection rules, thereby allowing for a finite coupling between the otherwise forbidden transitions [101], however, with a somewhat weaker oscillator strength. The electric susceptibility is calculated from equation (5.4) by setting $\rho = \Gamma/V$ where $\Gamma$ is the confinement factor and $V$ is the volume of a single dot. The associated refractive index is found as[126]

$$n^2 = \epsilon_{bg} + \chi_p \tag{5.9}$$

where $\varepsilon_{bg}$ is the background electric permitivity.

---

[5]symmetrical in one, two or all three dimensions

### 5.3.1 Neglecting inhomogeneous broadening

We start by disregarding IHB. Thus the QD medium is treated similar to the atomic system, except, the dephasing and population decay rates are changed to realistic values. I.e. many-body interactions such as Coulomb interactions [130, 133] are neglected. Furthermore, all calculations are based on monochromatic laser fields, and as such, we shall not consider propagation effects such as GVD [59].

An example of the calculated group index of the $\Xi$-scheme for various homogeneous linewidths $\gamma_{12}$, is seen plotted in figure 5.9. The chosen ground transition linewidths correspond to those reported in [74, 77], while we tentatively set $\gamma_{23} = \gamma_{12} = \gamma_{13}$. The chosen parameters are presented in table 5.1.
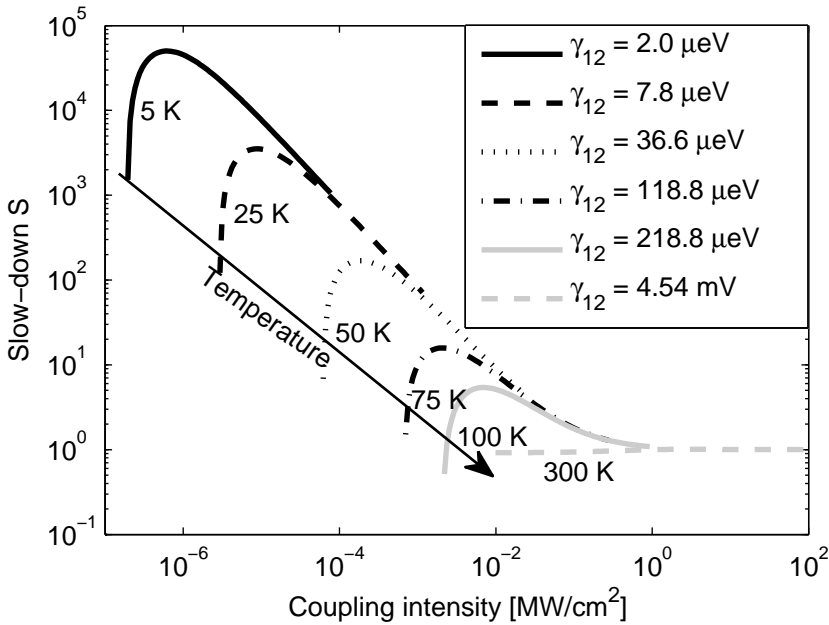


**Figure 5.9:** Calculated slowdown for the $\Xi$-scheme as a function of coupling intensity for various ground state transition linewidths, $\gamma_{12}$, based on measurements from[74, 77]. Furthermore $\gamma_{23} = \gamma_{12} = \gamma_{13}$.

As seen from figure 5.9, the dephasing rates, and thereby the temperature, drastically influences the possible slowdown effect. Especially at room temperature is the slowdown effect seen to completely vanish. Thus, for practical applications, one inevitably needs significant cooling of the QD sample. At lower temperature, an optimal coupling exists where a maximum slowdown factor is achieved. At this point, increasing the coupling field further, increases the Rabi splitting resulting in a decreasing slope of the refractive index.

| Parameter | $|1\rangle \leftrightarrow |2\rangle$ | $|1\rangle \leftrightarrow |3\rangle$ | $|2\rangle \leftrightarrow |3\rangle$ |
|:---:|:---:|:---:|:---:|
| $\hbar\omega_{ij}$ | 0.999 eV[95] | 1.06 eV[95] | 61 meV[95] |
| $\mu_{ij}$ | 0.7 e nm | 4.7 e nm | 0.10 e nm |
| $\Gamma$ | | $6 \cdot 10^{-3}$ | |
| $\epsilon_{bg}$ | | 13 | |
| $V$ | | 1200 nm$^3$ | |

**Table 5.1:** Quantum dot parameters. $\mu_{ij}$ is the dipole moment between $|i\rangle$ and $|i\rangle$. $V$ is volume of a single QD, $\Gamma$ is the confinement factor and $\epsilon_{bg}$ is electric permitivity of the surrounding material.

### 5.3.2 Including Inhomogeneous broadening

QDs suffer from inhomogeneous broadening, mainly caused by the fluctuating QD sizes in the ensemble. The typical spectral FWHM of the IHB of the ground state transition is in the range of 10 meV $-$ 100 meV [78, 95, 129, 139, 140]. This is compared to the typical homogeneous linewidths of the ground state transition at low temperatures ($\sim$ 7 K) being $\sim 1$ $\mu$eV.

In order to simplify the inclusion of IHB, we assume that the broadening is only attributed varying quantum confinement potentials as a result of size fluctuations. Hence, strain effects and material composition that might depend on the QD size are not considered. The nature of quantum confinement insures that small dots have more energetic states than larger dots. For a given shift in size, the pump and probe transition energy will not necessarily shift by an equal amount. The ratio between the two shifts depends on the type of confining potential, the coupling scheme and the effective electron and hole masses. To simplify matters, the calculations in this chapter only consider infinite confining potentials. Finally, due to the larger effective mass of a hole, valence band energy levels are assumed constant with respect to the size of the quantum dot.

#### Modelling the QD eigenenergies

Treating the quantum dot as a quantum disc with height $\ell$ and radius $a$, we consider the problem in cylindrical coordinates $\mathbf{r} = (\rho, \phi, z)$. The wavefunction of a particle inside this potential can be written[126]:

$$\psi(\mathbf{r}) = \frac{1}{2\pi} C_{ln} \, \mathrm{e}^{im\phi} \, J_l(p\varrho) \cos(k_z z) \,, \tag{5.10}$$

where $C_{ln}$ is a normalization constant, $J_m(p\varrho)$ is the Bessel function of the first kind, $p$ and $k_z$ are constants determined by the boundary condition (i.e. $k_z = m\pi/\ell$). The eigenenergy is given as

$$E_{nlm} = \frac{\hbar^2}{2m_e^*} \left( \left(\frac{Z_{nl}}{a}\right)^2 + \left(m\frac{\pi}{\ell}\right)^2 \right) \,, \tag{5.11}$$

where $Z_{nl}$ defines the n'th rooth of the l'th Bessel function, i.e. $J_l(Z_{nl}) = 0$. As pointed out in [126], in the case of having a sufficiently flat disc ($\ell < 1.82a$),

the first two exited electron states are given by

$$\varepsilon_{101} = \frac{\hbar^2}{2m_e^*}\left(\left(\frac{Z_{10}}{a}\right)^2 + \frac{\pi}{\ell}\right) \qquad \varepsilon_{111} = \frac{\hbar^2}{2m_e^*}\left(\left(\frac{Z_{11}}{a}\right)^2 + \frac{\pi}{\ell}\right). \qquad (5.12)$$

Considering only transversal size fluctuation, a small shift $\delta a$ in size will induce shift of the energy levels by

$$\delta\varepsilon_{101} = -\frac{\hbar^2}{m_e^*}\frac{Z_{10}^2}{a^3}\delta a \approx -\frac{\hbar^2}{a^3 m_e^*}5.783\,\delta a \qquad (5.13)$$

and

$$\delta\varepsilon_{111} = -\frac{\hbar^2}{m_e^*}\frac{Z_{11}^2}{a^3}\delta a \approx -\frac{\hbar^2}{a^3 m_e^*}14.682\,\delta a\,. \qquad (5.14)$$

Linearising the problem is justified since the inter-band transition energy is typically $\sim 1$ eV, and the inhomogeneous broadening is on the order of a few tens of meV[95].

For the pump and probe transition, this leads to different energy shifts depending on the chosen scheme. Relating the energy shift of the two electron eigen energies, it is seen that the ratio $\frac{\delta\varepsilon_{111}}{\delta\varepsilon_{101}}$ is a constant independent of both $a$ and $m$. With this, we can relate the spectral shift of the probe transition, $\Delta_{ih,p}$, to the spectral shift of the coupling transitions $\Delta_{ih,c}$. The three schemes lead to:

$$\Xi : \Delta_{ih,c} = \quad \frac{\delta(\varepsilon_{111}-\varepsilon_{101})}{\delta\varepsilon_{101}}\Delta_{ih,p} \quad \approx 1.54\Delta_{ih,p} \qquad (5.15)$$

$$\text{V} : \Delta_{ih,c} = \quad \frac{\delta\varepsilon_{111}}{\delta\varepsilon_{101}}\Delta_{ih,p} \quad \approx 2.54\Delta_{ih,p} \qquad (5.16)$$

$$\Lambda : \Delta_{ih,c} = \quad \frac{\delta(\varepsilon_{111}-\varepsilon_{101})}{\delta\varepsilon_{111}}\Delta_{ih,p} \quad \approx 0.60\Delta_{ih,p} \qquad (5.17)$$

For the following we define $\kappa$ as the ratio between $\Delta_{ih,c}$ and $\Delta_{ih,p}$, i.e.

$$\Delta_{ih,c} \equiv \kappa\Delta_{ih,p}\,. \qquad (5.18)$$

Assuming a Gaussian inhomogeneous broadening of the probe transition:

$$f(\Delta_{ih}) = \frac{2\sqrt{\ln(2)}}{\sigma_{ih}\sqrt{\pi}}\exp\left(-4\ln(2)\frac{\Delta_{ih}^2}{\sigma_{ih}^2}\right), \qquad (5.19)$$

where $\sigma_{ih}$ is the FWHM of the probe transition, the mean electric susceptibility is calculated as:

$$\langle\chi(\Delta_p,\Delta_p)\rangle = \int_{-\infty}^{\infty} f(\Delta_{ih})\chi(\Delta_p - \Delta_{ih},\Delta_c - k\Delta_{ih})\,\mathrm{d}\Delta_{ih}. \qquad (5.20)$$

### 5.3.3 Slowdown versus inhomogeneous broadening

From equation 5.20 we can calculate the slowdown factor. In figure 5.10, the slowdown of the $\Xi$-scheme is seen plotted as a function of the coupling intensity for various IHBs. Material parameters are chosen as in 5.1 and with $\gamma_{12} = 2.0$ $\mu$eV corresponding to $\sim 7K$. Furthermore we set $\gamma_{12} = \gamma_{13} = \gamma_{23}$ as in section 5.3.1.
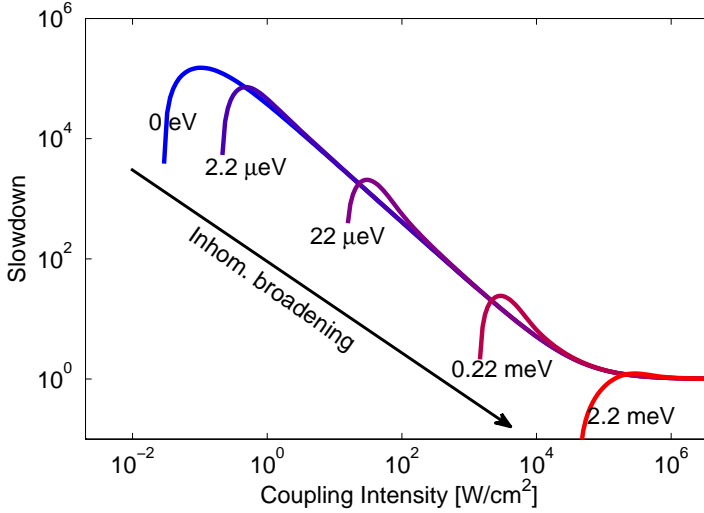


**Figure 5.10:** Slowdown factor as a function of coupling intensity for various inhomogeneous broadenings written as the FWHM. Material parameters as in table 5.1, decay parameters as in table 5.2 at 7 K.

From figure 5.10, it is clearly seen that IHB has a tremendous impact on the achievable slowdown. Notably, at 2.2 meV, all signature of slowdown has vanished. The required coupling intensity, $I_c$ at the maximum slowdown is seen to scale roughly as

$$I_c \propto \sigma_{ih}^2 \tag{5.21}$$

This stems from the fact, that the Rabi splitting needs to exceed the IHB. Thus the relation $\Omega_c \gtrsim \sigma_{ih}$ gives a quadratic scaling of the intensity that for realistic IHBs ($> 1$ meV) requires a very strong coupling intensity . At large rabi frequencies of the coupling field, the slope of $\chi'$ is roughly inversely proportional to the Rabi frequency. Hence we can derive the following scaling law: $S_{max} - 1 \propto \partial_\omega n \propto \partial_\omega \chi^{-1/2} \propto \Omega_c^{-1/2} \propto I_c^{-1}$. Combing this with the relation (5.21) we get

$$S_{max} - 1 \propto \sigma_{ih}^{-2}. \tag{5.22}$$

Consequently, the slowdown factor is roughly inversely proportional to the IHB squared, as is also verified from the figure.

It is tempting to think, that dephasing is the main problem for achieving EIT in QDs. Surely, dephasing has an impact as seen from figure 5.9, but unless room temperature operation is essential, the problem can be minimised by cooling. The problem seems more serious with IHB. Since today's QD samples exhibit IHB ranging from $10 - 100$ meV, it is clearly seen, that IHB simply cannot be ignored when trying to achieve EIT in an ensemble of QDs.

In the following section, the three schemes $\Xi$, V and $\Lambda$ are compared with focus on the sensitivity towards IHB using slightly modified parameters.

### 5.3.4 Comparison of slowdown factor

In the following, we use QD parameters close to measured values by Heitz et al. [95]. In this paper they report on QDs with an exceptionally low intra-band population decay rate. It is demonstrated, that the geometrical shape of the QDs can be tailored to either enhance or reduce the exciton-LO-phonon coupling[95, 141]. In the latter case, truncated pyramidal shaped QDs where used, giving measured intra-band relaxation rates $\sim$15 time lower than the radiative population decay rate of the ground state transition. Later, we shall discuss the consequences of using typical QDs with a much faster intra band decay rate. To the author's knowledge, no measurement has so far been published, giving the measured population decay and dephasing rates on the same QD sample for transitions related to those depicted in figure 5.8. Thus, the used population decay rates are similar to those measured in [95], while the dephasing rate $\gamma_{12}$ is similar to [77] and $\gamma_{23}$ is estimated[6] from measurements in [96]. We tentatively set $\gamma_{13}$ equal to $\gamma_{21}$. The chosen decay rates are shown in table 5.2, while the material parameters are shown in table 5.1.

| Parameter | $|1\rangle \leftrightarrow |2\rangle$ | $|1\rangle \leftrightarrow |3\rangle$ | $|2\rangle \leftrightarrow |3\rangle$ |
|---|---|---|---|
| $\Gamma_{ij}$ | 2.6 $\mu$eV[95] | 0.16 $\mu$eV [95] | 2.6 $\mu$eV |
| $\gamma_{ij}$ @ 7K | 2.1 $\mu$eV[77] | 2.1 $\mu$eV | 2.1 $\mu$eV |
| $\gamma_{ij}$ @ 25K | 7.8 $\mu$eV [77] | 7.8 $\mu$eV | 7.8 $\mu$eV |
| $\gamma_{ij}$ @ 50K | 36.6 $\mu$eV[77] | 36.6 $\mu$eV | 36.6 $\mu$eV |
| $\gamma_{ij}$ @ 75K | 118.8 $\mu$eV[77] | 118.8 $\mu$eV | 118.8 $\mu$eV |
| $\gamma_{ij}$ @ 100K | 218.8 $\mu$eV[77] | 218.8 $\mu$eV | 218.8 $\mu$eV |

**Table 5.2:** Used decay parameters for the simulations including IHB. $\Gamma_{ij}$ and $\gamma_{ij}$ are the population decay rate and homogeneous linewidth of the transition $|i\rangle \leftrightarrow |j\rangle$, respectively.

In figure 5.11 the slowdown factor is seen plotted as a function of coupling intensity for the three different schemes using (5.4)- (5.5). Decay parameters used are shown in table 5.2 at 7 K and the IHB was chosen to 2 eV. Comparing the three schemes without IHB (dashed lines), the $\Xi$ and V- scheme show

---

[6]Since the temperatures measured at, was not the same in [96] as for [77], decay rates were extracted by linear interpolation.
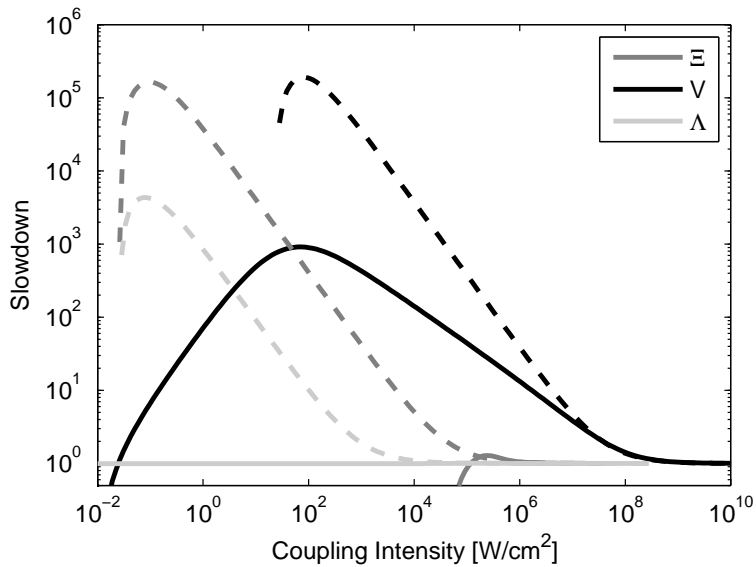
**Figure 5.11:** Comparsion of slowdown factor as a function of coupling intensity for the three schemes $\Xi$ (grey), V (black) and $\Lambda$ (light grey), with (solid) and without (dashed) IHB. IHB was chosen to 2 eV while the chosen decay parameters corresponds to 7 K and are presented in table 5.2. Material parameters are presented in 5.1.

similar maximum slowdown although with different coupling intensities. This is caused as a result of the weak dipole moment between $|1\rangle$ and $|3\rangle$. Thus, for the V-scheme, a fairly high intensity is required in order to realise the required Rabi frequency. The $\Lambda$-scheme, however, shows a somewhat lower slowdown factor. Since the IHB was set relative to the ground state transition ($|1\rangle \leftrightarrow |2\rangle$), the effective IHB on the probe transition of the $\lambda$-scheme ($|1\rangle \leftrightarrow |3\rangle$) will be larger[7], thereby giving a decreased slowdown performance.

When comparing the calculated slowdown including IHB, it is seen, that the V-scheme is far superior. For the two other schemes, the inhomogeneous broadening is seen to completely destroy any slowdown effect, whereas for the V scheme, a slowdown factor of more than $10^3$ is possible. Also the required power on the coupling laser is less by roughly 3 orders of magnitude relative to the other two schemes.

In order to understand this notable difference, we shall examine how the electric susceptibility depends on both $\Delta_{ih}$ and $\Delta_p$. This dependence is plotted in figure 5.12. Left middle and right column are the electric susceptibil-
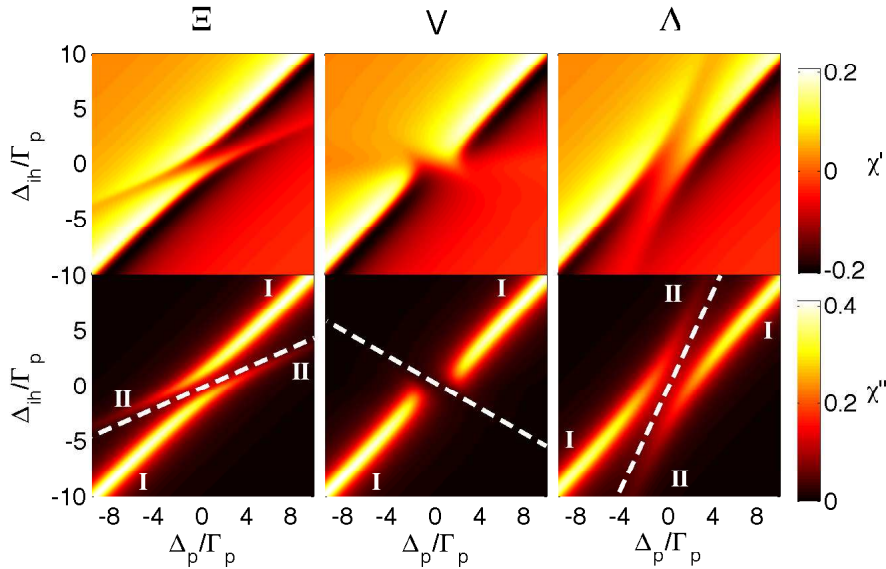


**Figure 5.12:** Normalised electric susceptibility (in units of $\Gamma\mu_p^2/(\varepsilon_0\hbar\Omega_p)$) as a function of the normalised probe detuning, $\Delta_p$, and spectral shift $\Delta_{ih}$. Left middle and right column is for the $\Xi$, V and $\Lambda$, respectively, while the top and bottom row is the real and imaginary part of the susceptibility, respectively. Two-photon resonance is indicated

ity of the $\Xi$-, V- and $\Lambda$-scheme respectively, with the top and bottom plots showing the respective real and imaginary part of the normalised susceptibility

---

[7]similar to equation 5.16, it will be larger by a factor of $\epsilon_{111}/\epsilon_{101} \approx 2.54$

$\chi_p/[\varrho\mu^2/(\varepsilon_0\hbar)]$ (see equation (5.3)). Once again, the primary and secondary resonance have been illustrated by I and II, respectively. With the inclusion of IHB, the two-photon resonance condition in equation (5.8), is found as:

$$0 = \Delta_p - \Delta_{ih} \pm (\Delta_c - \kappa\Delta_{ih}), \tag{5.23}$$

where the sum applies to the cascade and the difference is for the V and $\Lambda$-scheme, Setting $\Delta_c = 0$ we find the linear relation between the probe detuning and the spectral shift:

$$\Delta_{ih} = \frac{1}{1 \pm \kappa}\Delta_p. \tag{5.24}$$

The equality 5.24 is illustrated as a dashed line in figure 5.12. Since $\kappa > 1$ for the $\Xi$-scheme and $0 < \kappa < 1$ for the $\Lambda$-scheme it is seen from (5.24), that the slope of the two photon resonance condition is positive. However,since $\kappa > 1$ for the V-scheme, the two-photon resonance exhibits a negative slope.

Looking at the absorption (bottom row) of the $\Xi$- and $\Lambda$-scheme it is seen that close to the two-photon resonance the secondary absorption resonance peak appears, while the primary absorption resonance peak is located along the line $\Delta_{ih} = \Delta_p$, as expected. One notable difference is that the slope of the two-photon resonance is negative for the V-scheme, while it is positive for the other two schemes. For $\Xi$ and $\Lambda$, this causes the secondary resonance to cross the region where $\Delta_p = 0$. Thus, calculating the average absorption from (5.20) reaveals that EIT is destroyed. This, however, is not the case for the V-scheme as is seen from figure 5.12. Firstly, as mentioned in section 5.2, the V scheme shows no clear signature of the secondary resonance since the coupling field excites carriers. For those QDs where the coupling laser is far off resonance i.e., $\Delta_{ih} \gg 0$ carriers from $|1\rangle$ are no longer excited to $|3\rangle$ and as a result, absorption from the two-photon pathway vanishes. Secondly, even the slightest contribution from the secondary resonance never crosses the region where $\Delta_p = 0$ since the slope of the two-photon resonance,$(1-\kappa)^{-1}$ is negative. To this we may add, that this observation holds true even when using a more advanced model. E.g. using a more realistic model for calculating the QD eigenenergies as well as including the energy shifts of the holes.

In order to investigate the feasible operating temperatures, the slowdown of the V- scheme was calculated for various dephasing rates, corresponding to different temperatures. The decay parameters are shown in table 5.2. We note, though, that the homogeneous linewidths $\gamma_{23}$ and $\gamma_{13}$ was tentatively set equal to $\gamma_{12}$. While this might be a good assumption at low temperature, the assumption may be less appropriate at higher temperatures. Nevertheless, in figure 5.13 the slowdown factor as a function of coupling intensity is plotted at various temperatures. From the solid lined plots it is seen that the slowdown is still strongly dependent on the dephasing rate and thereby the temperature. The dashed lines are calculations using similar parameters as for the solid lines except $\gamma_{23} = 1000\gamma_{12}$. In this case, all coherence between the terminal states are immediately lost, and as a result, no effects from EIT is expected. Nevetheless, from figure 5.13, slowdown effects are still clearly present. This, incoherent, slowdown is due to spectral holeburning from the coupling field. The holeburning causes the probe to experience a reduced absorption near its
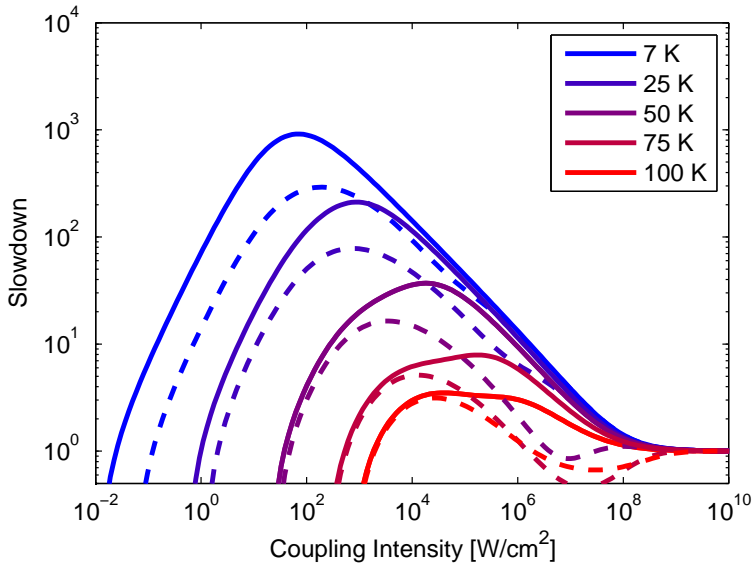
**Figure 5.13:** Slowdown of the V-scheme as a function of coupling intensity for various temperature. Decay parameters are chosen as in 5.2. Material parameters are chosen as in table 5.1. Dashed lines, are with the same parameters except $\gamma_{23} = 1000\gamma_{12}$.

resonance that leads to a positive slope of the refractive index. Thus, calculating the slowdown of the V-scheme inevitably leads to a slowdown consisting of contributions from both EIT and SHB. Notably this is observed in figure 5.11, where for decreasing coupling intensity, the slowdown is seen to drop off more gradual than for the alternate schemes, due to the SHB generated slowdown. Slowdown solely based on SHB, is indeed a much simpler task, however, as seen from figure 5.13, exploiting EIT results in a slowdown factor roughly five times as large.

The previous calculations were based on QDs with an exceptionally long intra-band scattering time $\Gamma_{23}$. Measurements on the intraband scattering time of QDs are typically $1 - 5$ ps [97, 142, 143]. In this case, the system would act as an amplifier with electrons pumped by the coupling field from $|1\rangle$ to $|3\rangle$ and quickly decaying to $|2\rangle$. This is illustrated in figure 5.14 where the real (left) and imaginary (right) part of the susceptibility is plotted as a function of the probe detuning, for various intraband scattering rated $\Delta_{23}$. For $\Delta_{23} = 0$,
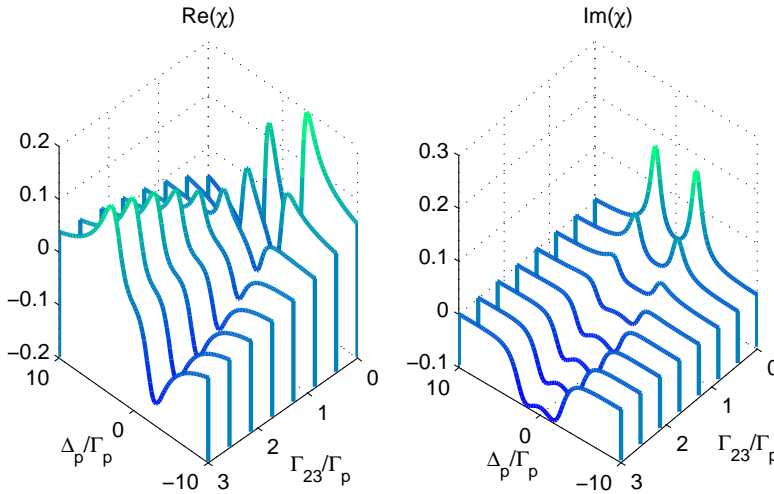


**Figure 5.14:** Normalised real (left) and imaginary (right) part of the electric susceptibility, for various intraband population decay rates, $\Gamma_{23}$

the absorption spectrum shows Rabi splitting as a result of the strong coupling field. However, as $\Gamma_{23}$ is gradually increased, the absorption becomes negative (i.e. amplication). Considering the real part of $\chi$ (left), it is seen, that the slope remains positive, giving reduction of the group velocity even for high values of $\Gamma_{23}$. However, this effect is completely incoherent, with less sharp features of $\chi'$ near zero detuning. It is interesting to note though, that the two effects support each other. Thus, for intermediate values of $\gamma_{23}$ an effective slowdown may be achieved by EIT, while minimising the absorption due to the small fraction of carriers being pumped to the probe transition.

## 5.4 Delay and transmission comparsion

Since the V-scheme turns out being much more robust against IHB, using a waveguide structure is an efficient way of increasing the interaction length and thereby increase the possible delay. However, as opposed to the two other schemes, the coupling field is subject to carrier absorption on the transition $|1\rangle \leftrightarrow |3\rangle$. An upper limit on the achievable delay is therefore expected. The situation is illustrated in figure 5.15. I.e. for a long waveguide the coupling
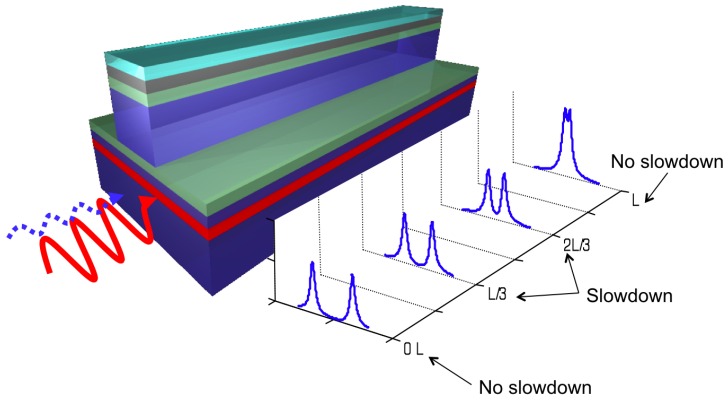


**Figure 5.15:** Illustration of using a ridge waveguide structure for the V scheme to increase the interaction length of the probe. The graph illustrates the absorption spectrum at various propagation lengths. Absorption of the coupling field causes the probe to experience an increasing absorption propagating down the device. The slowdown is optimised in a section where the coupling field is saturated to the optimal strength.

field is initially very strong and generates a large Rabi-splitting. The probe absorption in this section is very low, and so is the slowdown effect. At the end of the device, on the other hand, the coupling field is absorbed such that the limited Rabi splitting causes a high degree of absorption, while the slowdown effect on the probe has vanished. Since this problem is avoided with the $\Xi$- and $\Lambda$-scheme, a comparison of the delay and transmission of the three schemes is reasonable. In the following, the propagation model of both the probe and coupling field are described, before discussing the results of the calculated delay and transmission.

### 5.4.1 Propagation of the coupling beam

Assuming a monochromatic coupling field, the propagation of the coupling field is governed by equation (2.12). Using equation (5.3) we find:

$$\partial_z \mathcal{E}_c(z) = \mathrm{i}\, \frac{\omega_c}{2n_0\varepsilon_0 c} \mathcal{P}(z) = \mathrm{i}\, \frac{\Gamma}{V}\frac{\omega_c}{2n_0\varepsilon_0 c}\mu_{23}\langle\rho_{13}(z)\rangle\,, \tag{5.25}$$

where $\Gamma$ is the confinement factor and $V$ is the volume of a single QD. $\langle\rho_{13}(z)\rangle$ is the average matrix element over all quantum dot sizes and is solved in the steady state assuming that the probe beam is sufficiently weak. Since the probe is assumed weak, we can simplify the computations by approximating the pump transition to be a pure 2-level problem, with two decay channels: One directly from $|3\rangle$ to $|1\rangle$ and another via the state $|2\rangle$, where the population decay rate for the latter channel is given by $\left(\Gamma_{23}^{-1} + \Gamma_{12}^{-1}\right)^{-1}$. This approximation is valid as long as the probe is weak and $\Gamma_{23} \ll \Gamma_{12}$, meaning that $\rho_{22} \ll 1$ . In this case $\rho_{13}$ is easily solved analytically using equations (2.28) :

$$\rho_{13}(z,\delta_c) \approx \Gamma_{\mathrm{eff}}\Omega_c \frac{(i\gamma_{13} - \delta_c)}{(\delta_c^2 + \gamma_{13}^2)\,\Gamma_{\mathrm{eff}} + 4\gamma_{13}\Omega_c(z)^2}, \tag{5.26}$$

where $\Gamma_{\mathrm{eff}} = \Gamma_{23} + \left(\Gamma_{12}^{-1} + \Gamma_{13}^{-1}\right)^{-1}$ and $\delta_c$ is the relative probe detuning with respect to a certain QD size class, i.e. $\delta_c = \Delta_c - \kappa\Delta_{ih}$. Averaging over all quantum dots we get:

$$\langle\rho_{13}(z,\Delta_c)\rangle = \int\limits_{-\infty}^{\infty} f(\Delta_{ih})\rho_{13}(z,\Delta_c - \kappa\Delta_{ih})\mathrm{d}\Delta_{ih} \tag{5.27}$$

We note that for a sufficiently weak coupling field, the coupling field experience on average[8] absorption in accordance with the Beer-Lambert law [8], i.e. $I_c(z) = I_c(0)\exp(-z/z_0)$, where $z_0$ is the attenuation length given by

$$z_0 = \left(\frac{\Gamma}{V}\frac{\omega_c}{n_0\varepsilon_0 c}\mu_{23}\langle\rho_{13}(z)\rangle\right)^{-1}. \tag{5.28}$$

However, since EIT requires a sufficiently large Rabi splitting on the coupling transition, the absorption is saturated by the coupling field. The coupling is therefor subject to less absorption than predicted by the Beer-Lambert relations.

---

[8]We note that it is on average, since the coupling field coherently drives the carriers at the Rabi freuqnecy.

### 5.4.2 Propagation of the probe beam

The propagation of the probe through the QD waveguide is calculated using the wave equation (2.10). As with the coupling field, we solve $\rho_{12}$ in the steady state that is valid for probe pulses with a spectral width sufficiently narrow to give a negligible GVD induced by the QD material. Fourier transforming (2.10), results in

$$\frac{\partial \mathcal{E}(z,\Omega)}{\partial z} = i\left(\frac{\Omega}{u_g} + \frac{\omega_0}{2n_0 c}\chi_{qd}(z)\right)\mathcal{E}(z,\Omega), \tag{5.29}$$

where $\Omega = \omega - \omega_0$. Equation (5.29) is formally solved to give:

$$\mathcal{E}(z,\Omega) = \mathcal{E}(0,\Omega)\exp\left[i\,z\left(\frac{\Omega}{u_g} + \frac{1}{z}\frac{\Omega+\omega_0}{2n_0 c}\int_0^z \chi_{qd}(\tilde{z},\omega)\,\mathrm{d}\tilde{z}\right)\right]. \tag{5.30}$$

Noting that (5.30) takes the form $\mathcal{E}(z) = \mathcal{E}(0)\exp(ik)$ we can immediately extract the group index using the relation $n_g/c = \partial\Re(k)/\partial\omega|_{\omega_p}$:

$$\langle n_g(\omega)\rangle = \frac{c}{u_g} + \frac{1}{z}\frac{1}{2n_0}\int_0^z\left(\chi'_{qd}(\tilde{z},\omega) + \omega\frac{\partial\chi'_{qd}(\tilde{z},\omega)}{\partial\omega}\right)\mathrm{d}\tilde{z}. \tag{5.31}$$

Notice that equation (5.31) describes the average group index, over the length $z$ through the device. The local group index at the position $z$, is given as

$$n_g(\omega,z) = \frac{c}{u_g} + \frac{1}{2n_0}\left(\chi'_{qd}(z,\omega) + \omega\frac{\partial\chi'_{qd}(z,\omega)}{\partial\omega}\right) \tag{5.32}$$

From equation (5.32) it is easily shown that if the background group velocity, $u_g$ is set equal to the background phase velocity, i.e. $\partial k/\partial\omega|_{\omega_0} = k/\omega$, we recover the usual relation for the group velocity: $n_g(\omega_p) = n + \omega_p\partial n/\partial\omega_{\omega_p}$.

An example of the calculated local and average group index is plotted in figure 5.16 as a function of propagation length and injected coupling intensity. The coupling and probe detuning are chosen on resonance with the inhomogeneous broadened coupling and probe transition, respectively. Considering the local group index, it is seen that in a narrow segment of the device the group index is maximised. In the part of the wave guide before this segment the coupling field is too strong, whereas in the remaining part it is too weak. As a result, the calculated average group index is largest for a short device as seen in figure 5.16 (right). Making the device longer, requires a stronger coupling field to reach the maximum slowdown factor that in turn decrease the maximum average group index factor. Thus, in terms of buffering capacity, simply making the device twice as long does not make the delay twice as big. The delay is calculated as:

$$\Delta t = \frac{z}{c}\left(\langle n_g(z)\rangle - n_{bg}\right) \tag{5.33}$$

and is plotted in figure 5.17. The results show that a given input coupling intensity, the delay initially increases with $z$ until a certain point. Hereafter no additional delay is achieved by making the device longer.
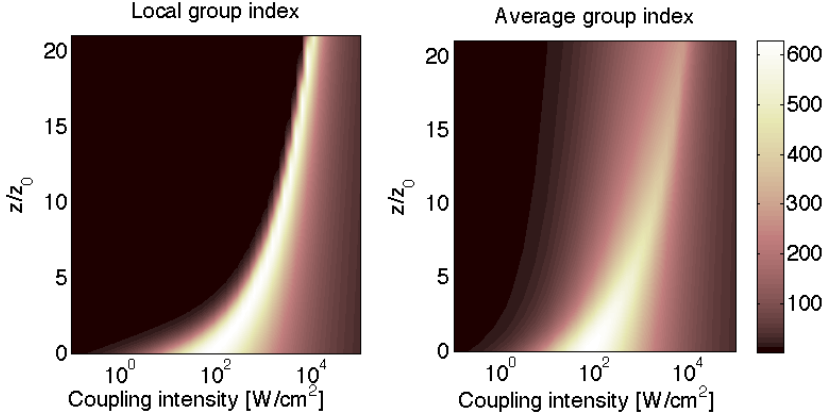
**Figure 5.16:** Calculated local (left) and average (right) group index as a function of propagation length and injected coupling intensity. The propagation length is normalised by the coupling field attenuation length $z_0$. Calculations are based on equations (5.32) and (5.31). Material parameters are chosen as in table 5.1 and decay parameters as in table 5.2 at 7 K. FWHM of the inhomogeneous broadening was set to 10 meV.

Figure 5.17 shows that the delay can be increased simply by increasing the propagation length while also increasing the coupling field. However, for long propagation lengths, a finite probe absorption may lead to an unacceptably low transmission. To address this issue, in figure 5.18, the delay and transmission are plotted as a function of propagation length $z$ and injected coupling intensity for all three schemes Ξ, V and Λ. The surface plot shows the delay in units of ns, while the lines on top shows iso-curves of the calculated transmission in dB. Noting the different scaling on the associated color bar, it is seen that for the Ξ and Λ scheme, hardly any positive delay is possible as a result of the large IHB. For the V scheme, however, a considerable delay, on the order of ns, is be obtained. Furthermore, it is seen that the required coupling intensity for maximum delay, is considerably larger for both the Ξ and Λ scheme compared to the V scheme. In fact, such high coupling intensities inevitably requires a strong field confinement such as in a waveguide. However, for these schemes, the coupling transition is typically around 10 $\mu$m whereas the probe transition is roughly 1 $\mu$m. Fabricating a waveguide for both wavelengths is a difficult task.

Considering the calculated transmissions, the Λ-scheme shows a considerable larger transmission compared to the other two schemes. This is a result of the small dipole moment of the probe transition in the Λ scheme. However, this also affects the achievable delay being very small.

Inevitably what sets the limit of the achievable delay, is the tolerated absorption of the probe signal. A plot of the delay as a function of coupling intensity along the -10 dB transmission is seen in figure 5.19 comparing the V and Ξ scheme. From the inset it is seen that the delay of the Ξ scheme continues to grow for increasing coupling intensity. This is due to the fact that
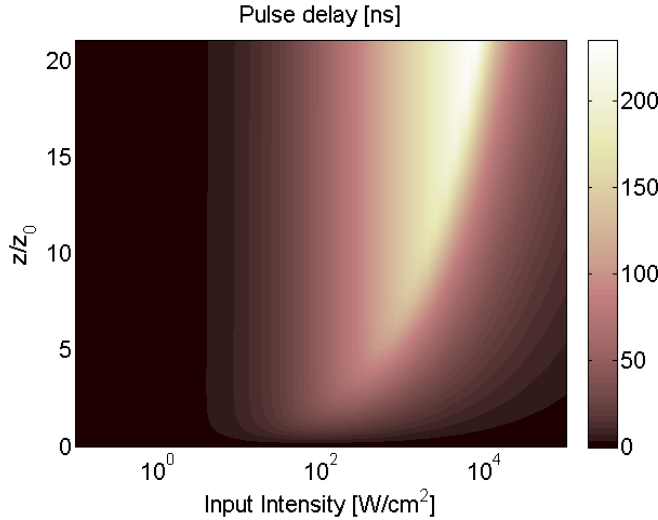
**Figure 5.17:** Calculated delay as a function of propagation length and injected coupling intensity. The propagation length is normalised by the coupling field attenuation length $z_0$. Material parameters are chosen as in table 5.1 and decay parameters as in table 5.2 at 7 K. FWHM of the Inhomogeneous broadening was set to 10 meV.

the coupling field does not experience any absorption. Thus, by increasing the propagation length, the achieved delay may be increased. However, group dispersion and waveguide losses, that have not been included in the model, sets an upper limit on the device length. This monotonically increasing delay does not hold for the V scheme where the delay is seen to reach a maximum. Thus, the achieved delay is almost constant from 500 W/cm$^2$ only changing by less than 10 %. Considering the device length, indicated by arrows, this implies that very little is gained by making the device longer than $\sim 1$ mm.

## 5.5 Conclusion

Electromagnetically induced transparency based on the three schemes $\Xi$, V and $\Lambda$, were analysed and compared. For an ideal atomic system, the $\Lambda$-scheme is best suited to achieve full transparency. Applying the schemes to a quantum dot system, shows that the large dephasing rates rules out applications of EIT in a QD system at room temperature. Furthermore, inhomogeneous broadening was shown to have an adverse effect on EIT features for the $\Xi$ and $\Lambda$ scheme where no slowdown is possible for a realistically inhomogeneously broadened ensemble. This is not the case for V scheme showing a slowdown factor of more than $10^3$. This notable difference is caused by two properties
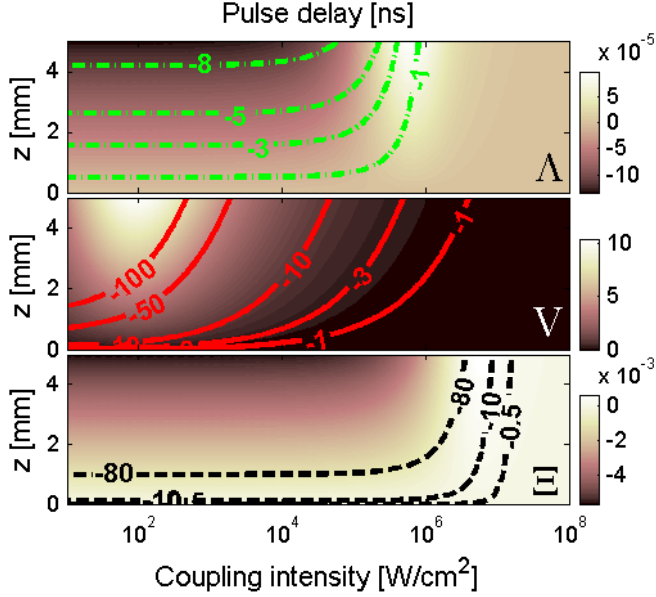
**Figure 5.18:** Calculated delay (surface plot) and transmission (isocurves) as a function of injected coupling intensity and propagation length $z$ for the $\Lambda$- (top), V- (middle) and $\Xi$-scheme (bottom). The transmission curves are labelled with the corresponding transmission in dB. Note from the colorbar the different scales of the delay. Material parameters are chosen as in table 5.1 and decay parameters as in table 5.2 at 7 K. FWHM of the Inhomogeneous broadening was set to 10 meV.

special for this scheme: Firstly, the V-scheme relies on carrier excitations on the coupling transition. Thus, QDs far off resonance are not exited and do therefore not influence the induced coherence in resonant QDs. Secondly, the two-photon resonance condition has a negative slope between the probe detuning and inhomogeneous spectral shift. This prevents absorption of the probe via the two-photon absorption path of resonant QDs. Finally, the probe delay and transmission of the three schemes were compared. Despite the finite absorption of the coupling field in the V-scheme, the achievable delay is far superior compared to the other schemes. Due to the absorption of the coupling field it was shown that the achievable delay at a fixed transmission of -10 dB is constant for all propagation lengths longer than 1 mm with a delay of roughly 0.8 ns.
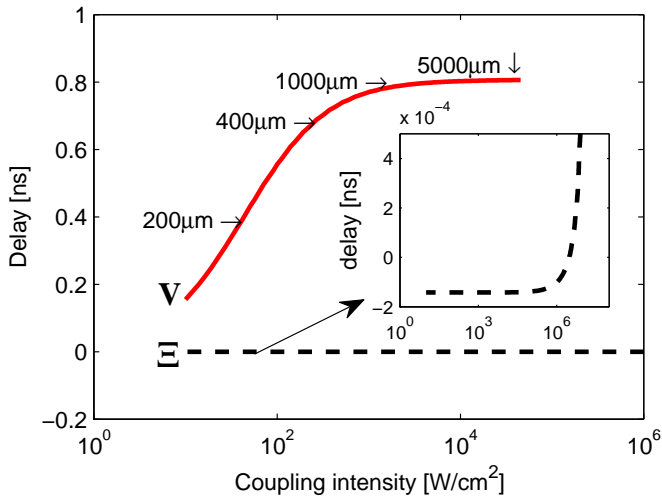
**Figure 5.19:** Delay as a function of the injected coupling intensity at a fixed transmission of 10 dB for the V- (solid) and Ξ-scheme (dashed). Parameters are chosen as in figure (5.18). Corresponding propagation length is illustrated by arrows for the V- scheme. Inset shows a zoom in of the calculated delay of the Ξ-scheme.

# Pump-probe measurements of a quantum dot SOA

In this chapter, the gain dynamics of a quantum dot semiconductor amplifier are measured using degenerate transmission pump probe spectroscopy and the results are analysed. The experiments were carried out using the setup described in chapter 3. The device was grown and processed at the Alcatel-Thales III-V Lab, and supplied by the group of Jean-Claude Simon at ENSSAT Lannion, France. Both wavelength dependence and the carrier injection dependence of the gain dynamics are analysed and compared with earlier work.

## 6.1 Principles of pump-probe measurements

Pump-probe measurements refer to a general technique, where a strong pump laser pulse excites the sample under investigation. A subsequent weak pulse, delayed relative to the pump field by an optical delay path, probes the induced changes. Some property related to the probe beam is subsequently measured as a function of the introduced delay, e.g. transmission, reflection, four wave-mixing, photon echo etc. [73, 144]. The temporal resolution of such a measurement is ultimately limited by the pulse length. Since many important physical processes related to absorption and stimulated emission in semiconductor material occur on a sub-picosecund time scale (see chapter 2), laser pulses with a duration <200 fs are required to measure the optical response.

In this section, the gain dynamics of an QD SOA are presented based on transmission pump probe measurements. I.e., the transmission of a weak probe is measured with and without a pump pulse as a function of the probe delay. Both pump and probe pulse share the same wavelength (see section 3), and the technique is thus denoted *degenerate* pump probe response.

## 6.2 The sample

The QD SOA is an InAs/InGaAsP based structure[103] with an ASE emission spectrum centred around 1.5 $\mu$m [145]. The QD density is estimated to a few $10^{10}$ cm$^{-2}$ with an average base width and length of 20 nm and 30 nm. The waveguide is a 2 $\mu$m wide InP single mode ridge wave guide with an estimated optical confinement of $\sim 1\%$. The device is mounted on top of a Peltier cooling element stabilised at 20° C. A bias tee is inserted between the current source and SOA, to make sure that the current source does not compensate for the generated photocurrent.

## 6.3 Experimental procedure

The delay of the reference beam is adjusted for temporal overlap of reference pulse with the transmitted probe pulse. Spatial overlap is optimised by maximising the lock-in signal detecting at the reference-probe beat frequency (see section 3). Since the time for full gain recovery is on the order of 100 ps, the corresponding delay for temporal overlap between pump and probe is easily found by detecting the probe-reference signal while modulating the pump signal with a chopper and moving the delay stage of the pump in large steps. I.e. as long as no modulation in the probe signal is measured due to gain suppression, the pump pulse arrives after the probe, and the optical path of the pump needs to be decreased.

The pump signal is chopped at 15 Hz and the lock-in amplifier integrates over 1 ms. This choice gives a tolerable signal to noise while allowing to detect the fast shift between the "on" and "off" state of the pump. The heterodyne measurement technique (see chapter 3) allows for extraction of both phase and amplitude of the transmitted signal using a dual phase lock-in amplifier [114]. Since the Mach-Zehnder configuration is not phase stable over large times, only the phase difference between the "on" and "off" state are measured. Within a period of the pump modulation, the phase are found acceptably stable.

Measurements are performed in the linear regime, i.e. the measured differential probe transmission scales linearly with pump power. The differential probe transmission is defined as

$$\delta T \equiv \frac{T_w - T_{w.o}}{T_{w.o}} = \frac{V_w^2 - V_{w.o}^2}{V_{w.o}^2}, \tag{6.1}$$

where $V_w$ and $V_{w.o}$ are the measured lock-in signal with and without the pump pulse, respectively. Here, the signals are squared since the balanced heterodyne detection gives a signal proportional to the electric field. An example of the measured differential transmission at a fixed pump delay as a function of pump pulse energy is plotted in figure 6.1. The differential transmission is seen to scale approximately linear with the pulse energy for energies below 2 pJ illustrated
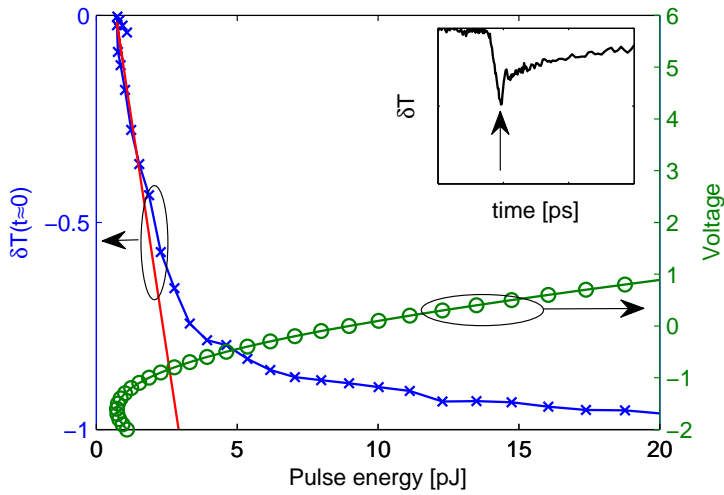
**Figure 6.1:** Differential probe transmission ($\times$) at a fixed pump delay as a function of input energy. The corresponding probe delay relative to the pump is indicated by an arrow on the inset. The pulse energy was changed by changing the voltage controlling the RF amplitude for the AOM, where the AOM voltage versus output pulse energy is plotted ($\circ$). Typically a pump and probe pulse energy of 1 pJ was used.

by the linear fit (red). The pump pulse energy was changed by changing the voltage controlling the RF amplitude fed to the AOM. Since the AOM voltage and pulse energy are not proportional, a mapping between voltage and pulse energy is necessary and is plotted by circles in figure 6.1.

## 6.4 Experimental results

### 6.4.1 Spectral gain dynamics

The spectrum of the ASE as a function of the applied current is shown plotted on a log scale in figure 6.2(left). The associated spectral width $\sigma_{\hbar\omega}$ and mean
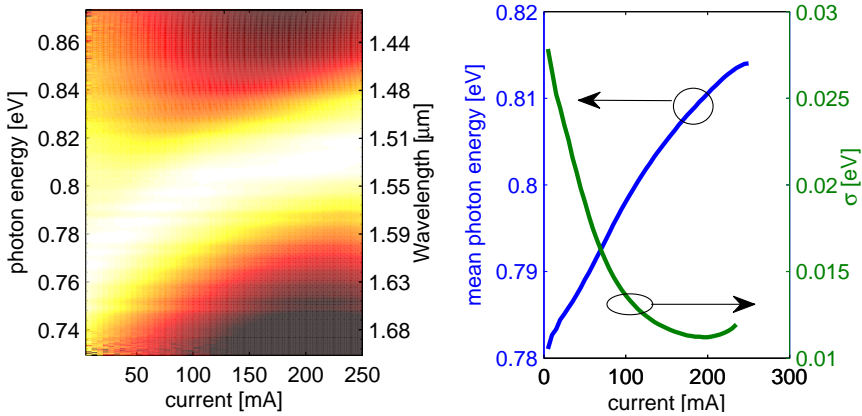


**Figure 6.2:** (left) Normalised ASE spectrum (logarithmic scale) of the SOA as a function of photon energy and current. Small ripples appear as a result of interference, possibly arising from the in-coupling lens . (right) Associated mean photon energy and spectral width, $\sigma_{\hbar\omega}$ (as standard deviation), as a function of current.

photon energy $\langle\hbar\omega\rangle$, defined as

$$\langle\hbar\omega\rangle = \frac{\int \hbar\omega_i\, s(\omega)\,\mathrm{d}\omega}{\int \hbar\omega\, s(\omega)\,\mathrm{d}\omega} \quad \text{and} \quad \sigma_{\hbar\omega} = \sqrt{\langle(\hbar\omega - \langle\hbar\omega\rangle)^2\rangle}, \qquad (6.2)$$

is plotted in figure 6.2(right). It is seen that the mean photon energy inclines as the current is gradually increased and near 250 mA, the incline levels off. This indicates that the sample consists of relatively large QDs with densely spaced states. First off all, no additional peaks or sudden changes in the width or center frequency are observed. For small dots, with only a few quantised states, a roughly constant width and centre frequency is expected at low currents since most electrons and holes relax to the ground state before emitting a

photon [146]. In this case, the spectral width resembles the IHB of the ground state transition. As the current is increased, the first exited transition starts emitting photons resulting in the apperance of second peak [75, 147] resulting in a broadening of the spectrum with an increased mean photon energy. For this sample, the spectral width is seen to decrease with current, which we attribute to a near continous density of states , where the density of states increases with the transition frequency. This leads to a blue shift of the spectrum. We attribute the narrowing of the spectrum to arise from the larger amplification (ASE) of spontaneously emitted photons with a high energy, due to the increasing density of states. Similar measurements have been observed on quantum dash devices [148]. For the lowest current densities, a "shoulder" is observed at high energies, that we attribute to a finite thermal population of excited states [129].

The gain was measured for six different wavelengths with a fixed applied current of 100 mA and a fixed probe and pump energy of 1 pJ. The laser spectra are seen illustrated in figure 6.3, together with the associated ASE. The asymmetry of the laser spectra and the ripples in the ASE spectrum are believed to arise from interference effects from reflections of the in coupling lense. The
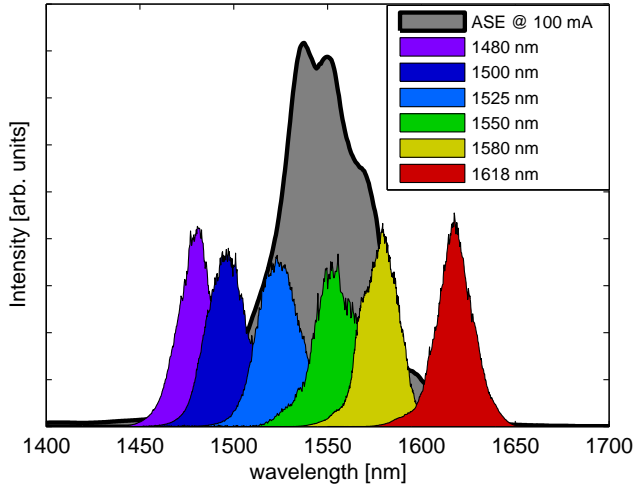


**Figure 6.3:** Spectra of the laser fields used for measurements with a fixed applied current of 100 mA and a fixed probe and pump energy of 1 pJ. The associated ASE is seen plotted in grey. The assymetry of the peaks are mainly due to interference from reflections of the in coupling lens.

transmission was calibrated from the transparency current that was measured by pump-probe transmission measurements. At a delay of 10 ps relative to the pump, all ultra fast relaxation dynamics are vanishing, whereas the slow component related to the recovery of the total carrier density is typically much longer ($\sim$ 100 ps)[57, 93, 94, 149, 150]. Thus, the differential transmission is

positive in the absorbing regime, negative in the amplifying regime and vanishing at the transparency current at a fixed probe delay of 10 ps . We note, that this definition of the transparency current refers to the material gain, i.e. the current at which the rate of stimulated emission equals the rate of absorption. As such, wave guide losses as well as coupling losses are excluded, which implies that the current where the input-output ratio equals unity will in general be larger. An example of the differential transmission as a function of probe delay is plotted in figure 6.4 for three currents corresponding to absorption, close to transparency and amplification. Here, the wavelength was chosen to be 1480
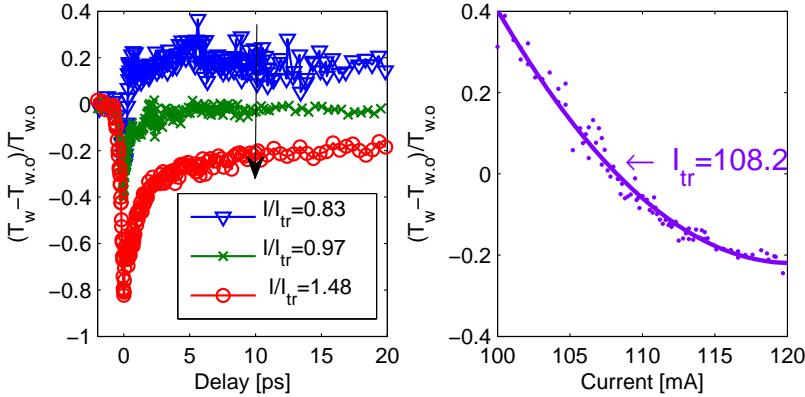


**Figure 6.4:** (Left) Differential probe transmission at 1480 nm for three applied currents corresponding to $I/I_{tr}$ = 0.83, 0.97 and 1.48. (Right) Differential transmission as a function of applied current at a fixed delay of 10 ps. The tranparency current is extracted as the root of a polynomial fit, that is plotted as a solid line.

nm. The differential transmission at a fixed delay of 10 ps is seen plotted as a function of applied current. The transparency current is extracted as the root of a polynomial fit (solid line). The measured transparency currents of all six measured wavelengths are plotted in figure 6.5. From the figure it is clear that the transparency current decreases with increasing wavelength. This observation confirms the suggestion that the QDs are large with many electron-hole states exhibiting fast intraband scattering times. A similar dependence of the transparency current is also observed in [151]. For QDs containing only a single or a few well separated quantum states, where thermal excitation is negligible, the transparency current is expected to be constant with wavelength [152].

The transmission is measured as a function of the current using a detector measuring the transmitted signal. In order to filter out the contribution from ASE, the detector is connected to a lock-in amplifier locked to the laser repetition rate. The transmission is found by subtracting coupling losses ($\sim$0.25), dividing the signal with the measured input energy and finally scaling it to correspond with the measured transparency current. The results are seen in figure 6.6a. From the figure it is seen that the transmission saturates at a
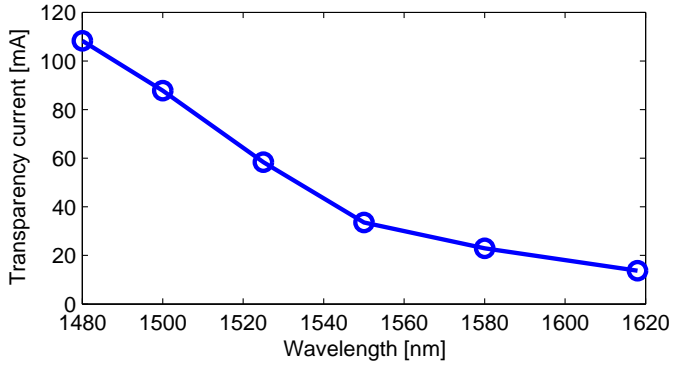
**Figure 6.5:** Measured transparency current as a function of wavelength. The transparency current was found from the measured differential transmission at 10 ps (see figure 6.4).



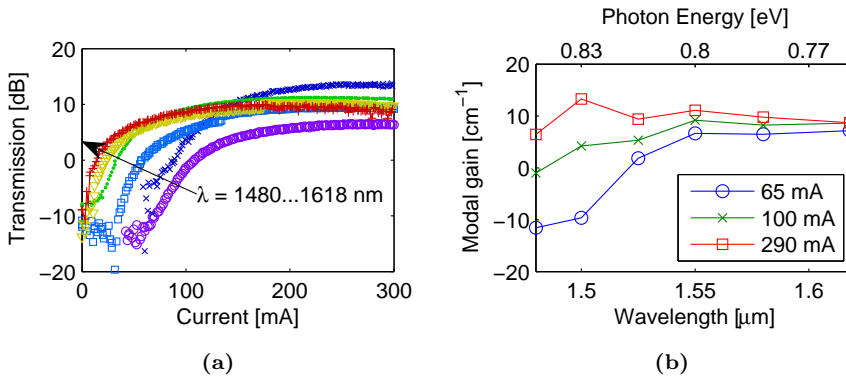|          |          |
| :------: | :------: |
|   (a)    |   (b)    |

**Figure 6.6:** (a) Transmission as a function of current for the laser wavelengths shown in 6.3. (b) Transmission as a function of wavelength for the fixed currents 65 mA, 100 mA and 290 mA.

decreasing current for an increasing wavelength. Furthermore, at low currents it is only the longest wavelengths that give positive gain. The corresponding plots of the transmission as a function of wavelength for three fixed currents is shown in 6.6b. Here it is seen that for low currents $I < 65$ mA, the transmission increases monotonically with increasing wavelength. At larger currents $I \sim 100$ mA, the transmission shows a maximum near 1550 nm. For currents larger than 200 mA, the transmission is saturated for wavelengths in the investigated range, with 1500 nm showing the largest gain. This is in good agreement with the measured ASE spectrum in figure 6.2(left). We note, that for a QD medium consisting of only a single transition, the gain is expected to be independent of the applied current as long as $I/q > \tau_s$. Furthermore the maximum gain is expected near the center wavelength of the inhomogeneously broadened spectrum. From figure 6.6b, it is clearly seen that this is not the case for our sample, confirming that the QD consist of several states. We also note that the transmission shown in 6.6b is in qualitative agreement with the calculated gain spectrum of a QDash medium by Dery *et al.* [148].

### 6.4.2 Temporal gain dynamics versus wavelength

Pump-probe measurements for the six wavelengths shown in figure 6.3 were carried out using a fixed pump and probe energy of 1 pJ, being in the linear regime. The measurements were carried out for a probe delay ranging from -2 ps to 20 ps. The results are plotted in figure 6.7. For a linear gain we may generally write the pump induced changes of gain as

$$\Delta g(t) = \int_{-\infty}^{\infty} h(t - t')\mathcal{S}(t')\,\mathrm{d}t',  \tag{6.3}$$

where $h$ is a response function to the impulse function $\mathcal{S}(t)$ that describes the photon flux, cf. section 1.2.2. Assuming the probe pulse to be a weak replica of the pump, the measured change of the probe transmission as a function of pump delay $\tau$ is given as [84]:

$$\delta T(\tau) = \int_{-\infty}^{\infty} \mathrm{d}t\, \mathcal{S}(\tau - t) \int_{-\infty}^{\infty} \mathrm{d}t'\, h(t - t')\mathcal{S}(t').  \tag{6.4}$$

Since the convolution is Fourier transformed to a product, it is easily shown that equation (6.4) can be written as:

$$\delta T(\tau) = \int_{-\infty}^{\infty} h(\tau - t)G_2(t)\,\mathrm{d}t,  \tag{6.5}$$

where $G_2(t) = \int_{-\infty}^{\infty} S(t')S(t - t')\,\mathrm{d}t'$. Including waveguide propagation, (6.5) can be rewritten as [61]:

$$\delta T(\tau, L) = \frac{\mathrm{e}^{-2\xi_0 L} + \mathrm{e}^{-\xi_0 L}}{\xi_0} \int_{\infty}^{\infty} h(\tau - t)G_2(t)\,\mathrm{d}t  \tag{6.6}$$
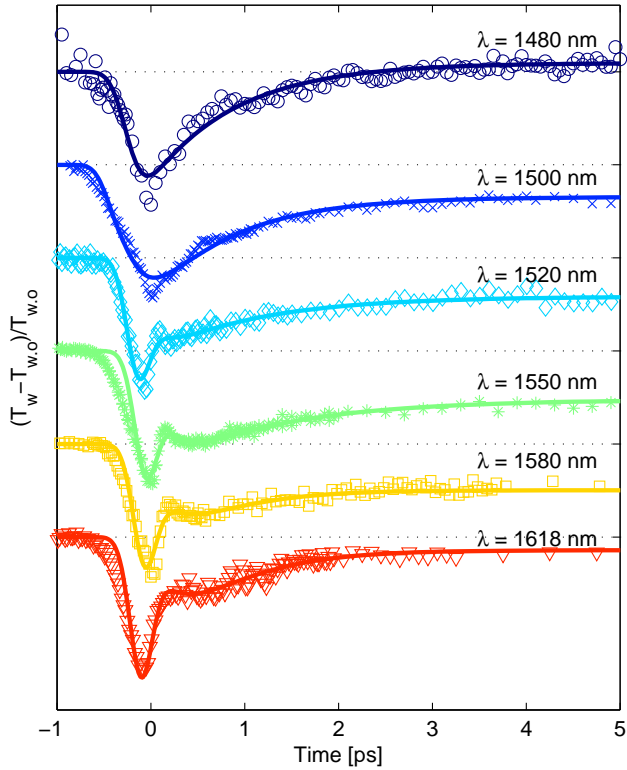
**Figure 6.7:** Differential transmission measurements for various wavelengths and a current of 100 mA. Each plot is scaled and translated for clarity. Solid lines represents fits based on a bi-exponential response function presented in equation (6.7).

where $\xi_0 = \Gamma g_0 - \alpha_{int}$, $G_2(t) = \int_{-\infty}^{\infty} S(t') S(t-t') \, dt'$.

Reasonably good fits were achieved using a bi-exponential response function $h$ [153]. The spectral gain analysis in the previous section suggests large QDs and we therefor tentatively use a response function in a form traditionally used for bulk and QW media [61, 63, 82, 85, 153] . I.e. the response function $h$ is the sum of the four terms

$$h_N(t) = A_N \left( 1 - e^{-t/\tau_2} \right) \Theta(t) \tag{6.7a}$$

$$h_{CH}(t) = A_1 \left( e^{-t/\tau_1} - e^{-t/\tau_2} \right) \Theta(t) \tag{6.7b}$$

$$h_{SHB}(t) = A_2 \, e^{-t/\tau_2} \, \Theta(t) \tag{6.7c}$$

$$h_{TPA}(t) = A_{TPA} \delta(t), \tag{6.7d}$$

where gain dispersion is neglected and $\tau_N \gg \tau_1, \tau_2$ where $\tau_N$ is the recovery time of the total carrier density. $\Theta(t)$ is the Heaviside step function (causality requirement) and $\delta$ is the Dirac delta function (instantaneous). In [61, 85, 153] the subindices N, CH, SHB and TPA naturally refer to the gain contributions of the total carrier density, carrier heating, spectral hole burning and two photon absorption, with relaxation times of the latter two $\tau_1$ and $\tau_2$, respectively. In the linear gain regime, the amplitudes can be derived from the rate equations as [61]:

$$A_N = -\Gamma v_g g_0 \, \partial_N g_0(\omega)|_{\omega_0} \tag{6.8a}$$

$$A_1 = -\Gamma \epsilon_{CH} \gamma_c^{(h)} g_0(\omega_0) \tag{6.8b}$$

$$A_2 = -\Gamma \epsilon_{SHB} \gamma^{(sc)} g_0 \omega_0 \tag{6.8c}$$

$$A_{TPA} = -2\beta_2 \tag{6.8d}$$

where $\epsilon_{CH}$ and $\epsilon_{SHB}$ are the nonlinear gain supression factors related to carrier heating and spectral holeburning, while $\beta_2$ is the two-photon absorption coefficients (cf. equation (2.50)). Especially CH is a process that is only meaning full for a medium exhibiting a continuum of states with an occupation described by a quasi Fermi distribution. In a strongly quantised system, the notion of a Fermi distribution is no longer meaningfull [115]. Nevertheless, the notion of CH has earlier been used for large QDs operating near 1.5 $\mu$m [93, 94].

An important observation of equations (6.7a) and (6.7b) is that the pump induced gain changes, due to CH and changes in $N$, are suppressed during the initial carrier-carrier scattering time $\sim \tau_2$. This relation is due to the fact that for a nonequilibrium carrier distribution, it takes on the order of the carrier-carrier scattering time to equilibrate to a quasi fermi distribution $f_\alpha$, cf. equation (2.35). As we shall see, this causes an undulation of the gain change near $\tau_2$, that in literature has been referred to as a delay of CH [84, 122]. Pump-probe measurements on smaller QDs carried out by Borri et al [115, 116] and Poel et al [57, 149] also reveal a bi-exponential response (ignoring refilling of N) , of the type $h = B_0 + B_1 \exp(t/\tau_1) + B_2 \exp(t/\tau_2)$, however the origin of the two time scales is slightly different. Here, the depleted QD states are initially refilled through phonon mediate carrier relaxation from higher states [57], corresponding to SHB. Subsequently, the QDs are refilled via capture from

the wetting layer with a typical relaxation time of $\sim 4...5$ ps [57, 115, 116, 149], approximately ten times slower than typically measured CH [61, 85, 153]. More importantly, the two responses are not coupled as is the case for equation (6.7), and it is easily verified, that a response of this type does not lead to undulations.

Considering the measured differential transmission in figure 6.7, it is noted that only for $\lambda = 1480$ nm is the medium (slightly) absorbing. I.e. the differential transmission is positive at large times. Furthermore, besides the decrease of the differential transmission near 0 ps, due to SHB and TPA, we observe an undulation shortly after ($\sim 0.5$ ps) for $\lambda = 1520$ nm...1618 nm. This is a good indication of CH processes that are suppressed during the initial carrier-carrier scattering time $\tau_2$, confirming the choice of response function. An example of this is illustrated in figure 6.8, where separate contributions to the gain dynamics are plotted using parameters from fitting the probe transmission for $\lambda = 1580$ nm of figure 6.7. From figure 6.8, it seen seen that the observed
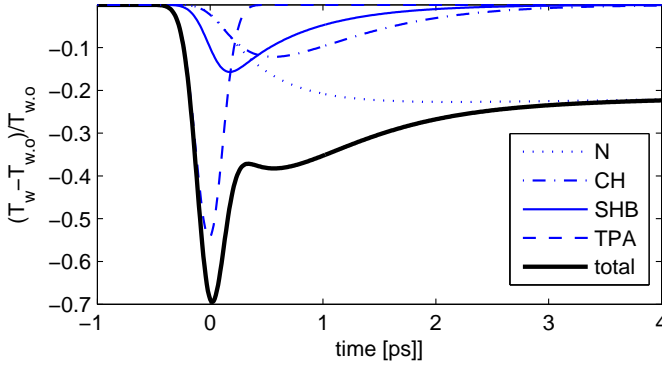


**Figure 6.8:** Example of the seperate contribution to the gain dynamics using parameters fitted to the measured differential transmission at $\lambda = 1580$ nm, cf. figure 6.7.

sharp dip at 0 ps, is mainly caused by 2-photon absorption, while the delayed gain change from CH and changes in $N$ causes the observed undulation close to 0 ps.

Figure 6.9 shows the extracted constants as a function of wavelength. The amplitudes are normalised by $\sqrt{A_N^2 + A_1^2 + A_2^2 + A_{TPA}^2}$. The relaxation time constants are seen to be on the order $\tau_2 \sim 1$ ps and $\tau_2 \sim 0.2$ ps, in good agreement with earlier reported values of similar QDs emitting near 1.5 $\mu$m [93, 94]. We note, that the presented measurements were measured over a delay range of 20 ps, and extracting a time constant, $\tau_N$, related to the recovery of the total carrier density was associated with great uncertainty, but was found in the range $60$ ps $- 100$ ps. Thus, for the parameters presented in figure 6.9, we used $\exp(-t/\tau_N) \approx 0$, while only fitting the data up to 10 ps delay.

From the amplitude of the carrier heating contribution, plotted in figure 6.9b, it is noticed that $A_N$ has its minimum around $\lambda = 1520...1550$ nm corresponding to the largest values of $g_0|\partial_N g|_{\omega_0}|$ (see equation (6.8a)). Also,

(a)                                    (b)

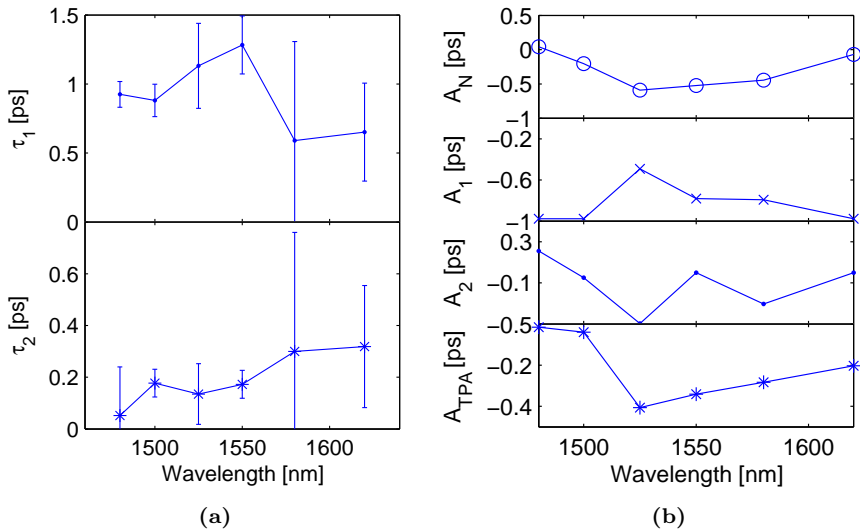**Figure 6.9:** (left): Extracted decay constants as a function of laser wavelength from a tri-exponential fit . The time constants $\tau_1$ and $\tau_2$ are related to the recovery of CH and SHB, respectively (see discussion below). (right) Amplitude coefficients $A_N, A_1, A_2$ and $A_{TPA}$ of the response function (6.7) related to the recovery of the total carrier density, CH, SHB and TPA, respectively

$|A_{TPA}|$ is seen to be the largest at the same wavelengths. Since this is also the spectral region showing the largest gain (see figure 6.6b), we expect that the gradual amplification of the pump through the wave guide leads to a larger TPA contribution.

As mentioned, earlier measurements, using InAs/InGaAs QDs operating near 1200 nm, performed by Borri et al [115, 116] and Poel et al. [57, 149], report on intermediate decay constants of $\tau_1 \sim 4 - 5$ ps, and was attributed carrier refilling of the QDs from the wetting layer. For our sample, the undulation near 0 ps is a strong indication that CH is the main contribution to the intermediate relaxation time and is further supported by the shorter relaxation time $\tau_1 \sim 1$ ps. We attribute this to the large QD size that to some extend is described by a continuum of states, with a carrier occupation determined by a quasi Fermi distribution. We note though, that the CH relaxation time has earlier been found to be in the range $0.5 \ldots 1$ ps in bulk and QWs [85, 153]. Although our fitted relaxation times are associated with large uncertainties, the general trend of $\tau_1$ seems larger than 0.5 ps, and could be a fingerprint of (weakly) quantised states where both thermal relaxation and refilling from the wetting layer play a role.

The extracted time constants shown in figure 6.9a, are associated with large uncertainties. This is mainly attributed to the noisy data caused by the laser that was affected by large amplitude fluctuations. But also the resulting fits show clear deviations from the measurements. This indicates that effects, other than those included in the response function, may contribute to the gain dynamics. An example of this is seen i figure 6.10, showing a zoom in of the differential transmission at $\lambda = 1550$ nm together with its corresponding fit. It is seen that for delay times $t < 0$, the transmission decreases at a slower rate than suggested by the fit, and was observed for all measurements. This can be rectified by increasing the FWHM of the simulated pulse envelope (to values much larger than what was observed in the lab), however, this also smears out the sharp dip near 0 ps as well as the undulation at $\sim 0.2$ ps that is clearly resolved in the measurements. Instead we suggest that the broadened feature could be caused as a result of TPA or GVD that both tends to broaden the pulse. Especially the latter is expected to be significant due the rather long length of the waveguide (3 mm). It is also noted that the sharp feature of the undulation is not fully reproduced in the fit. It has earlier been shown, that gain dispersion in combination with refractive index nonlinearities lead to an enhanced undulation in the measured transmission [122]. It can be shown, that the magnitude of this "spectral artifact" relative to the transmission when ignoring gain dispersion is given as [122]:

$$\eta \approx \alpha \frac{\partial_\omega \xi_0 L}{4\tau_p} \left( 1 - \frac{1}{6}\xi_0 L \right) + O((\xi_0 L)^2), \tag{6.9}$$

where $\alpha$ is the linewidth enhancement factor [62, 154]. Based on the gain measurements shown in figure 6.6b, the influence of gain dispersion was estimated for the three currents 65 mA, 100 mA and 290 mA, using a spline interpolation to extract the slope. The calculated values of $\eta$ relative to the linewidth enhancement factor is seen plotted in figure 6.11. From the plot it is seen
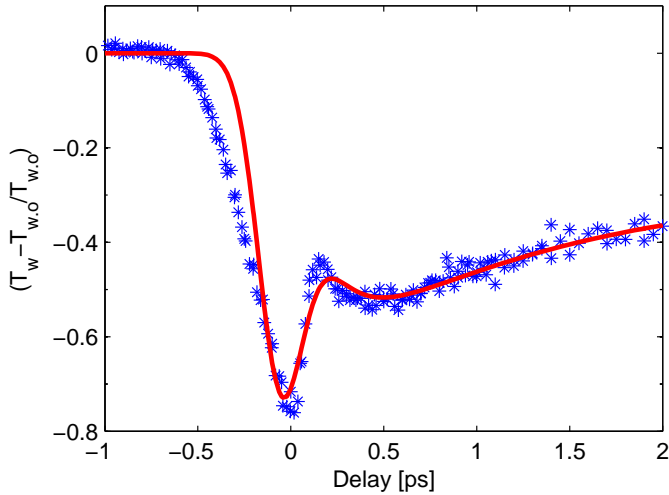
**Figure 6.10:** Zoom in of the measured differential transmission for $\lambda = 1550$ nm together with its corresponding fit. Clear deviations between the two curves are seen. Especially for negative probe delays, is the deviation between data and fit clear, but also the undulation near $t = 0.2$ ps is seen more pronounced than what is captured by the fit.
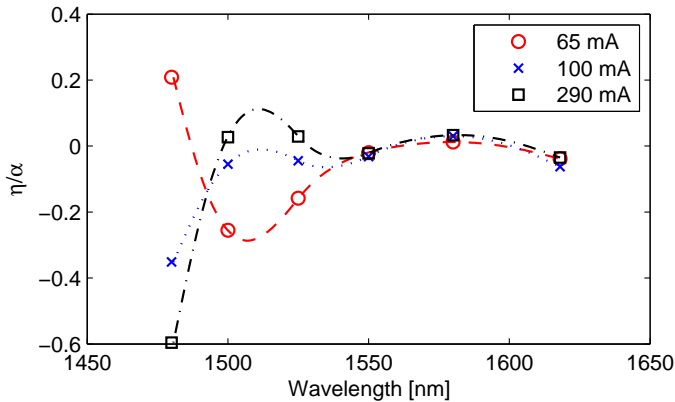


**Figure 6.11:** Estimated magnitude of the transmission change including gain dispersion relative to the transmission change without gain dispersion. Calculations are based on equation (6.9) [122] and the measured gain plotted in6.6b. The gain dispersion were extractedvusing a spline interpolation of the data points.

that from approximately 1550 nm . . . 1620 nm, the influence of gain dispersion is expected to be smallest, whereas at short wavelengths the effect is largest. Measurements performed at 1480 nm for various currents (see appendix B.2), however, did not show such an enhancement of the undulation.

### 6.4.3 Temporal gain dynamics versus carrier injection

Pump-probe measurements with a fixed wavelength were carried out for various currents. The differential transmission for $\lambda = 1620$ nm are plotted in figure 6.12 for various currents scaled by the transparency current $I_{tr} = 13.7$ mA. The solid lines represents bi-expontial fits with parameters plotted in figure 6.13.

From figure 6.12 it is seen that undulations only occur for the highest applied currents. Comparing with the fitted amplitude of CH $A_1$, plotted in figure 6.13b, it is seen that CH decreases for decreasing current. This is in good agreement with the expression for $A_1$ in equation (6.8b) since it is proportional to $g_0$. Thus, only for the strongest currents is CH strong enough to show the undulation.

From figure 6.13a we find relaxation time constants of approximately $\tau_1 \sim$ 1 ps and $\tau_2 \sim 0.2$ ps. Similar to the measurements in the previous section, the extracted decay times are subject to great uncertainty. Especially the values of $\tau_2$ are prone by large errors since it is at the edge of our temporal resolution, i.e. close to the pulse width. Considering $\tau_1$, it seems that for $I/I_{tr} > 2$, $\tau_1$ shows an increasing trend with increasing current. This could be caused by an increasing free carrier absorption that is more dominant for large carrier densities. It has earlier been demonstrated that heating due to free carrier absorption shows a longer relaxation time compared to heating associated with stimulated emmission [155]. Estimates close to the transparency current are associated with large errors, since most of the features are attributed TPA. Nevertheless $\tau_1$ seems larger ($\sim 1.5$ ps) near $I/I_{tr} = 1$. At transparency no net stimulated emission is generated and therefor only heating from TPA and free carrier absorption is expected therfor giving a longer relaxation time.

From the amplitudes $A_N$, $A_1$, $A_2$ and $A_{TPA}$, plotted in figure 6.13b, it is seen that $A_1 > 0$ for $I/I_{tr} < 1$, indicating carrier cooling. Furthermore, it is noticed that $A_{TPA}$ increase with current, but saturates at the highest currents. This is attributed the amplification of the pump pulse. I.e. for large currents, the pump pulse is significantly amplified through the waveguide, leading to an increased TPA. Increasing the current further leads to saturation of the gain, that in turn causes $A_{TPA}$ to converge towards a constant level.
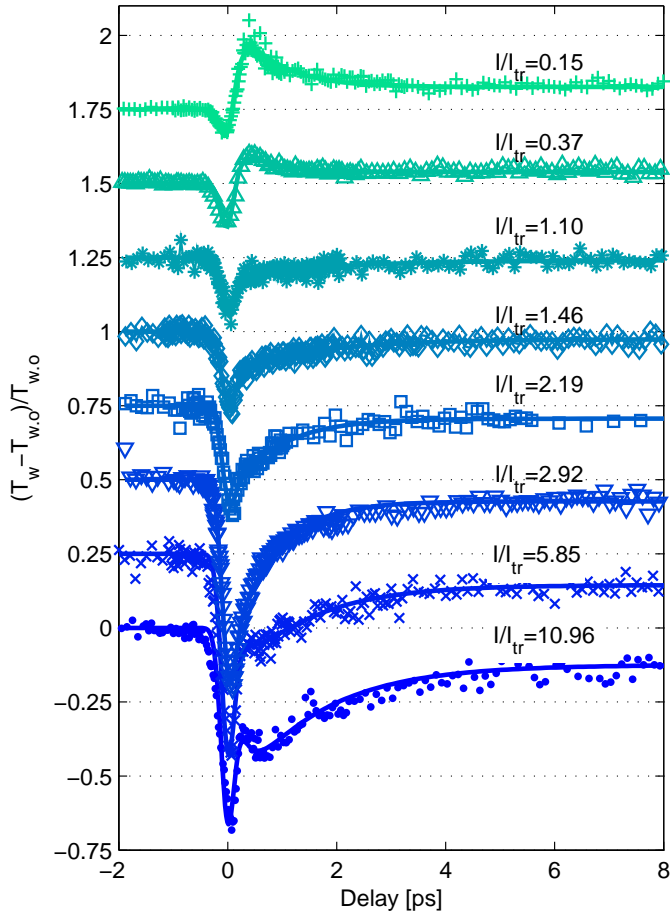
**Figure 6.12:** Differential transmission measurements for various currents relative to the transparency current ($I_{tr} = 13.7$ mA). Laser wavelength was fixed at 1620 nm. Each plot is translated for clarity. Solid lines represents bi-exponential fits of the first 10 ps probe delay using the response function (6.7).
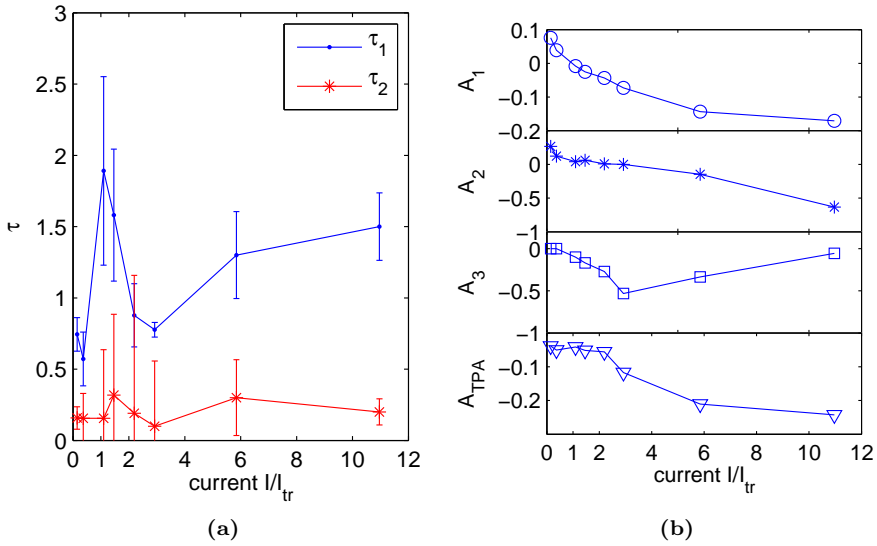
**Figure 6.13:** (left): Extracted decay constants as a function of current from a bi-exponential fit, cf. equation 6.7 . The current is shown relative to the transparency current. Time constants $\tau_1$ and $\tau_2$ are related to the recovery of the total carrier density, CH and SHB, respectively (see discussion above). (right) Amplitude coefficients $A_N, A_1, A_2$ and $A_{TPA}$ of the response function 6.7 associated with the recovery of the total carrier density, CH, SHB and TPA, respectively

# 6.5 Conclusion

Measurements of the ultra fast gain dynamics of a QD based SOA operating near 1.5 $\mu$m were analysed and discussed.

ASE spectra showed a mean photon energy that smoothly increased with increasing current, indicating that the QDs possessed several quantum states. The transparency current was measured for six different wavelengths showing that the transparency current decrease with wavelength. This observation further points to large QDs consisting of multiple states.

Pump-probe measurements using $\sim$ 180 fs pulses were carried out for different wavelengths with a fixed wavelength showing two characteristic decay times of $\sim$ 0.2 ps and 1 ps. The former was attributed SHB while the latter was attributed heating of the carrier ensemble. This was also confirmed from an observed undulation of the transmission near 0 delay.

Finally, pump-probe measurement for various applied currents were carried out at 1620 nm, showing a increasing CH relaxation time with increasing current while the measured SHB relaxation time was limited by the pulse width giving a fairly constant value of $\sim$ 0.2 ps. For the highest currents, clear sign of carrier heating was observed with notable undulation of the transmission near 0 delay. A the smallest currents, carrier cooling was observed.

# CHAPTER 7

# Summary and outlook

## 7.1 Summary

The work in this thesis concerned the propagation of light in semiconductor waveguide structures with emphasis on methods for achieving controllable signal delays. Measurements of pulse delay measurements in quantum well structures, based on a simple principle of pulse shaping by gain saturation, where carried out and presented in chapter 4 . A more sophisticated method of slowing the propagation of light in waveguide structures, using electromagnetically induced transparency, was theoretically investigated in chapter 5. Finally, the ultra fast carrier dynamics of a quantum dot semiconductor optical amplifier was experimentally investigated in chapter 6.

**Pulse delay by gain saturation**

Simultaneous transmission and pulse delay measurements of 180 fs FWHM were presented for two QW waveguide devices. The first was a standard SOA structure that allowed for an applied electric bias across the entire waveguide. The second device consisted of a single waveguide with separately contacted sections of the waveguide allowing for individually applied voltages on three separate parts of the waveguide. For these measurements, the first and last section was operated at a forward bias, rendering them amplifying, whereas the middle section was rendered absorbing by a reverse bias. The two type of devices were referred to as the single sectioned and cascaded devices, respectively. In a series of experiments, the pulse delay and transmission were measured as a function of input pulse energy for various applied bias levels.

The single sectioned device showed slight pulse advancement in the amplifying regime and pronounced delays in the absorbing regime with a maximum delay of 90 fs corresponding to 0.5 of the FWHM pulse width. The maximum delay was furthermore associated with a pulse attenuation of 10 dB. At pulse

energies $> 10$ pJ, pulse advancement was measured both in the amplifying as well as in the absorbing regime. Comparing with simulated pulse propagation calculations, using a simple model derived in chapter 2, reasonably good fits of the transmission were achieved, however, the calculations did not give rise to a pulse advancement as was experimentally observed.

The cascaded device was measured with a fixed current density on both amplifying sections and for various reverse bias of the absorbing section. For this device, it was demonstrated possible to achieve net delay of $\sim 70$ fs, with a net transmission of unity. Also for this device, a pulse advancement was observed at high input pulse energies for all applied bias levels. In this regime the transmission was similar for all measured bias levels due to the domination TPA. As a result an electrically controlled net pulse shift of more than 100 fs was demonstrated without significant change of the transmission.

The observed pulse advancement at high pulse energies was investigated and discussed. Propagation simulations using a more rigourous model based on rate equations including ultra fast carrier relaxation mechanisms such as TPA, CH and SHB, was presented. However the simulations were unable to explain the observed pulse advancement. Calculations, taking into account refractive index nonlinearities in the background material combined with gain dispersion, were discussed. Although these results did not point towards the observed pulse advancement, they indicated the importance of including index nonlinearities and gain dispersion at high field intensities.

## Slow light in quantum dots by EIT

In chapter 5 theoretical calculations of the slowdown factor in a quantum dot medium using EIT were presented. It was shown that EIT in quantum dots is only feasible at cryogenic temperatures due to the strong dephasing at room temperatures.

Also, inhomogeneous broadening was demonstrated to have an adverse effect on EIT. To address the latter issue, three schemes, $\Xi$, V and $\Lambda$, were compared. The results showed a clear difference of the V-scheme compared to the $\Xi$- and $\Lambda$-scheme. Where the V-scheme showed a slowdown factor of more than $10^3$, almost no slowdown effect was observed in the other schemes. This difference stems from two properties special to the V scheme: Firstly, the coupling field drives carriers on the coupling transition. Thus far off-resonant QDs does not contribute with probe absorption via the secondary resonance. Secondly, the two-photon resonance condition has a negative slope between the inhomogeneous spectral shift and probe detuning. This prevents absorption of the probe via the two-photon absorption path from off-resonant QDs.

Propagation calculations of the probe were presented for the three schemes. Despite the fact that the coupling field is subject to absorption in the V scheme, the achievable delay was demonstrated far superior compared to the other schemes. For a fixed transmission of $-10$ dB, the V scheme showed a maximum delay of approximately 0.8 ns for a device length of 1 mm. For device lengths longer than 1 mm the delay was approximately constant.

**Pump-probe measurements on a quantum dot SOA**

In chapter 6 measurements of the ultra fast gain dynamics of a QD SOA were presented based on degenerate pump-probe spectroscopy.

Amplified spontaneous emission spectra and small signal gain measurements at various wavelengths suggested QDs possessing many quantised states.

Pump-probe measurements were carried out in the linear regime, at six different wavelengths, with a fixed applied current of 100 mA. Two characteristic relaxation times of $\sim 0.2$ ps and $\sim 1$ ps were extracted using a response function typically used for bulk and QW media. The former was attributed SHB, while the latter was attributed heating of the carriers. The heating effect was furthermore confirmed by an observed undulation near $\sim 0.2$ ps, confirming that the QDs consists of many quantised states with a Fermi-Dirac like occupation probability.

Pump-probe measurements for various applied currents, at a fixed wavelength of 1620 nm, were presented. Apart from currents near the transparency current, the CH relaxation time was found to increase with increasing current, and was tentatively suggested being due to the increased free carrier absorption at high currents. At the lowest applied currents, the extracted amplitude of CH suggests carrier cooling induced by the pump. The measured SHB relaxation time was limited by our pulse width, showing a close to constant value of $\sim 0.2$ ps.

# 7.2 Outlook

Several issues related to the work presented in this thesis are left unanswered and could be pursued in future work.

**Pulse delay by gain saturation**

The cascaded device proved capable of delaying a pulse without attenuating, however the obtained delay was modest. For this work, the current density was fixed on both SOA sections, thus, much of the parameter space are left unexplored. Also the number of EA and SOA section could be further investigated. Increasing the number of SOA and EA sections by making the waveguide long, would most likely imply large group velocity dispersion. However, the effect of using several EA and SOA sections, while keeping the same ratio between the total SOA and EA length constant could be further examined.

The observed pulse advancement at high pulse energies is currently not understood, but is believed to be related with refractive index nonlinearities in combination with gain dispersion, that become increasingly important at high intensities. To investigate this experimentally, similar experiments could be carried out changing the pulse duration as well as the pulse chirp. Fur-

thermore, the influence of gain dispersion could be examined by investigating the wavelength dependence. Also pump-probe measurements, comparing the phase and transmission change, could provide usefull insight to the underlying physical mechanisms. A theoretical model furthermore needs to be developed that include refractive index nonlinearities, while being valid in the nonlinear gain regime.

### Slow light in quantum dots by EIT

The theoretical calculations of the V-scheme show promising results and an experimental implementation are currently being investigated. This requires QDs with a low intra-band relaxation rate similar to the ones observed in [95, 156]. Furthermore, a coupling laser, with a wavelength suitable for the specific quantum dots, needs to be implemented in the current setup. Finally a cryostat that allows for transmission measurements is required and is currently being installed into the setup.

### Pump-probe measurements on a quantum dot SOA

The pump-probe setup is a practical tool for analysing the carrier dynamics in waveguide structures. In relation to future experiments on EIT or pulse delay by gain saturation, this may provide a useful insight of the relevant relaxation mechanisms.

The pump-probe measurements, presented in chapter 6, were unfortunately subject to much noise, that made it difficult to extract consistent relaxation times. This was mainly caused by laser fluctuations. A problem that has turned out being related to a faulty Verdi pump laser, and is currently being fixed. But also the rather long device (3 mm), made measurements difficult in the absorption regime, and often required long integration times and pulse energies at the edge of the linear regime. Thus, future characterisations of QD SOAs should preferably be performed on shorter devices.

# APPENDIX A

# Deriving the 3-level density matrix

The density rate equations for a standard three level scheme are used to calculate the polarisation and absorption as a function of the laser detuning. Based on figure 5.1 we define the laser detunings as:

$$\Delta_p \equiv \omega_p - \omega_{12} \qquad \text{and} \qquad \Delta_c \equiv \omega_c - \omega_{23}, \tag{A.1}$$

where $\omega_{ij}$ is the (positive) frequency difference between state i and j and $\omega_p$ ($\omega_c$) is frequency of the probe (coupling) laser. The Rabi frequencies are defined as

$$\Omega_p = \frac{\mu_{12} E_p(\mathbf{r})}{\hbar} \qquad \Omega_c = \frac{\mu_{23} E_c(\mathbf{r})}{\hbar}, \tag{A.2}$$

where $\mu_{ij}$ is the dipole moment of the corresponding transition $|i\rangle \to |j\rangle$. As in section 2.2, decay is added to the rate equations phenomenologically denoting $\Gamma_{ij}$ and $\gamma_{ij}$ is the population decay rate and homogeneous linewidth of the transition between $|i\rangle \leftrightarrow |j\rangle$. We note that for the case of population decay rate, $\Gamma_{ij}$, the direction of decay is not explicitly noted, i.e. $\Gamma_{ij} \equiv \Gamma_{ji}$.

## A.1 Hamiltonian

The Hamiltonian is derived analogous to a two-level system derived in section 2.2. I.e. using the dipole approximation as well as the slowly varying wave approximation. In the interaction picture the Hamiltonian of the three schems takes the form:

$$\Xi: \qquad \hat{H}_1^{int} = \hbar \left( e^{-i\Delta_p t} \Omega_p |2\rangle\langle 1| + e^{-i\Delta_c t} \Omega_c |3\rangle\langle 2| + h.c. \right) \tag{A.3}$$

$$\text{V}: \qquad \hat{H}_1^{int} = \hbar \left( e^{-i\Delta_p t} \Omega_p |1\rangle\langle 2| + e^{-i\Delta_c t} \Omega_c |3\rangle\langle 2| + h.c. \right) \tag{A.4}$$

$$\Lambda: \qquad \hat{H}_1^{int} = \hbar \left( e^{-i\Delta_p t} \Omega_p |2\rangle\langle 1| + e^{-i\Delta_c t} \Omega_c |2\rangle\langle 3| + h.c. \right) \tag{A.5}$$

## A.2  V scheme

The homogeneous linewidth consist of terms from the population decay rate as well as from pure dephasing. For the V-scheme this is modelled as.

$$\gamma_{12} \quad = \quad \gamma_{12}^{(pd)} + \frac{1}{2}\left(\Gamma_{13} + \Gamma_{23} + \Gamma_{12}\right) \tag{A.6}$$

$$\gamma_{13} \quad = \quad \gamma_{13}^{(pd)} + \frac{1}{2}\Gamma_{13} \tag{A.7}$$

$$\gamma_{23} \quad = \quad \gamma_{23}^{(pd)} + \frac{1}{2}\Gamma_{23} \tag{A.8}$$

The density rate equation is derived similarly to section 2.2

$$\partial_t \rho_{11} \quad = \quad -\Gamma_{12}\rho_{11} + \Gamma_{13}\rho_{33} + i\frac{\Omega_p}{2}\left(\tilde{\rho}_{21} - \tilde{\rho}_{12}\right) \tag{A.9}$$

$$\partial_t \rho_{22} \quad = \quad \Gamma_{12}\rho_{11} + \Gamma_{23}\rho_{33} + i\frac{\Omega_p}{2}\left(\tilde{\rho}_{12} - \tilde{\rho}_{21}\right) + i\frac{\Omega_c}{2}\left(\tilde{\rho}_{32} - \tilde{\rho}_{23}\right) \tag{A.10}$$

$$\partial_t \tilde{\rho}_{12} \quad = \quad i\frac{\Omega_p}{2}\left(\rho_{22} - \rho_{11}\right) + (i\Delta_p - \gamma_{12})\tilde{\rho}_{12} - i\frac{\Omega_c}{2}\tilde{\rho}_{13} \tag{A.11}$$

$$\partial_t \tilde{\rho}_{13} \quad = \quad -i\frac{\Omega_c}{2}\tilde{\rho}_{12} + \left(i(\Delta_p - \Delta_c) - \gamma_{13}\right)\tilde{\rho}_{13} + i\frac{\Omega_p}{2}\tilde{\rho}_{23} \tag{A.12}$$

$$\partial_t \tilde{\rho}_{23} \quad = \quad i\frac{\Omega_c}{2}\left(\rho_{33} - \rho_{22}\right) + i\frac{\Omega_p}{2}\tilde{\rho}_{13} - (i\Delta_c + \gamma_{23})\tilde{\rho}_{23} \tag{A.13}$$

$$1 \quad = \quad \rho_{11} + \rho_{22} + \rho_{33}\,. \tag{A.14}$$

For the case of the two other schemes, the equations are similar, only the sign of $\Delta_p$ and $\Delta_c$ are changed according to the relative energy difference of the levels and the decay terms are changed in accordance with the correspondence decay channels. For consistency though, we present the equations for the two other schemes.

### A.2.1  Ξ scheme

The honogeneous linewidths are given as

$$\gamma_{13} \quad = \quad \gamma_{13}^{(pd)} + \frac{1}{2}\left(\Gamma_{23} + \Gamma_{13}\right) \tag{A.15}$$

$$\gamma_{12} \quad = \quad \gamma_{12}^{(pd)} + \frac{1}{2}\Gamma_{12} \tag{A.16}$$

$$\gamma_{23} \quad = \quad \gamma_{23}^{(pd)} + \frac{1}{2}\left(\Gamma_{23} + \Gamma_{12} + \Gamma_{13}\right) \tag{A.17}$$

The density matrix equations becomes:

$$\partial_t \rho_{11} = \Gamma_{12}\rho_{22} + \Gamma_{13}\rho_{33} + i\frac{\Omega_p}{2}\left(\tilde{\rho}_{21} - \tilde{\rho}_{12}\right) \tag{A.18}$$

$$\partial_t \rho_{22} = \Gamma_{23}\rho_{33} - \Gamma_{12}\rho_{22} + i\frac{\Omega_c}{2}\left(\tilde{\rho}_{32} - \tilde{\rho}_{23}\right) + i\frac{\Omega_p}{2}\left(\tilde{\rho}_{12} - \tilde{\rho}_{21}\right) \tag{A.19}$$

$$\partial_t \tilde{\rho}_{12} = i\frac{\Omega_p}{2}\left(\rho_{22} - \rho_{11}\right) - i\frac{\Omega_c}{2}\tilde{\rho}_{13} - \left(i\Delta_p + \gamma_{12}\right)\tilde{\rho}_{12} \tag{A.20}$$

$$\partial_t \tilde{\rho}_{13} = i\frac{\Omega_p}{2}\tilde{\rho}_{23} - \left(i(\Delta_p + \Delta_c) + \gamma_{13}\right)\tilde{\rho}_{13} - i\frac{\Omega_c}{2}\tilde{\rho}_{12} \tag{A.21}$$

$$\partial_t \tilde{\rho}_{23} = i\frac{\Omega_c}{2}\left(\rho_{33} - \rho_{22}\right) - \left(i\Delta_c + \gamma_{23}\right)\tilde{\rho}_{23} + i\frac{\Omega_p}{2}\tilde{\rho}_{13} \tag{A.22}$$

$$1 = \rho_{11} + \rho_{22} + \rho_{33}. \tag{A.23}$$

### A.2.2 $\Lambda$ scheme

The polarization decay is for the $\Lambda$ scheme, seen in figure **??**(a), related to the population decay as:

$$\gamma_{13} = \gamma_{13}^{(pd)} + \frac{1}{2}\Gamma_{13} \tag{A.24}$$

$$\gamma_{12} = \gamma_{12}^{(pd)} + \frac{1}{2}\left(\Gamma_{12} + \Gamma_{23}\right) \tag{A.25}$$

$$\gamma_{23} = \gamma_{23}^{(pd)} + \frac{1}{2}\left(\Gamma_{12} + \Gamma_{23} + \Gamma_{13}\right) \tag{A.26}$$

The density matrix equations becomes:

$$\partial_t \rho_{11} = \Gamma_{12}\rho_{22} + \Gamma_{13}\rho_{33} + i\frac{\Omega_p}{2}\left(\tilde{\rho}_{21} - \tilde{\rho}_{12}\right) \tag{A.27}$$

$$\partial_t \rho_{22} = -\left(\Gamma_{12} + \Gamma_{23}\right)\rho_{22} + i\frac{\Omega_p}{2}\left(\tilde{\rho}_{13} - \tilde{\rho}_{31}\right) + i\frac{\Omega_c}{2}\left(\tilde{\rho}_{23} - \tilde{\rho}_{32}\right) \tag{A.28}$$

$$\partial_t \tilde{\rho}_{12} = i\frac{\Omega_p}{2}\left(\rho_{22} - \rho_{11}\right) + \left(i\Delta_p - \gamma_{12}\right)\tilde{\rho}_{12} - i\frac{\Omega_c}{2}\tilde{\rho}_{13} \tag{A.29}$$

$$\partial_t \tilde{\rho}_{13} = -i\frac{\Omega_c}{2}\tilde{\rho}_{12} + \left(i(\Delta_p - \Delta_c) - \gamma_{13}\right)\tilde{\rho}_{13} + i\frac{\Omega_p}{2}\tilde{\rho}_{23} \tag{A.30}$$

$$\partial_t \tilde{\rho}_{23} = i\frac{\Omega_c}{2}\left(\rho_{33} - \rho_{22}\right) + i\frac{\Omega_p}{2}\tilde{\rho}_{13} - \left(i\Delta_c + \gamma_{23}\right)\tilde{\rho}_{23} \tag{A.31}$$

$$1 = \rho_{11} + \rho_{22} + \rho_{33}. \tag{A.32}$$

# APPENDIX B

# Pump-probe measurements

## B.1 Phase change at 1620 nm

For the pump-probe measurements presented in chapter 6, the change of phase was simultaneously measured. The change of carriers in a semiconductor material gives rise to a change of the refractive index that is detected as a change of the optical phase. This effect is often in literature quantified by the linewidth enhancement factor [123] since it gives rise to a broader linewidth than what was predicted by Schawlow and Townes [62]. The linewidth enhancement factor is defined as [154]:

$$\alpha = \frac{\frac{\partial \chi'}{\partial N}}{\frac{\partial \chi''}{\partial N}} \approx -\frac{2}{L}\frac{\Delta \phi}{\Delta g},\tag{B.1}$$

where $\Delta \phi$ and $\Delta g$ is the pump induced phase and gain change. From equation (B.1) it is noted, that the response function of $\Delta g$ and $\Delta \phi$ should be of the same type. Thus, similar to chapter 6, we use a bi-exponential response function convoluted with the autocorrelation of the pulse (see equation (6.5)) to fit the phase dynamics. The results are plotted in figure B.1. The extracted fit parameters where in reasonable agreement with the parameters extracted from the transmission, although with a tendency of slightly larger estimates on $\tau_1$ being closer to 1.5 ps compared to 1 ps in transmission measurements.
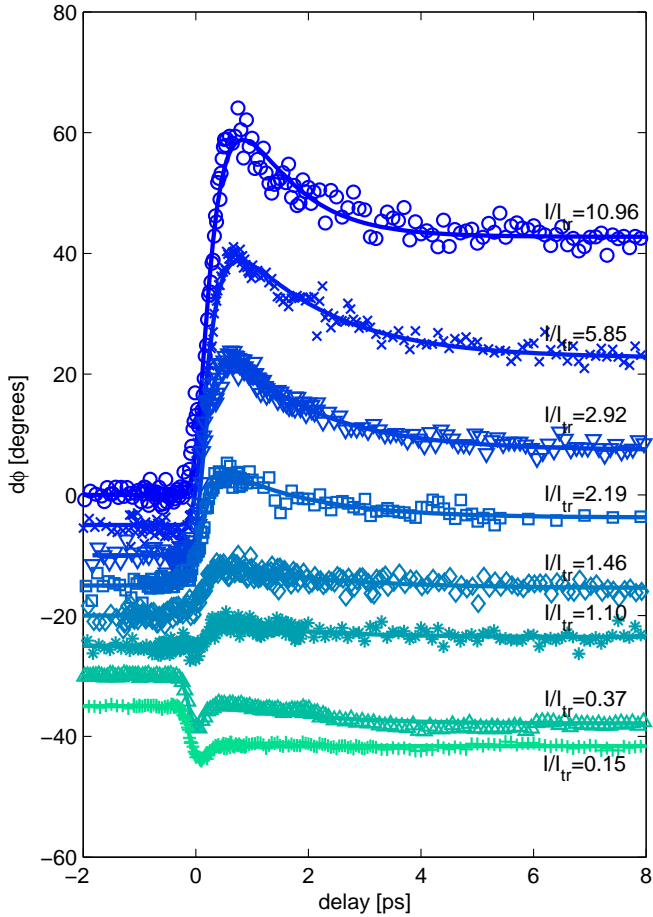
**Figure B.1:** Phase change measurements for various currents relative to the transparency current ($I_{tr} = 13.7$ mA). Laser wavelength was fixed at 1620 nm. Each plot is translated for clarity. Solid lines represents bi-exponential fits of the first 10 ps probe delay using the response function (6.7).

## B.2 Pump-probe measurements at 1480 nm

In section 6.4.2, it was discussed whether the observed undulation arise due to a coupling between phase changes and gain changes, and was referred to as a spectral artifact [122]. The estimated magnitude of the spectral artifact is plotted in figure 6.11 and shows that the contribution from spectral artifacts in the differential transmission should be largest at the shortest wavelengths.

Pump-probe measurements similar to those presented in section 6.4.3 were carried out at 1480 nm. The corresponding differential transmission and phase change are plotted in figure B.2 and B.3, respectively for various current normalised by the transparency curren $I_{tr} = 108.3$ mA. Based on figure B.2, no clear indication of an increased undulation is observed, which leads us to believe that the observed undulation is mainly due to the direct contribution from CH.
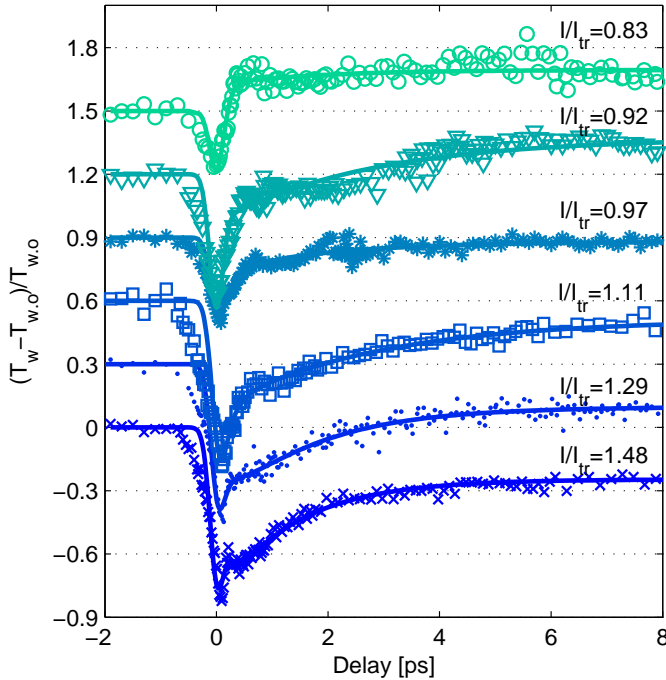


**Figure B.2:** Phase change measurements for various currents relative to the transparency current ($I_{tr} = 108.3$ mA). Laser wavelength was fixed at 1480 nm. Each plot is translated for clarity. Solid lines represents bi-exponential fits of the first 10 ps probe delay using the response function (6.7).

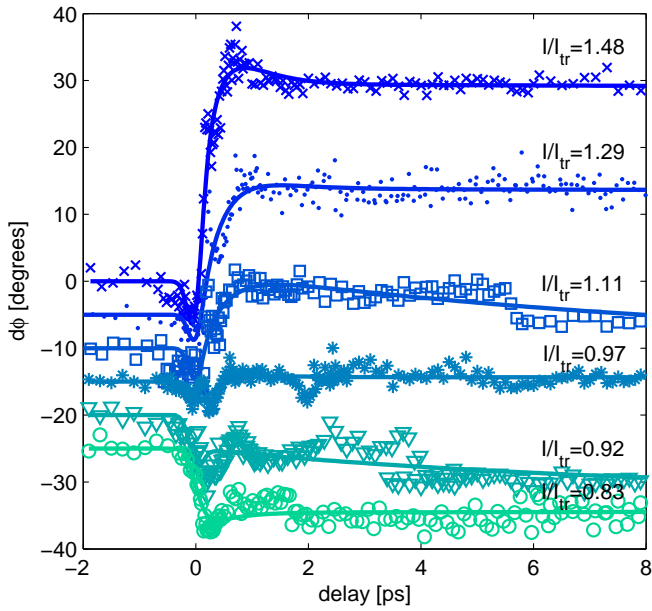Solid lines represents fits based on a bi-expontial response function (see

**Figure B.3:** Phase change measurements for various currents relative to the transparency current ($I_{tr}$ = 108.3 mA). Laser wavelength was fixed at 1480 nm. Each plot is translated for clarity. Solid lines represents bi-exponential fits of the first 10 ps probe delay using the response function (6.7).

equation (6.7)). The measurements at this wavelength are more noisy compared to the measurements at 1620 nm as a result of increased absorption in the absorbing regime, and an increase of ASE in the gain regime. Thus, the fitted parameters where associated with great uncertainty for the low currents and are therefore not shown. The extracted relaxation time constants for the three largest currents, are plotted in figure B.4, and shows approximate values of $\tau_2 \sim 0.15$ ps, while $\tau_1$ is in the range between $1 \ldots 3$ ps with a decreasing tendency with current.
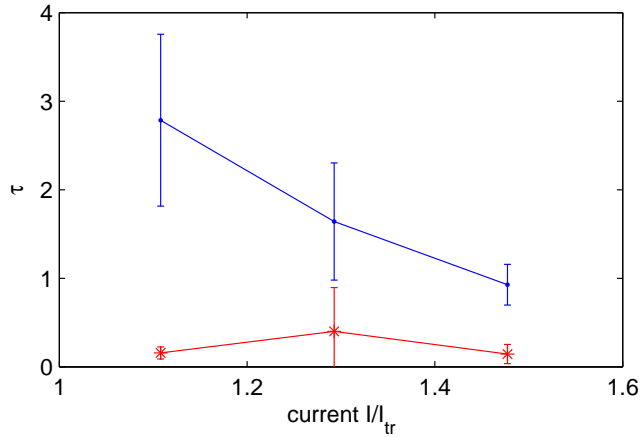


**Figure B.4:** Phase change measurements for various currents relative to the transparency current ($I_{tr} = 108.3$ mA). Laser wavelength was fixed at 1480 nm. Each plot is translated for clarity. Solid lines represents bi-exponential fits of the first 10 ps probe delay using the response function (6.7).

# Bibliography

[1] P. W. Milonni, *Fast Light, Slow Light and Left-Handed Light* (Institute of Physics Publishing, Bristol, UK, 2005).

[2] E. Hecht, *Optics* (Addison Wesley, San Francisco, USA, 2002), 4th ed.

[3] J. D. Jackson, *Classical Electrodynamics* (John Wiley & Sons, New York, 1998), 3rd ed.

[4] M. Born and E. Wolf, *Principles of Optics* (Camebridge University Press, Cambridge, UK, 1999), 7th ed.

[5] R. W. Boyd, *Nonlinear Optics, Third Edition* (Academic Press, 2008), 3rd ed., ISBN 0123694701.

[6] J. S. Toll, Phys. Rev. **104**, 1760 (1956).

[7] C. G. B. Garrett and D. E. McCumber, Phys. Rev. A **1**, 305 (1970).

[8] P. Meystre and M. Sargent, *Elements of quantum optics* (Springer, 2007).

[9] M. O. Scully and M. S. Zubairy, *Quantum Optics* (Cambridge University Press, Cambridge, 1997).

[10] L. Brillouin, *Wave propagation and group velocity* (Academic Press, 1964).

[11] S. Chu and S. Wong, Phys. Rev. Lett. **48**, 738 (1982).

[12] L. J. Wang, A. Kuzmich, and A. Dogariu, Nature **407**, 277 (2000).

[13] A. M. Steinberg, P. G. Kwiat, and R. Y. Chiao, Phys. Rev. Lett. **71**, 708 (1993).

[14] M. S. Bigelow, N. N. Lepeshkin, and R. W. Boyd, Science **301**, 200 (2003).

[15] G. M. Gehring, A. Schweinsberg, C. Barsi, N. Kostinski, and R. W. Boyd, Science **312**, 895 (2006).

[16] J. B. Khurgin and R. S. Tucker, *Slow light -Science and Applications* (Taylor & Francis Group, Boca Raton, USA, 2009).

[17] T. Baba, Nature Photonics **2**, 465 (2008), ISSN 1749-4885.

[18] T. F. Krauss, Journal of Physics D: Applied Physics **40**, 2666 (2007).

[19] J. D. Joannopoulos, S. G. Johnson, J. N. Winn, and R. D. Meade, *PhotonicCrystals, Molding the Flow of Light* (Princeton University Press, 2008), 2nd ed.

[20] L. H. Frandsen, A. V. Lavrinenko, J. Fage-Pedersen, and P. I. Borel, Opt. Express **14**, 9444 (2006).

[21] D. Mori, S. Kubo, H. Sasaki, and T. Baba, Optics Express **15**, 5264 (2007).

[22] M. Notomi, K. Yamada, A. Shinya, J. Takahashi, C. Takahashi, and I. Yokohama, Phys. Rev. Lett. **87**, 253902 (2001).

[23] Y. A. Vlasov, M. O'Boyle, H. F. Hamann, and S. J. McNab, Nature **438**, 65 (2005).

[24] Y. A. Vlasov and S. J. McNab, Opt. Lett. **31**, 50 (2006).

[25] P. K. Kondratko and S.-L. Chuang, Opt. Express **15**, 9963 (2007).

[26] P.-C. Ku, F. Sedgwick, C. J. Chang-Hasnain, P. Palinginis, T. Li, H. Wang, S.-W. Chang, and S.-L. Chuang, Opt. Lett. **29**, 2291 (2004).

[27] J. Mørk, R. Kjær, M. van der Poel, and K. Yvind, Opt. Express **13**, 8136 (2005).

[28] P. Palinginis, F. Sedgwick, S. Crankshaw, M. Moewe, and C. Chang-Hasnain, Opt. Express **13**, 9909 (2005).

[29] H. Su and S. L. Chuang, Opt. Lett. **31**, 271 (2006).

[30] A. Schweinsberg, N. N. Lepeshkin, M. S. Bigelow, R. W. Boyd, and S. Jarabo, EPL (Europhysics Letters) **73**, 218 (2006).

[31] M. S. Bigelow, N. N. Lepeshkin, and R. W. Boyd, Phys. Rev. Lett. **90**, 113903 (2003).

[32] M. S. Bigelow, N. N. Lepeshkin, and R. W. Boyd, Science **301**, 200 (2003).

[33] J. Mørk, F. Öhman, M. van der Poel, Y. Chen, P. Lunnemann, and K. Yvind, Laser & Photonics Review **3**, 30 (2008).

[34] F. Öhman, K. Yvind, and J. Mørk, Opt. Express **14**, 9955 (2006).

[35] W. Xue, Y. Chen, F. Öhman, and J. Mørk, Opt. Express **17**, 1404 (2009).

[36] W. Xue, Y. Chen, F. Öhman, S. Sales, and J. Mørk, Opt. Lett. **33**, 1084 (2008).

[37] W. Xue, S. Sales, J. Capmany, and J. Mørk, in *Slow and Fast Light* (Optical Society of America, 2009), p. SMB6.

[38] S. E. Harris, J. E. Field, and A. Imamoğlu, Phys. Rev. Lett. **64**, 1107 (1990).

[39] K. J. Boller, A. Imamolu, and S. E. Harris, Phys. Rev. Lett. **66**, 2593 (1991).

[40] L. V. Hau, S. E. Harris, Z. Dutton, and C. H. Behroozi, Nature **397**, 594 (1999).

[41] J. J. Longdell, E. Fraval, M. J. Sellars, and N. B. Manson, Phys. Rev. Lett. **95**, 063601 (2005).

[42] C. Liu, Z. Dutton, C. Behroozi, and L. Hau, Nature **409**, 490 (2001).

[43] D. F. Phillips, A. Fleischhauer, A. Mair, R. L. Walsworth, and M. D. Lukin, Phys. Rev. Lett. **86**, 783 (2001).

[44] M. Bajcsy, A. Zibrov, and M. Lukin, Nature **426**, 638 (2003).

[45] M. Eisaman, A. Andre, F. Massou, M. Fleischhauer, A. Zibrov, and M. Lukin, Nature **438**, 837 (2005).

[46] S. R. G. Naomi S. Ginsberg and L. V. Hau, Nature **445**, 623 (2007).

[47] X. Xu, B. Sun, P. R. Berman, D. G. Steel, A. S. Bracker, D. Gammon, and L. J. Sham, Science **317**, 929 (2007).

[48] G. Jundt, L. Robledo, A. Hogele, S. Falt, and A. Imamoglu, Physical Review Letters **100**, 177401 (pages 4) (2008).

[49] M. C. Phillips and H. Wang, Phys. Rev. B **69**, 115337 (2004).

[50] M. C. Phillips, H. Wang, I. Rumyantsev, N. H. Kwong, R. Takayama, and R. Binder, Phys. Rev. Lett. **91**, 183602 (2003).

[51] A. C. Selden, British Journal of Applied Physics **18**, 743 (1967).

[52] A. C. Selden, Optics and Spectroscopy **106**, 6 (2009).

[53] E. B. Aleksandrov and V. S. Zapasskii, Physics-Uspekhi **49**, 1067 (2006).

[54] M. van der Poel, J. Mørk, and J. Hvam, Opt. Express **13**, 8032 (2005).

[55] F. G. Sedgwick, B. Pesala, J.-Y. Lin, W. S. Ko, X. Zhao, and C. J. Chang-Hasnain, Opt. Express **15**, 747 (2007).

[56] F. G. Sedgwick, B. Pesala, A. V. Uskov, and C. J. Chang-Hasnain, Opt. Express **15**, 17631 (2007).

[57] M. van der Poel and J. M. Hvam, Journal of Materials Science: Materials in Electronics **18** (2007).

[58] C. J. Chang-Hasnain and S. L. Chuang, J. Lightwave Technol. **24**, 4642 (2006).

[59] P. K. Nielsen, H. Thyrrestrup, J. Mørk, and B. Tromborg, Opt. Express **15**, 6396 (2007).

[60] C. Chang-Hasnain, P.-C. Ku, J. Kim, and S.-l. Chuang, in *Proceedings of the IEEE* (2003), vol. 91, pp. 1884–1897, ISSN 0018-9219.

[61] J. Mørk and J. Mark, in *SPIE, Physics and Simulation of Optoelectronic Devices III*, edited by M. Osinski and W. W. Chow (SPIE, 1995), vol. 2399, pp. 146–159.

[62] L. Coldren and S. Corzine, *Diode lasers and photonic integrated circuits*, vol. 36 (John Wiley & Sons, 1997).

[63] J. Mørk and A. Mecozzi, Applied Physics Letters **65**, 1736 (1994).

[64] J. Mørk, A. Mecozzi, and C. Hultgren, Applied Physics Letters **68**, 449 (1996).

[65] A. Dienes, J. P. Heritage, M. Y. Hong, and Y. H. Chang, Opt. Lett. **17**, 1602 (1992).

[66] A. Dienes, J. P. Heritage, C. Jasti, and M. Y. Hong, J. Opt. Soc. Am. B **13**, 725 (1996).

[67] J. Mulet and J. Mørk, Quantum Electronics, IEEE Journal of **42**, 249 (2006), ISSN 0018-9197.

[68] G. P. Agrawal, *Fiber-Optic Communication Systems* (John Wiley & Sons, 2002), 3rd ed.

[69] J. J. Sakurai, *Modern Quantum Mechanics (2nd Edition)* (Addison Wesley, 1994), ISBN 0201539292.

[70] H. Haug and S. W. Koch, *Quantum theory of the optical and electronic properties of semiconductors* (World Scientific Publishing Co. Pte. Ltd., 2004), 4th ed.

[71] K. Henneberger, F. Herzel, S. W. Koch, R. Binder, A. E. Paul, and D. Scott, Phys. Rev. A **45**, 1853 (1992).

[72] D. Birkedal, K. Leosson, and J. M. Hvam, Phys. Rev. Lett. **87**, 227401 (2001).

[73] J. Shah, *Ultrafast spectroscopy of Semiconductors and Semiconductor Nanostructures* (Springer, Berling, Germany, 1999), 2nd ed.

[74] P. Borri, W. Langbein, J. Mørk, J. M. Hvam, F. Heinrichsdorff, M.-H. Mao, and D. Bimberg, Phys. Rev. B **60**, 7784 (1999).

[75] P. Borri, W. Langbein, S. Schneider, U. Woggon, R. L. Sellin, D. Ouyang, and D. Bimberg, IEEE Journal of Selected Topics in Quantum Electronics **8**, 984 (2002).

[76] P. Borri, W. Langbein, S. Schneider, U. Woggon, R. L. Sellin, D. Ouyang, and D. Bimberg, Phys. Rev. Lett. **89**, 187401 (2002).

[77] P. Borri, W. Langbein, S. Schneider, U. Woggon, R. L. Sellin, D. Ouyang, and D. Bimberg, Phys. Rev. Lett. **87**, 157401 (2001).

[78] P. Borri, S. Schneider, W. Langbein, and D. Bimberg, Journal of Optics A: Pure and Applied Optics **8**, S33 (2006).

[79] W. Langbein, P. Borri, U. Woggon, V. Stavarache, D. Reuter, and A. D. Wieck, Phys. Rev. B **70**, 033301 (2004).

[80] W. Demtröder, *Laser Spectroscopy, Experimental Techniques* (Springer, 2008).

[81] J. Mark and J. Mørk, Applied Physics Letters **61**, 2281 (1992).

[82] J. Mørk, M. Willatzen, J. Mark, M. Preisel, and C. P. Seltzer, in *SPIE, Physics and Simulation of Optoelectronic Devices II*, edited by W. W. Chow and M. Osinski (SPIE, 1994), vol. 2146, pp. 52–67.

[83] K. L. Hall, A. M. Darwish, E. P. Ippen, U. Koren, and G. Raybon, Applied Physics Letters **62**, 1320 (1993).

[84] K. L. Hall, G. Lenz, A. M. Darwish, and E. P. Ippen, Optics Communications **111**, 589 (1994), ISSN 0030-4018.

[85] K. L. Hall, G. Lenz, E. P. Ippen, and G. Raybon, Opt. Lett. **17**, 874 (1992).

[86] J. Mørk, J. Mark, and C. P. Seltzer, Applied Physics Letters **64**, 2206 (1994).

[87] E. Yablonovitch, Phys. Rev. Lett. **58**, 2059 (1987).

[88] P. Lodahl, A. Floris van Driel, I. S. Nikolaev, A. Irman, K. Overgaag, D. Vanmaekelbergh, and W. L. Vos, Nature **430**, 654 (2004), ISSN 0028-0836.

[89] D. Englund, D. Fattal, E. Waks, G. Solomon, B. Zhang, T. Nakaoka, Y. Arakawa, Y. Yamamoto, and J. Vučković, Phys. Rev. Lett. **95**, 013904 (2005).

[90] M. Fujita, S. Takahashi, Y. Tanaka, T. Asano, and S. Noda, Science **308**, 1296 (2005).

[91] H. Altug, D. Englund, and J. Vuckovic, Nat Phys **2**, 484 (2006), ISSN 1745-2473.

[92] D.-S. Kim, J. Shah, J. E. Cunningham, T. C. Damen, W. Schäfer, M. Hartmann, and S. Schmitt-Rink, Phys. Rev. Lett. **68**, 1006 (1992).

[93] A. J. Zilkie, J. Meier, P. W. E. Smith, M. Mojahedi, J. S. Aitchison, P. J. Poole, C. N. Allen, P. Barrios, and D. Poitras, Opt. Express **14**, 11453 (2006).

[94] A. J. Zilkie, J. Meier, M. Mojahedi, P. J. Poole, P. Barrios, D. Poitras, T. J. Rotter, C. Yang, A. Stintz, K. J. Malloy, et al., IEEE Journal of Quantum Electronics **43**, 982 (2007).

[95] R. Heitz, H. Born, F. Guffarth, O. Stier, A. Schliwa, A. Hoffmann, and D. Bimberg, Phys. Rev. B **64**, 241305 (2001).

[96] S. Sauvage, P. Boucaud, T. Brunhes, M. Broquier, C. Crépin, J.-M. Ortega, and J.-M. Gérard, Phys. Rev. B **66**, 153312 (2002).

[97] T. S. Sosnowski, T. B. Norris, H. Jiang, J. Singh, K. Kamath, and P. Bhattacharya, Phys. Rev. B **57**, R9423 (1998).

[98] D. Birkedal, J. Bloch, J. Shah, L. N. Pfeiffer, and K. West, Applied Physics Letters **77**, 2201 (2000).

[99] K. L. Silverman, R. P. Mirin, S. T. Cundiff, and A. G. Norman, Applied Physics Letters **82**, 4552 (2003).

[100] R. J. Warburton, C. S. Dürr, K. Karrai, J. P. Kotthaus, G. Medeiros-Ribeiro, and P. M. Petroff, Phys. Rev. Lett. **79**, 5282 (1997).

[101] O. Stier, M. Grundmann, and D. Bimberg, Phys. Rev. B **59**, 5688 (1999).

[102] R. Nötzel, S. Anantathanasarn, R. van Veldhoven, F. van Otten, T. Eijkemans, A. Trampert, B. Satpati, Y. Barbarin, E. Bente, Y. Oei, et al., Jpn. J. Appl. Phys **45**, 6544 (2006).

[103] F. Lelarge, B. Dagens, J. Renaudier, R. Brenot, A. Accard, F. van Dijk, F. van Dijk, D. Make, O. Le Gouezigou, J. G. Provost, et al., IEEE Journal of Selected Topics in Quantum Electronics **13**, 111 (2007).

[104] T. W. Berg, Ph.D. thesis, Technical University of Denmark (2004).

[105] S. Schneider, P. Borri, W. Langbein, U. Woggon, R. L. Sellin, D. Ouyang, and D. Bimberg, Photonics Technology Letters, IEEE **17**, 2014 (2005).

[106] E. Kreyszig, *Advanced Engineering Mathematics* (John Wiley & Sons, Hoboken, NewJersey, USA, 2006), 9th ed.

[107] L. M. Frantz and J. S. Nodvik, Journal of Applied Physics **34**, 2346 (1963).

[108] G. Agrawal and N. Olsson, Quantum Electronics, IEEE Journal of **25**, 2297 (1989), ISSN 0018-9197.

[109] U. Keller, *Progress in Optics* (Elsevier, 2004), vol. 46, chap. Ultrafast Solid State Lasers, pp. 1–115.

[110] J. T. Verdeyen, *Laser Electronics*, Prentice Hall series in solid state physical electronics (Prentice Hall, Englewood Cliffs, New Jersey 07632 , USA, 1995), 3rd ed.

[111] F. Träger, ed., *Handbook of Lasers and Optics* (Springer, New York, USA, 2007).

[112] D. J. Kane and R. Trebino, IEEE Journal of Quantum Electronics **29**, 571 (1993).

[113] R. Trebino, K. W. DeLong, D. N. Fittinghoff, J. N. Sweetser, M. A. Krumbugel, B. A. Richman, and D. J. Kane, Review of Scientific Instruments **68**, 3277 (1997).

[114] P. Borri, W. Langbein, J. Mørk, and J. M. Hvam, Optics Communications **169**, 317 (1999), ISSN 0030-4018.

[115] P. Borri, W. Langbein, J. M. Hvam, F. Heinrichsdorff, M.-H. Mao, and D. Bimberg, IEEE Journal of Selected Topics in Quantum Electronics **6**, 544 (2000).

[116] P. Borri, W. Langbein, J. M. Hvam, F. Heinrichsdorff, M.-H. Mao, and D. Bimberg, IEEE Photonics Technology Letters **12**, 594 (2000).

[117] A. Mecozzi and J. Mørk, J. Opt. Soc. Am. B **13**, 2437 (1996).

[118] A. Weiner, Review of Scientific Instruments **71**, 1929 (2000).

[119] A. Weiner and A. Kan'an, IEEE Journal of Selected Topics in Quantum Electronics **4**, 317 (1998).

[120] K. Yvind, Ph.D. thesis, Technical University of Denmark, Research Center COM, Optoelectronics (2003).

[121] R. J. Manning, A. Antonopoulos, R. Le Roux, and A. E. Kelly, Electronics Letters **37**, 229 (2001).

[122] J. Mørk and A. Mecozzi, J. Opt. Soc. Am. B **13**, 1803 (1996).

[123] C. Henry, IEEE Journal of Quantum Electronics **18**, 259 (1982).

[124] C. Pethick and H. Smith, *Bose-Einstein condensation in dilute gases* (Camebridge University Press, 2001), 1st ed.

[125] M. Fleischhauer, A. Imamoglu, and J. P. Marangos, Review of Moderne physics **77**, 633 (2005).

[126] J. Kim, S. L. Chuang, P. C. Ku, and C. J. Chang-Hasnain, Journal of Physics: Condensed Matter **16**, S3727 (2004).

[127] M. Bayer and A. Forchel, Phys. Rev. B **65**, 041308 (2002).

[128] Y. Nakata, Y. Sugiyama, and M. Sugawara, *Self-assembled InGaAs/GaAs Quantum dots* (Academic Press, 1999), chap. 2, pp. 117–154.

[129] R. Heitz, I. Mukhametzanov, H. Born, M. Grundmann, A. Hoffmann, A. Madhukar, and D. Bimberg, Physica B: Condensed Matter **272**, 8 (1999), ISSN 0921-4526.

[130] J. Houmark, T. R. Nielsen, J. M. rk, and A.-P. Jauho, Physical Review B (Condensed Matter and Materials Physics) **79**, 115420 (pages 6) (2009).

[131] J. Houmark, A. Jauho, T. Nielsen, and J. Mørk, in *Journal of Physics: Conference Series* (Institute of Physics Publishing, 2008), vol. 107, p. 012005.

[132] T. R. Nielsen, A. Lavrinenko, and J. Mørk, Applied Physics Letters **94**, 113111 (pages 3) (2009).

[133] W. W. Chow, H. C. Schneider, and M. C. Phillips, Phys. Rev. A **68**, 053802 (2003).

[134] S. Marcinkevičius, A. Gushterov, and J. P. Reithmaier, Applied Physics Letters **92**, 041113 (2008).

[135] M. Bayer, G. Ortner, O. Stern, A. Kuther, A. A. Gorbunov, A. Forchel, P. Hawrylak, S. Fafard, K. Hinzer, T. L. Reinecke, et al., Phys. Rev. B **65**, 195315 (2002).

[136] D. Gammon, E. S. Snow, B. V. Shanabrook, D. S. Katzer, and D. Park, Phys. Rev. Lett. **76**, 3005 (1996).

[137] R. Seguin, S. Rodt, A. Schliwa, K. Pötschke, U. W. Pohl, and D. Bimberg, physica status solidi (b) **243**, 3937 (2006).

[138] M. Bayer, A. Kuther, A. Forchel, A. Gorbunov, V. B. Timofeev, F. Schäfer, J. P. Reithmaier, T. L. Reinecke, and S. N. Walck, Phys. Rev. Lett. **82**, 1748 (1999).

[139] A. Rastelli, S. Stufler, A. Schliwa, R. Songmuang, C. Manzano, G. Costantini, K. Kern, A. Zrenner, D. Bimberg, and O. G. Schmidt, Phys. Rev. Lett. **92**, 166104 (2004).

[140] Q. Xie, J. L. Brown, R. L. Jones, J. E. V. Nostrand, and K. D. Leedy, Applied Physics Letters **76**, 3082 (2000).

[141] R. Heitz, I. Mukhametzhanov, O. Stier, A. Madhukar, and D. Bimberg, Phys. Rev. Lett. **83**, 4654 (1999).

[142] T. F. Boggess, L. Zhang, D. G. Deppe, D. L. Huffaker, and C. Cao, Applied Physics Letters **78**, 276 (2001).

[143] J. Siegert, S. Marcinkevičius, and Q. X. Zhao, Phys. Rev. B **72**, 085316 (2005).

[144] J.-C. Diels and W. Ruldolph, *Ultrashort Laser Phenomena* (Elsevier, London, UK, 2006).

[145] R. Brenot, M. Manzanedo, J. Provost, O. Legouezigou, F. Pommereau, F. Poingt, L. Legouezigou, E. Derouin, O. Drisse, B. Rousseau, et al., in *Conference and Exhibition on Optical Communication - ECOC* (IEE, 2007).

[146] P. Michler, *Single Quantum Dots, Fundamentals, Applications, and New Concepts* (Springer, 2003).

[147] P. Borri, S. Schneider, W. Langbein, U. Woggon, A. E. Zhukov, V. M. Ustinov, N. N. Ledentsov, Z. I. Alferov, D. Ouyang, and D. Bimberg, Applied Physics Letters **79**, 2633 (2001).

[148] H. Dery, E. Benisty, A. Epstein, R. Alizon, V. Mikhelashvili, G. Eisenstein, R. Schwertberger, D. Gold, J. P. Reithmaier, and A. Forchel, Journal of Applied Physics **95**, 6103 (2004).

[149] M. van der Poel, E. Gehrig, O. Hess, D. Birkedal, and J. M. Hvam, IEEE Journal of Quantum Electronics **41**, 1115 (2005).

[150] M. Van der Poel, J. Mørk, A. Somers, A. Forchel, J. Reithmaier, and G. Eisenstein, Applied Physics Letters **89**, 081102 (2006).

[151] N. J. Kim, J. M. Oh, M. D. Kim, D. Lee, S. H. Pyun, W. G. Jeong, and J. W. Jang, Applied Physics Letters **90**, 241108 (pages 3) (2007).

[152] M. Grundmann and D. Bimberg, Phys. Rev. B **55**, 9740 (1997).

[153] K. L. Hall, J. Mark, E. P. Ippen, and G. Eisenstein, Applied Physics Letters **56**, 1740 (1990).

[154] A. Zilkie, J. Meier, M. Mojahedi, A. S. Helmy, P. J. Poole, P. Barrios, D. Poitras, T. J. Rotter, C. Yang, A. Stintz, et al., J. Lightwave Technol. **26**, 1498 (2008).

[155] C.-K. Sun, H. K. Choi, C. A. Wang, and J. G. Fujimoto, Applied Physics Letters **62**, 747 (1993).

[156] E. A. Zibik, T. Grange, B. A. Carpenter, N. E. Porter, R. Ferreira2, G. Bastard, D. Stehr, S. Winner, M. Helm, H. Y. Liu, et al., Nature Materials **8**, 803 (2009).

# Acronyms

**ASE** amplified spontaneous emission

**AOM** acousto optical modulator

**BBO** $\beta-\mathrm{BaB_2O_4}$

**CH** carrier heating

**CPO** coherent population oscillations

**EA** electro absorber

**EIT** electromagnetically induced transparency

**FROG** frequency resolved optical gating

**FWHM** full width at half maximum

**GVD** group velocity dispersion

**IHB** inhomogeneous broadening

**ND** neutral density

**PCW** photonic crystal waveguide

**PC** photonic crystal

**RegA** regenerative amplifier

**OPA** optical parametric amplifier

**QD** quantum dot

**QW** quantum well

**SHB** spectral hole burning

**SLM** spatial light modulator

**SOA** semiconductor optical amplifier

**TPA** two photon loss

**WGL** waveguide loss